UC Berkeley
UC Berkeley Electronic Theses and Dissertations

Title
Simulation of the Atmospheric Boundary Layer for Wind Energy Applications

Permalink
https://escholarship.org/uc/item/8xg692q7

Author
Marjanovic, Nikola

Publication Date
2015

Peer reviewed|Thesis/dissertation

Simulation of the Atmospheric Boundary Layer for Wind Energy Applications

by

Nikola Marjanovic

A dissertation submitted in partial satisfaction of the

requirements for the degree of

Doctor of Philosophy

in

Engineering - Civil and Environmental Engineering

in the

Graduate Division

of the

University of California, Berkeley

Committee in charge:

Professor Fotini K. Chow, Chair
Professor Robert A. Harley
Professor John Chiang
Dr. Jeffrey D. Mirocha

Fall 2015

Simulation of the Atmospheric Boundary Layer for Wind Energy Applications

Abstract

Simulation of the Atmospheric Boundary Layer for Wind Energy Applications

by

Nikola Marjanovic

Doctor of Philosophy in Engineering - Civil and Environmental Engineering

University of California, Berkeley

Professor Fotini K. Chow, Chair

Energy production from wind is an increasingly important component of overall global power generation, and will likely continue to gain an even greater share of electricity production as world governments attempt to mitigate climate change and wind energy production costs decrease. Wind energy generation depends on wind speed, which is greatly influenced by local and synoptic environmental forcings. Synoptic forcing, such as a cold frontal passage, exists on a large spatial scale while local forcing manifests itself on a much smaller scale and could result from topographic effects or land-surface heat fluxes. Synoptic forcing, if strong enough, may suppress the effects of generally weaker local forcing. At the even smaller scale of a wind farm, upstream turbines generate wakes that decrease the wind speed and increase the atmospheric turbulence at the downwind turbines, thereby reducing power production and increasing fatigue loading that may damage turbine components, respectively. Simulation of atmospheric processes that span a considerable range of spatial and temporal scales is essential to improve wind energy forecasting, wind turbine siting, turbine maintenance scheduling, and wind turbine design.

Mesoscale atmospheric models predict atmospheric conditions using observed data, for a wide range of meteorological applications across scales from thousands of kilometers to hundreds of meters. Mesoscale models include parameterizations for the major atmospheric physical processes that modulate wind speed and turbulence dynamics, such as cloud evolution and surface-atmosphere interactions. The Weather Research and Forecasting (WRF) model is used in this dissertation to investigate the effects of model parameters on wind energy forecasting. WRF is used for case study simulations at two West Coast North American wind farms, one with simple and one with complex terrain, during both synoptically and locally-driven weather events. The model's performance with different grid nesting configurations, turbulence closures, and grid resolutions is evaluated by comparison to observation data. Improvement to simulation results from the use of more computationally expensive high resolution simulations is only found for the complex terrain simulation during the locally-driven event. Physical parameters, such as soil moisture, have a large effect

on locally-forced events, and prognostic turbulence kinetic energy (TKE) schemes are found to perform better than non-local eddy viscosity turbulence closure schemes.

Mesoscale models, however, do not resolve turbulence directly, which is important at finer grid resolutions capable of resolving wind turbine components and their interactions with atmospheric turbulence. Large-eddy simulation (LES) is a numerical approach that resolves the largest scales of turbulence directly by separating large-scale, energetically important eddies from smaller scales with the application of a spatial filter. LES allows higher fidelity representation of the wind speed and turbulence intensity at the scale of a wind turbine which parameterizations have difficulty representing. Use of high-resolution LES enables the implementation of more sophisticated wind turbine parameterizations to create a robust model for wind energy applications using grid spacing small enough to resolve individual elements of a turbine such as its rotor blades or rotation area.

Generalized actuator disk (GAD) and line (GAL) parameterizations are integrated into WRF to complement its real-world weather modeling capabilities and better represent wind turbine airflow interactions, including wake effects. The GAD parameterization represents the wind turbine as a two-dimensional disk resulting from the rotation of the turbine blades. Forces on the atmosphere are computed along each blade and distributed over rotating, annular rings intersecting the disk. While typical LES resolution (10-20 m) is normally sufficient to resolve the GAD, the GAL parameterization requires significantly higher resolution (1-3 m) as it does not distribute the forces from the blades over annular elements, but applies them along lines representing individual blades.

In this dissertation, the GAL is implemented into WRF and evaluated against the GAD parameterization from two field campaigns that measured the inflow and near-wake regions of a single turbine. The data-sets are chosen to allow validation under the weakly convective and weakly stable conditions characterizing most turbine operations. The parameterizations are evaluated with respect to their ability to represent wake wind speed, variance, and vorticity by comparing fine-resolution GAD and GAL simulations along with coarse-resolution GAD simulations. Coarse-resolution GAD simulations produce aggregated wake characteristics similar to both GAD and GAL simulations (saving on computational cost), while the GAL parameterization enables resolution of near wake physics (such as vorticity shedding and wake expansion) for high fidelity applications.

For the first time, to our knowledge, this dissertation combines the capabilities of a mesoscale weather prediction model, LES, and high-resolution wind turbine parameterizations into one model capable of simulating a real array of wind turbines at a wind farm. WRF is used due to its sophisticated environmental physics models, frequent use in the atmospheric modeling community, and grid nesting with LES capabilities. Grid nesting is feeding lateral boundary condition data from a coarse resolution simulation to a finer resolution simulation contained within the coarse resolution simulation's domain. WRF allows the development of a grid nesting strategy from synoptic-scale to microscale LES relevant for wind farm simulations; this is done by building on the results from the investigation of model parameters for wind energy forecasting and the implementation of the GAD and GAL wind turbine parameterizations. The nesting strategy is coupled with a GAD parameterization to

model the effects of wind turbine wakes on downstream turbines at a utility-scale Oklahoma wind farm. Simulation results are compared to dual-Doppler measurements that provide three-dimensional fields of horizontal wind speed and direction. The nesting strategy is able to produce realistic turbine wake effects, while differences with the measurements can mostly be attributed to the quality of the available weather input data.

To Katie

Contents

List of Figures

List of Tables

Acknowledgments

This dissertation has been made possible thanks to the support of many individuals and organizations to whom I am grateful. They have all contributed to experiences that have made my time in Berkeley and Livermore both memorable and enriching.

I thank my advisor, Professor Tina K. Chow, for her patience, guidance, and mentorship during my Ph.D. Her dedication and positive attitude are an inspiration to me and all her students. I was impressed by the first fluid mechanics course I took with Tina; she is the best college instructor I have had. This lead to an undergraduate research project with her and the rest is history. I appreciate how she always makes sure I understand the big picture and the theory behind what it is I am doing. Her encouragement when things did not go according to plan and excitement when an interesting result was uncovered will never be forgotten.

I am grateful to Dr. Jeffrey Mirocha, my mentor at Lawrence Livermore National Laboratory (LLNL), for serving as a second advisor to me. His generous investment of time and effort into teaching me about WRF and how to be a stronger writer are greatly appreciated. He was always available to talk and possessed tremendous patience when explaining anything to me. I cannot thank him enough for all his encouragement and friendship throughout my time in Livermore.

I also thank the rest of my committee members for all their help and support. I am grateful to Professor John Chiang for introducing me to atmospheric dynamics through his great class, on which I have relied on throughout my Ph.D. Professor Robert Harley taught me about air quality and provided the missing link between atmospheric science and environmental engineering. I also appreciate Professor Mark Stacey and his service on my qualifying and preliminary exam committees. Professor Evan Variano served on my preliminary exam committee and was always a welcome presence at group meetings.

Unlike most graduate students, I have had the honor to complete most of my research at LLNL thanks to the generous funding and support of the Lawrence Livermore Graduate Scholar Program and the Atmospheric, Earth, and Energy Division. This would not have been possible without the collaboration and help of Sonia Wharton. I am grateful for the data sets she provided to validate my simulations and for all her early encouragement and friendship. Katie Lundquist is another colleague at LLNL to whom I am indebted to for all the help with WRF she has given me over the years and for generously providing funding for my last few months at the lab. Many thanks to Julie Lundquist for her role in getting me started in wind energy for my first Ph.D. project, and to Branko Kosovic for sharing his actuator disk parameterization with me. I am also thankful to Gokhan Kirkil, Jessica Osuna, and Matthew Simpson for all their help along the way.

It was a great honor to be a part of the Environmental Fluid Mechanics group at Berkeley. They are some of the friendliest and most intelligent people I know. I will miss the beer hours, coffee breaks, lunches, and random conversations we have shared together. I am grateful to Bowen Zhou, who was with me from the beginning and taught me a great deal about Unix, computational modeling, and atmospheric fluid dynamics. He always made time to help

anyone in need and exuded great patience and knowledge in the process. I am thankful to Megan Daniels for taking me as her summer undergraduate research assistant and for making me feel welcome and teaching me about the atmospheric boundary layer. Andreas Brand deserves more appreciation than I can convey for his friendship during the work week and all the fun outdoor weekend activities he planned when I first started my Ph.D. Thanks to David Wiersema, Jason Simon, Lauren Goodfriend, Diane Taylor, Alex Connolly, Ian Tse, Audric Collignon, Wayne Wagner, Megan Williams, Rusty Holleman, Kevin Hsu, Cristina Poindexter, Mike Dvorak, and many more for all your help and companionship along this journey. Thanks to my roommate and best man, Kenny Lee, for going through the graduate experience with me and helping me get through the computational mathematics and fluid dynamics courses we took together.

My family deserves praise nearly impossible to express. I am grateful to my mother and father for all of their unconditional love and support. They have played a significant role as inspirations for my decision to pursue a degree in Civil and Environmental Engineering. Their selflessness and sacrifice for my sister and me will never be forgotten. I am also thankful to my sister, Jana, and the inspiration she has been to me.

Last, but not least, I thank my wife, Katie, for all her love and encouragement. I would not have met her if I did not come to Berkeley for my Ph.D. and notice this beautiful woman my first day in O'Brien Hall. Her intelligence, humor, and companionship have made my graduate experience all the more worthwhile.

Chapter 1

Introduction

1.1 General Description and Motivation

Wind turbines produce power by extracting kinetic energy from the wind. Most turbines are sited on land and operate in the atmospheric boundary layer (ABL), the region of the atmosphere adjacent to the earth's surface. Atmospheric conditions in the ABL can vary due to changes imparted by a diurnal cycle, weather events, mesoscale processes, terrain channeling, and changes in surface cover among other factors. These variations make wind speed, direction, and turbulence difficult to predict (Mahoney et al., 2012). Large scale, synoptic forcing events such as frontal passages and smaller scale, local forcing events such as land-surface heat fluxes can both contribute to wind dynamics. The strength of these events (even in proportion to one another) varies for different locales and time periods. Most locales encounter specific flow conditions due to unique facets such as topography, weather, and soil type. Therefore general heuristic/simple atmospheric models do not perform well.

Wind turbine spacing is a compromise between plant costs and the minimization of turbine wake interactions. The typical spacings (6-10D), however, are still insufficient to avoid significant wake effects that at times can influence performance and reliability. Wakes are produced at upwind turbines and impact any downstream turbines in their vicinity. These wakes are characterized by reduced wind speeds and increased turbulence which decrease power production and increase fatigue loading on downwind turbines, respectively (Högström et al., 1988; Magnusson and Smedman, 1999). The variability of atmospheric conditions over a large range of physical and temporal scales determines wind turbine wake interactions.

Renewable energy resources are gaining an increasingly larger share of the energy sector, which consequentially has placed even greater importance on securing and predicting wind energy sources. Improved weather prediction capabilities are vital to both short and long term energy management. Precise short term forecasting (minutes to days) allows for more wind power to be integrated into the energy grid at a lower cost and leads to reduced fossil fuel power generation (e.g., coal) required to maintain system security (Marquis et al., 2011). Improved long term forecasting (months to years) enables more efficient wind turbine

siting and design appropriate for a specific site's topography and weather patterns. Turbine siting and design also greatly benefit from improved simulation and understanding of turbine wake interactions. Enhanced weather forecasting and turbine wake modeling capabilities, together, present a powerful tool to better integrate power production into the grid. They also help determine if a site (and turbine placement strategy) is appropriate to generate the wind speeds necessary for wind power production, while maintaining turbulence intensity and wind shear below levels that would lead to periods of extended in-operation and turbine damage.

The work described in this dissertation aims to better understand and improve weather modeling methodologies for wind energy forecasting and wind turbine wake interactions. In addition, the goal is to develop a numerical model capable of internally coupling mesoscale with microscale wind farm simulations. Traditionally, engineering wake models are not able to represent atmospheric drivers of wind turbine wake variability over a large range of atmospheric scales. Mesoscale weather models are used for wind energy applications, but they represent turbulence using the Reynolds-Averaged Navier-Stokes (RANS) equations, which may not adequately capture transients in turbulence dynamics. Microscale computational fluid dynamics models (CFD) can better resolve turbulence by using large-eddy simulation (LES), but rely on idealized initial and boundary conditions while also lacking the capability to represent variations in synoptic weather events. Some numerical weather models, such as the Weather Research and Forecasting (WRF) model, possess the capability to nest from mesoscale domains that utilize RANS to microscale domains that use LES, however, these models lack turbine parameterizations that are compatible with LES or able to represent turbine wakes in detail.

1.2 Background

Prior studies have focused on both atmospheric modeling for wind energy applications and development/testing of different wind turbine parameterizations. Weather forecast models provide representation of physical processes driving wind flow which include radiation, clouds, planetary rotation, and surface exchange parameterizations needed for realistic representation of atmospheric flow. Many studies over the past few decades have been performed to assess the importance of different model parameters (e.g. grid spacing, turbulence parameterization etc.) on the accuracy of simulation results. In the past few years, however, some of these studies have focused on the significance of these parameters in accurately predicting atmospheric features important to wind turbine operations (e.g. turbine hub height wind speed and turbulence intensity). A few of those studies include a wind power forecasting system to optimize grid integration (Mahoney et al., 2012), a sensitivity study of model wind simulation for an area of high wind energy (Carvalho et al., 2012), a model ensemble for improved wind speed forecasts at turbine height (Deppe et al., 2012), and simulations nested from synoptic to LES scale for wind energy applications (Liu et al., 2011). Various wind turbine parameterizations have been developed to accurately represent the effects of turbine

generated wakes. These parameterizations can be categorized into the generalized actuator disk approach (Ammara et al., 2002; Madsen, 1996; Mikkelsen, 2003; Sørensen et al., 1998), the generalized actuator line approach (Mikkelsen et al., 2007; Sorensen and Shen, 2002; Troldborg et al., 2007), and the direct approach (Duque et al., 2003; Sørensen and Hansen, 1998; Zahle et al., 2009). Although direct modeling of the turbine rotor by constructing a body-fitted grid would yield the highest fidelity solution in computing flow around a turbine, it is computationally prohibitively expensive for long timescales and arrays of turbines. Instead of representing a turbine blade exactly, a disk or a line approximation, characteristic of the generalized actuator approach, is advantageous for accurate parameterizations that make use of more limited computational resources.

This dissertation investigates the importance of different simulation approaches for a mesoscale weather model and contributes to the testing and implementation of actuator disk parameterizations into an atmospheric simulation tool. The ultimate goal is to develop a unified model capable of nesting microscale LES wind turbine parameterizations within mesoscale weather simulations. The high fidelity microscale simulations would benefit from the realistic boundary conditions and atmospheric physical process parameterizations brought in by the mesoscale domains that are necessary to simulate complex atmospheric flows. Benefits from the development of such a multiscale atmospheric simulation framework would reach beyond wind energy applications, as the framework could be used for air quality or general numerical weather forecasting as well.

The Weather Research and Forecasting (WRF) (Skamarock et al., 2008) model is chosen to develop the mesoscale-microscale coupled wind farm simulation capabilities. Its support of both mesoscale and microscale simulation, wide user base, and an active development community make WRF a compelling modeling option.

Mesoscale Simulation for Wind Energy Applications

Effective atmospheric simulation requires an understanding of the relevant scales of motion that are important to capture and numerical considerations such as the appropriate domain size, mesh spacing, and time step. This understanding is also important for the selection of appropriate atmospheric process parameterizations to capture the relevant physics at the proper scales. Essentially, a numerical weather prediction model uses sufficiently high horizontal and vertical grid resolution to forecast mesoscale weather phenomena such as large convective systems or frontal passages over a three-dimensional area (domain). Features related to convection, topography, or coastlines generally force these weather phenomena. The core of numerical weather prediction is a set of mathematical equations that represent the physical laws of motion and conservation laws. These equations govern the evolution of the atmosphere and can predict how their variables (wind, pressure, etc.) change in time, and thus what the weather will be in the future. In this work, WRF uses a fully compressible, Eulerian and non-hydrostatic equation set (based on the Navier Stokes equations). The numerical weather simulation is initialized with available observation or simulation data and is usually updated with lateral boundary condition data as the prognostic equations are inte-

grated in time (third order Runge-Kutta scheme in WRF). The fidelity of simulation results is dependent on controllable simulation parameters such as grid resolution, turbulence parameterizations, and land-surface representations that may influence atmospheric dynamics relevant to wind energy applications.

Model Grid Resolution

Grid resolution is a basic modeling parameter that can impact simulation results significantly. The horizontal resolution is directly related to the scale of a feature that can be simulated. The higher (finer) the resolution, the smaller the feature the model can successfully represent. WRF, like most operation numerical weather models, uses equally spaced horizontal grid points at which the forecast equations are solved. Weather models typically require at least five to seven grid points to define a weather feature based on their numerics (Skamarock et al., 2008). An increase in resolution, however, requires increased computational resources due to an increase of the number of grid points over the same area and the necessity to decrease the time-step for numerical stability. Weather models, such as WRF, employ grid nesting to help reduce computational expense when higher resolution is required. Grid nesting consists of a finer resolution domain "nested" within a coarser resolution parent domain, where the finer resolution domain utilizes lateral boundary conditions from the coarser parent domain. While the fine resolution domain is more computationally expensive, it is only used over a small area, which is cheaper than resolving the whole domain at that higher resolution. Such a set-up still enables the resolution of large-scale synoptic weather phenomena that span larger physical distances with the coarse resolution parent domain.

The horizontal grid resolution necessary for wind energy applications is dependent on weather and site conditions as well as the intended application. Expected weather conditions can influence the choice of horizontal grid resolution. These conditions can occur at several scales. Certain conditions such as sea breezes or thermally-driven winds occur at local scales, whereas frontal passages are generally synoptically-driven phenomena. Low-level jets are an important wind energy resource that can occur over vastly different scales due to different physics. Simulations during periods dominated by strong synoptically-driven events may not require fine grid resolution due to the longer time scales that are characteristic of these weather phenomena. Topography can significantly affect a model's prediction abilities, as wind farms located in an area with particularly complex terrain may require finer resolution grid spacing to achieve accurate results. Many studies have demonstrated improvements in simulation results with higher grid resolution for locations with some terrain complexity (Carvalho et al., 2012; Chen et al., 2004; Grell et al., 2000; Gronas and Sandvik, 1999; Mass et al., 2003). Conversely, significant computational resources could be saved by using coarser resolution for cases in which terrain and meteorology are simple (Marjanovic et al., 2014).

Vertical grid resolution is usually specified independently from the horizontal grid resolution. Unlike horizontal grid spacing, vertical grid spacing is not constant, but is commonly stretched in height depending on the application to save computational resources. Higher vertical resolution is also needed to resolve turbulent eddies in LES. WRF, like most mesoscale

models, uses terrain following vertical coordinates to avoid problems constant pressure or height coordinates have when intersecting the ground. Past studies have considered the effects of vertical resolution on simulation results, but have found that while there is improvement with higher resolution near the surface in complex terrain, it is not as significant as improvement due to increased horizontal resolution (Talbot et al., 2012; Zhang et al., 2013a).

Turbulence Parameterizations

Strong turbulent eddies can manifest at scales relevant to the wind farm, but too small for a mesoscale model to resolve. Atmospheric flows contain motions over a broad spectrum of scales, with small-scale turbulent motions near the surface responsible for surface drag and vertical exchanges of heat, moisture, and momentum. For mesoscale simulations, the model resolution is too coarse to resolve turbulence motions. Therefore, those small scale motions must be parameterized to obtain the proper surface drag and other global characteristics such as storm spinup and spindown. Mesoscale models, such as WRF, commonly use turbulence closure (parameterization) options based on the Reynolds-Averaged Navier Stokes (RANS) equations of motion, as they are generally used at grid spacings unable to resolve the most energetic turbulent scales. These closures are referred to as Planetary Boundary Layer (PBL) schemes. They tend to differ in how vertical turbulence diffusion (mixing) is parameterized. Many PBL schemes predict the subgrid turbulent kinetic energy (TKE) using a prognostic TKE equation to obtain the vertical eddy viscosity, which characterizes the transport and dissipation of energy in the smaller-scale unresolved flow. These schemes differ from less computationally expensive lower order parameterizations that do not solve a prognostic TKE equation, but instead use more general empirical methods to obtain an eddy viscosity. Past studies have not found a single PBL scheme to recommend for all situations, instead, each scheme has certain strengths and weaknesses (Yver et al., 2013; Zhang et al., 2013a).

Progressing to finer resolution simulations at the scale of wind turbines allows for the resolution of some turbulence scales and the use of LES. Figure 1.1 shows the turbulent energy cascade. LES is used when the largest energy-containing eddies can be resolved. While the largest eddies are resolved, the smaller eddies that cannot be resolved must be parameterized to maintain the correct energetics of the resolved scales. These are parameterized in a subgrid-scale (SGS) stress model. RANS can be used at LES scales, however only LES resolves the transients, which are important for wake formation and evolution, instantaneous power production and fatigue loading. The RANS parameterizations are utilized with coarse resolution grids that cannot usually resolve even the largest energy-containing eddies and instead parameterize them. WRF supports LES via several LES turbulence SGS models and idealized simulation setups. This dissertation expands beyond idealized setups by linking LES with mesoscale input through the built-in WRF nesting procedures. LES provides higher fidelity results on nested fine resolution domains that may contain wind turbine parameterizations, however, the transition from RANS to LES simulations can be challenging when nesting with WRF (Wyngaard, 2004) and has not been extensively tested (Liu et al.,

2011).
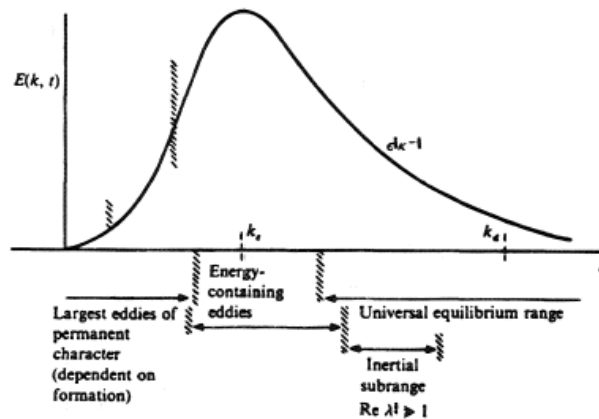
Figure 1.1: Turbulent energy (E) distribution in wave number (k) space (largest eddies have a smaller wave number). (Landahl and Mollo-Christensen, 1986)

Surface Exchange Representations

Along with turbulence, several other surface exchange processes are typically parameterized in a mesoscale numerical model. These include longwave radiation, solar insolation and reflection, evapotranspiration, convection, vegetation and land-use effects, and soil moisture/temperature. Near-surface physics, along with cloud/moisture processes and atmospheric radiation physics, need to be parameterized because they are important to realistic forecasting and they are either not capable of being numerically resolved and/or the processes are not well understood enough to be represented precisely. Accurate parameterization of surface conditions is more important when local-scale forcing phenomena with short time scales dominate (Chow et al., 2006). Most mesoscale numerical models, WRF included, parameterize certain surface effects based on values for a select number of land-use and soil categories (including sea surface temperature and wave state over oceans). An accurate overlay of these categories over a domain's surface along with accurate initialization data and surface schemes can profoundly influence the atmospheric physics wind energy forecasts rely on.

Wind Turbine Parameterization

Operating turbines can be represented in CFD in several ways. The most accurate is to explicitly resolve the turbine tower and blades and apply no slip boundary conditions on the surfaces, but this is too computationally expensive to permit simultaneous representation of both turbine dynamics and weather events. For mesoscale applications, for which grid spacing is too coarse to resolve turbine components, WRF currently contains

a publicly available wind farm/turbine parameterization, however this approach does not capture turbine-turbulence interactions. An approach that still captures turbine-turbulence interactions at intermediate resolution and computational expense is to use actuator models. These models parameterize aerodynamic interactions of turbulent flow with a wind turbine's blades, and provide forcing of the flow via the prognostic flow equations in the vicinity of a turbine.

WRF Mesoscale Parameterization

The WRF built-in wind farm/turbine parameterization was developed by Fitch et al. (2012) and based on a wind farm parameterization proposed by Adams and Keith (2007). The wind turbines are modeled as a momentum sink and TKE source in grid cells containing the turbine blades. The drag force over the actuator disk, formed by the rotation of the blades, is calculated using the thrust coefficient (drag coefficient) specific to the blade. It is then possible to calculate a momentum tendency term with which to modify the prognostic equations in WRF. The parameterization assumes the portion of total kinetic energy (obtained from the drag force on the disk) extracted from the atmosphere by the turbine, and not converted into power, contributes to an increase in TKE. The fraction of total kinetic energy converted into TKE can be found by subtracting the turbine's power coefficient from its thrust coefficient, where the power coefficient is the fraction of kinetic energy extracted from the wind that is converted to power. This allows for the TKE tendency equation to be modified to account for the increase of TKE, which means that the PBL schemes that use a prognostic TKE equation are the only ones able to use this parameterization. In summary, the momentum sink and TKE source produced are averaged over the model levels within the grid cells containing the turbine blades. The parameterization was tested by Fitch et al. (2012) in an idealized setting that gave good results. The test was for a wind farm with a turbine density specified for each grid cell within the wind farm's bounds.

Generalized Actuator Disk Model

High resolution LES capable of resolving the actuator disk produced by the rotation of a wind turbine's blades is required to accurately represent the resolved momentum and turbulent structures in its wake. The generalized actuator disk (GAD) model parameterizes the effects of wind turbine thrust and torque (rotation) by computing lift and drag forces on the turbine blades by using their known (or assumed) aerodynamic properties and the inflow velocity at the rotor plane. Induction factors are used to modify the flow field near the blades due to interactions with the blades and the wake. These induction factors are obtained from equating expressions for thrust and torque from stream tube momentum analysis with the same expressions from the known blade aerodynamics. The thrust and torque are computed along increments of the blade, dr, and distributed over an infinitesimal annular ring, as shown in figure 1.2. Integrating the rings over the length of the blade results in a body force for the entire actuator disk. Numerically, the forces are discretized into grid points over a

porous actuator disk dependent on radial position but constant over an annulus. The lift and drag forces, equal in magnitude but opposite in sign, are then explicitly added to the model's momentum equations to parameterize the effects of the blade aerodynamics on the atmospheric flow. Tower and nacelle drag forces are also applied.
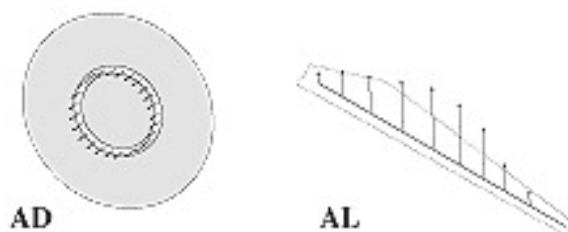
Figure 1.2: Illustration of the actuator disk (AD) and line (AL) concepts. (Sanderse et al., 2011)

Some actuator disk parameterizations do not include rotation (or torque) for simplicity and conservation of computational resources. Meyers and Meneveau (2010), in an LES context, showed the effects of tangential forces to be negligible in the case of a moderate power coefficient and high tip speed ratio. Porte-Agel et al. (2011), however, showed turbine rotation significantly improves prediction of mean velocity and turbulence intensity; the effect of rotation disappears farther downstream. The GAD, with rotation, was implemented and tested in WRF using an idealized set-up for a real world case with observation data (Mirocha et al., 2014). The intent was to create a computational framework capable of capturing atmosphere-turbine interactions in a realistic ABL environment provided by the WRF model. Further detail on the theory of the implementation can be found from the generalization of the Blade Element Momentum theory of Glauert (1963) by Madsen (1996), Sørensen et al. (1998), and Mikkelsen (2003).

Generalized Actuator Line Model

In order to improve wind turbine wake fidelity, especially in the near wake ($\approx$3 rotor diameters from the turbine), the actuator disk approach can be extended into the generalized actuator line (GAL) approach (Sorensen and Shen, 2002). Forces computed on the blades are not averaged over the actuator disk, as with the GAD, but are instead applied at the blades' location for each time-step, as shown in figure 1.2. The GAL enables resolution of distinct tip vortices, whereas the GAD, less accurately, sheds vorticity as a continuous sheet. This enables more realistic representation of near-wake physics with the GAL, which could lead to improved fundamental understanding of wake generation and evolution or use of the atmospheric forces occurring along the blade lines as input to a blade load model. Improved resolution of the near-wake physics may even effect atmospheric dynamics in the far-wake for certain weather conditions such as stable night-time flows. Past studies have shown the GAL to perform better than the GAD parameterization in the near wake, and both to perform

similarly in the far wake (Martınez et al., 2012; Troldborg et al., 2010). The potential benefit of the GAL parameterization needs to be evaluated against the GAD in WRF, particularly because the GAL requires much finer grid resolution in order to resolve each turbine blade.

1.3   Overview

This dissertation focuses on the development of a unified computational framework capable of realistically representing atmospheric dynamics important to wind energy applications from meso- to microscale. Chapter 2 investigates modeling parameters likely to influence mesoscale simulation results for two wind farms (one with simple and one with complex terrain) during a strongly forced synoptic and weakly forced local event; this allows investigation of the modeling parameters with regards to terrain and weather forcing sensitivity. Chapter 3 implements a microscale GAL parameterization to model wind turbine wake effects, and then compares the GAL with GAD results from previous studies. Chapter 4 unifies results from Chapters 2 and 3 to model a real array of wind turbines during a frontal passage by nesting from mesoscale weather boundary conditions to an LES domain with GAD turbine parameterizations. A brief summary of each chapter is provided in the following.

Chapter 2 uses WRF mesoscale simulations for case studies at two West Coast North American wind farms, one with simple and one with complex terrain. The case studies investigate both synoptically and locally-driven weather events at each site, while also including ramping events relevant to the wind industry. Observation data is used to test the performance of the model with different grid resolutions, turbulence closures, and nesting configurations. Simulation results did not improve significantly with higher grid resolution for the simple terrain site, however, there is marked improvement with increased resolution for the complex terrain site, but only during the locally-forced event. Consequently, computational resources could be conserved if the topography is adequately resolved at coarser resolution. Other parameters, such as soil moisture and two-way nesting, have a more significant effect on simulation results for the locally-forced event.

In Chapter 3, a GAL wind turbine parameterization is implemented into WRF with the purpose of enabling higher fidelity LES simulations of turbine interactions with realistic ABL conditions. The GAL is evaluated against a previously implemented GAD parameterization and measurements from two field campaigns, each of which measured the near-wake regions of a single turbine and allow for comparison during weakly convective and stable conditions, respectively. Similar aggregated wake characteristics are produced by the GAD and GAL for both stability classes, thus verifying proper implementation of the GAL. Each parameterization is compared by its ability to represent wake wind speed, variance, and vorticity distributions at the same fine grid resolution. The GAD is also compared at a coarser grid resolution only capable of resolving the actuator disk and not the turbine blade. The coarse-resolution GAD simulation shows slightly smaller and less persistent velocity deficits and substantially less variance and vorticity in the wake when compared to the finer-resolution GAD and GAL simulations. The GAL distinguishes itself from the fine-resolution GAD by

its ability to generate distinct tip and root vortices able to maintain coherence as helical tubes for about one rotor diameter downstream. This difference disappears at distances greater than approximately 2 rotor diameters downstream.

Building on Chapters 2 and 3, Chapter 4 implements a unified WRF meso- to microscale real-world computational framework for an array of wind turbines at a utility-scale Oklahoma wind farm. The GAD parameterization is modified to realistically function in a real simulation by making use of real terrain input, responding to operational cut-in and cut-out wind speeds, and obtaining the ability to yaw into the wind by utilizing an algorithm designed to replicate real turbine motion. Simulation results are compared to dual-Doppler measurements that provide three-dimensional fields of horizontal wind speed and direction. The model framework is able to produce realistic turbine wake effects, while differences with measurements can be attributed to the quality of the available weather and input/boundary data.

Chapter 5 provides a summary of the dissertation along with recommendations for future work.

1.4   Summary of Contributions

The main contributions of this work are the:

- Investigation of the importance and effects of common modeling parameters, such as grid resolution and turbulence closure, on simulation results relevant to the wind industry for different site conditions.

- Recommendations for wind energy operations that balance the conservation of computational resources against simulation accuracy for different situations (e.g. terrain complexity of the site, local vs. synoptic forcing).

- Improvements to the GAD parameterization in WRF to enable its use with real cases and more realistic turbine behavior (such as yaw, offset, etc.).

- Implementation of the GAL in WRF and evaluation against the GAD for its ability to improve the representation of the wind turbine wake for different site conditions.

- Introduction and evaluation of a unified computational framework able to perform mesoscale to microscale simulations for a wind farm, including both synoptic forcing (through grid nesting) and turbine wake effects (through a turbine parameterization).

Chapter 2

Investigation of Model Parameters for Wind Energy Forecasting[1]

2.1 Abstract

Wind power forecasting, turbine micrositing, and turbine design require high-resolution simulations of atmospheric flow. Case studies at two West Coast North American wind farms, one with simple and one with complex terrain, are explored using the Weather Research and Forecasting (WRF) model. Both synoptically and locally-driven events that include some ramping are considered. The performance of the model with different grid nesting configurations, turbulence closures, and grid resolutions is investigated through comparisons to observation data. For the simple terrain site, no significant improvement in the simulation results is found when using higher resolution. In contrast, for the complex terrain site, there is significant improvement when using higher resolution, but only during the locally-driven event. This suggests the possibility that computational resources could be spared under certain conditions, for example when the topography is adequately resolved at coarser resolutions. Physical parameters such as soil moisture have a very large effect, but mostly for the locally-forced events for both simple and complex terrain. The effect of the PBL scheme choice varies significantly depending on the meteorological forcing and terrain. On average, prognostic TKE equation schemes perform better than non-local eddy viscosity schemes.

---

[1]This chapter is a reproduction of the paper "Investigation of model parameters for high-resolution wind energy forecasting: Case studies over simple and complex terrain" by Nikola Marjanovic (the principal author), Sonia Wharton, and Fotini Katopodes Chow, published in the Journal of Wind Engineering and Industrial Aerodynamics, November 2014, Volume 134, pages 10-24 (Marjanovic et al., 2014), Copyright ©2014 Elsevier Ltd.

2.2   Introduction

Wind power forecasting benefits greatly from accurate predictions of atmospheric conditions at the heights spanned by wind turbines (~40-120m). Better simulation of the relevant physics could enable operational practices such as integration of larger fractions of wind power into power grids, scheduling maintenance on wind energy facilities, and defining design criteria for next-generation turbines and siting. Increases in available computational power have made high-resolution simulations of the atmospheric boundary layer more practical. The model operator, however, is required to make proper choices regarding model grid spacing, turbulence parameterization, land-surface representations and the configuration of initial and lateral boundary conditions for accurate simulations. The "proper" choice of these parameters is highly dependent on the situation under consideration.

As renewable energy sources begin to represent a larger fraction of the energy portfolio, additional strain is placed on the energy industry as these sources have to date been less predictable than traditional energy sources (Mahoney et al., 2012). Precise spatial analysis of weather events and improved weather prediction are crucial to both long and short-term energy management. Accurate short-term (minutes to days) forecasting increases the amount of wind power which can be integrated into electrical grid operations at a lower cost as it allows operators to make better real-time and day-ahead operations decisions. These decisions lead to a more efficient energy market by reducing the amount of polluting energy reserves (e.g., natural gas, coal) needed to maintain system security (Marquis et al., 2011).

This chapter analyzes and investigates some of the available parameters for atmospheric modeling for wind energy applications and their effects on predictions of wind speed at turbine hub heights for two case studies. We investigate several time periods which include ramping events at two wind farm locations on the West Coast of the United States, one over simple and the other over more complex terrain. "Ramping" refers to a rapid change in wind speed over a short time period and is of great interest to wind farm operators for preventing turbine fatigue and predicting power output. The exact definition of a ramping event varies in practice; examples include a 20% capacity change in production over a thirty-minute period (Freedman et al., 2008), or a pre-specified change in the magnitude of system-wide production. In this chapter, a ramping event is defined as an increase or decrease in wind speed of at least 7 m/s in less than 3 hours.

Atmospheric conditions have a large effect on the predictability of wind speed and ramping events. Meteorologically-driven wind and ramping events may be due to atmospheric motions at several scales. For example, thermally-driven winds such as sea breezes, mountain-valley circulations, or low-level jets occur at local scales, whereas the passage of a cold front is a synoptically-driven phenomenon. In all these cases, associated wind transitions may simply appear as large ramps in the wind speed time series to wind farm systems operators, though the cause for the wind changes can be quite different (Freedman et al., 2008). Larger, synoptically-driven features have longer time scales and are expected in theory to be more straightforward to forecast than local-scale phenomena, which usually require fine scale information about land-surface conditions and turbulent mixing in the atmosphere.

In addition to the synoptic conditions, local topography can significantly affect a model's prediction abilities. Many studies over complex terrain point to increasing grid resolution as a means to achieving better agreement of simulations with observations (Carvalho et al., 2012; Chen et al., 2004; Grell et al., 2000; Gronas and Sandvik, 1999; Mass et al., 2003), and this should be more important for locally-driven transitions. In contrast, low resolution mesoscale models may be adequate for many situations if the major features of the terrain are simple and adequately captured. The representation of subgrid turbulent motions and sub-grid features in the topography and land use can also play a role in a model's ability to accurately capture wind flow (Hanna and Yang, 2001).

There is uncertainty about the appropriate grid nesting strategy, including selecting adequate turbulence parameterizations and initialization data when moving to high resolution (Wyngaard, 2004). Another major challenge is conserving computational resources, especially when making ultra-high resolution forecasts, for example for predicting ramping events in the next few hours or days. Current models used by wind farm operators use a range of resolutions, often coarser than 1 km horizontally. This begs the question of whether this resolution is fine enough to capture the required flow features or whether computational resources could be saved by using coarser resolution. Accuracy is extremely important to wind power operators as improvements of just 1 m/s in wind speed forecasts can mean millions of dollars in savings because of financial penalties for both overestimating and underestimating power production. Suitable model configurations, however, may vary drastically depending on the terrain and other site conditions.

Here we perform simulations at two different sites for which terrain complexity varies greatly to develop insight into the ability to capture shifts in wind speed that are important to wind farm operators. The two sites are chosen to represent opposite ends of the spectrum in terms of terrain complexity, and two extreme types of forcings (locally weak and synoptically strong) are investigated at each site for the results to serve as a possible guide for a broad range of wind farms and forcing conditions. This study is relevant to wind energy forecasting in terms of day ahead forecasting. Short time periods are selected due to the computational cost of simulations at high resolutions. These time periods are chosen to be of interest to the wind industry by including ramping events with synoptic and local forcing to determine the importance of model parameters in each case. After exploring the model parameter space for these cases, a week-long simulation is performed for one group of settings to investigate longer time periods.

We use the Weather Research and Forecasting (WRF) model as our simulation tool (Skamarock and Klemp, 2008). WRF is intended mainly for mesoscale atmospheric simulations and includes large-eddy simulation (LES) capabilities. WRF has a fully compressible, Eulerian and non-hydrostatic equation set. Although we focus our study on only two wind farms, the farms are located in regions of high density, high MW wind power installation, making the results from this study meaningful to a large sector of the U.S. wind community. Our complex terrain wind farms are located in a region with at least 5,000 MW of installed capacity, while our simple terrain farm is in an area of at least 700 MW of installed capacity (American Wind Energy Association, 2012).

The simple terrain wind farm, with a 150 MW capacity, covers an area of about 10 km by 10 km with a fairly flat topography which includes a few hills with elevation variations of less than 150 m (see figure 2.1a). The complex terrain site spans a series of wind farms with over 500 MW installed spread across 37 km (north-south) by 53 km (west-east) and features much larger elevation differences of 1500 m (see figure 2.1b). Observation data are available from SODARs, meteorological towers, and cup anemometers on the turbine nacelles that can be used for comparison to numerical simulations. Wind speed accuracy is ± 0.5 m/s for SODAR and ± 0.3 m/s for cup anemometers. The turbine hub height for both wind farms is 80 m.
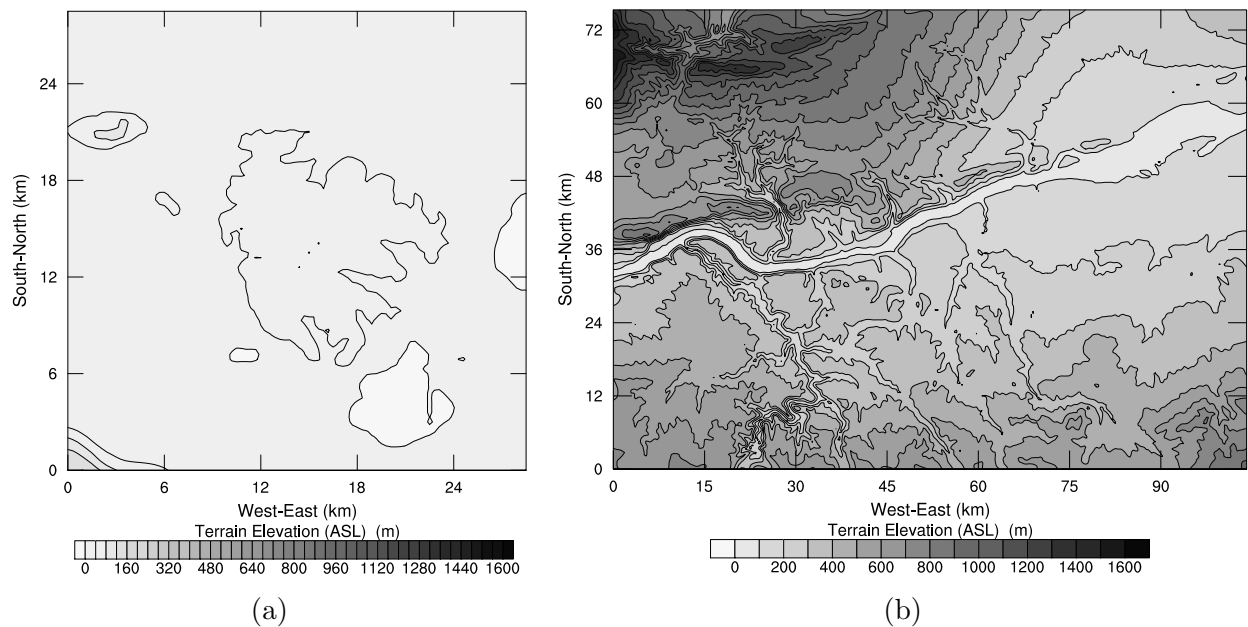
Figure 2.1: Wind farm topography for the 300 m horizontal resolution WRF domain comparing (a) the simple terrain site to (b) the complex terrain site.

The effects of horizontal and vertical grid resolution (section 2.4), 1-way vs. 2-way nesting (section 2.4), and turbulence closure models (section 2.4) are examined here. Results are presented below, along with discussion of the numerical setup and grid nesting approaches.

2.3 Numerical Simulation Setup

Grid nesting and topography

Four nested grids are used to simulate flow conditions for the wind farms at horizontal resolutions of 8.1 km, 2.7 km, 900 m, and 300 m. The main features of the topography become visible at 2.7 km for the simple terrain case and 900 m for the complex terrain, but fine structures become much better resolved at 100 m resolution for both cases (figure 2.1).

Topography was extracted from a 10 m resolution data set available from the USGS. The terrain is smoothed near the boundary for each nested sub-domain to match the elevations for the surrounding coarser grid. WRF uses a terrain-following, hydrostatic-pressure vertical coordinate system with the top of the model being a constant pressure surface. The vertical grid spacing is normally assigned by default by WRF, or it can be specified by the user to decrease spacing near the bottom of the model and stretch it near the top. The minimum vertical grid spacing ($\triangle z_{min}$) at the surface, as well as the average spacing ($\triangle z_{avg}$), are listed in table 2.1 for the grid configurations used. The domain height is approximately 13 km for the simple terrain case and 18 km for the complex terrain case to allow a larger damping region at the top of the domain (thus also requiring more vertical levels). The grids for the complex terrain site are larger so as to include more surrounding topographic features; the simple terrain site is not near any significant topographic features which would warrant a larger domain. Larger domains have been tested but have not shown any significant differences (not shown). This model setup is fairly standard for a nested WRF simulation. All the nested domains are the same size and centered within each other.

Several challenges are encountered with WRF over complex terrain. The terrain-following coordinates are considerably distorted near the surface over steep terrain which leads to numerical instability in the model. Reducing the time step, smoothing the terrain, and decreasing the vertical resolution near the ground were all attempted but resulted in significant distortion or excessive run time. The most effective option in our case is to adjust the time off-centering in WRF that weights (forward in time) the vertically-implicit acoustic-time-step terms in the model to damp instabilities associated with sound waves and sloping model levels (Dudhia, 1995; Durran and Klemp, 1983). The off-centering is accomplished by using a non-zero, positive coefficient in the acoustic time-step vertical momentum equation and geopotential equation.

Computational time

The computational time for these simulations is reasonable for short-term forecasting applications. The smaller simple terrain site needed about 9 hours of wall time for a 48 hour simulation, while the complex terrain site needed about 43 hours of wall time for a 48 hour simulation. Simulations for both sites used 144 processors for the 4 concurrently simulated domains (1:3 nesting ratio used for horizontal and temporal resolutions).

Initialization and lateral boundary conditions

Initial and boundary conditions were obtained from the National Center for Atmospheric Research (NCAR) North American Regional Reanalysis (NARR) data. NARR is available at 32 km horizontally at 29 vertical levels (1000-100hPa; excluding surface) to force the WRF simulations at the coarsest grid. Lateral boundary condition forcing was applied at three-hour intervals and linearly interpolated in between. Relaxation towards the lateral boundary values was applied around the edge of the domain. Simulations were performed

for 48 hours for the short term events and for an extra 120 hours for the week-long statistical analysis. Output was stored at ten-minute intervals and used to generate initial and boundary conditions for the nested grids. Simulations using NAM for initialization were also performed, but the overall conclusions were similar (not shown).

Surface characteristics

WRF uses 33 land use categories (including ice and water) from USGS. The simulations use National Land Cover Database (NLCD) data at 30 m resolution which is mapped from the native 19 land use categories to the USGS 33 land use categories. The Noah Land Surface Model was used with initial moisture and soil temperature in four layers interpolated from NARR. Land-atmosphere coupling effects on the boundary layer, such as soil moisture initialization, can have a significant effect on simulation results, and at finer resolutions it may be necessary to use finer-scale soil initialization fields (Chow et al., 2006; Williams et al., 2009; Woodward et al., 2009). Section 2.4 examines the role of soil moisture on the model results.

Turbulence

WRF provides several turbulence closure options for the Reynolds-Averaged Navier Stokes (RANS) equations of motion. These closures are referred to as Planetary Boundary Layer (PBL) schemes and they parameterize vertical turbulence diffusion (or vertical mixing) in physical space. All the PBL schemes make use of second order horizontal diffusion on the model levels, where gradients are simply taken along coordinate surfaces. The horizontal eddy viscosity is determined from horizontal deformation using a Smagorinsky first-order closure approach.

Several of the PBL schemes use a prognostic turbulence kinetic energy (TKE) closure that predicts the sub-grid TKE using a TKE equation to obtain the vertical eddy viscosity. These include the base case Mellor-Yamada-Janjic (MYJ) scheme (Janjic, 1994), the Quasi-Normal Scale Elimination (QNSE) PBL (Sukoriansky et al., 2005), the Mellor-Yamada Nakanishi and Niino Level 2.5 (MYNN2) and 3 (MYNN3) PBLs (Nakanishi and Niino, 2006), the Bougeault-Lacarrere (BouLac) PBL (Bougeault and Lacarrere, 1989), the University of Washington (UW) scheme (Park and Bretherton, 2009), and the Grenier-Bretherton-McCaa (GBM) scheme (Grenier and Bretherton, 2001). Unlike the prognostic TKE PBLs, the Yonsei University (YSU) scheme (Hong et al., 2006) and its predecessor, the Medium-Range Forecast (MRF) model (Hong and Pan, 1996), are both non-local vertical eddy viscosity schemes. The Asymmetric Convective Model (ACM2) (Pleim, 2007) uses a hybrid approach with non-local upward mixing and local downward mixing. The Total Energy Mass Flux (TEMF) scheme (Angevine et al., 2010), which uses a sub-grid total energy prognostic variable with mass-flux type shallow convection, is also tested, but is numerically unstable for the synoptically-forced complex terrain case and is not compared in this work. All the PBL schemes compared in this work (see section 2.4) make use of the Noah land surface model

and use the recommended surface-layer physics option in WRF (which is particular to each PBL scheme). ACM2 makes use of the MM5 Monin-Obukhov surface-layer scheme instead of its recommended surface-layer scheme, because the recommended scheme is designed for the Pleim-Xiu land surface model (which is not used in this study).

2.4 Comparison with Observation Data

Results comparing simulations with observation data for the two-day events are given in this section. Four main cases will be described: a locally-forced and a synoptically-forced case for both the simple and complex terrain. These events occur during four different selected time periods. The naming convention for each case is explained in table 2.2, along with a brief description of the ramping. Case CTL does show rapid changes in wind speed, but the magnitude of the wind speed is too low to consider any of these changes ramping events by our definition of a 7 m/s wind speed change.

For each simulation period, a number of different model configurations is tested, using different resolutions, grid nesting, vertical levels, and turbulence closure models. The naming convention for these runs is "(finest horizontal resolution)_(number of points in vertical)", as shown in table 2.3. Note that the base case simulation for the simple terrain (ST) site uses 49 vertical levels, while the base case simulation for the complex terrain (CT) site uses 54 vertical levels due to the different domain heights. All the results are from 1-way nesting and the Mellor-Yamada-Janjic turbulence model unless otherwise noted. The week-long simulations (section 2.4) are an extension of their respective short-term cases for 5 additional days.

Comparison strategy

A Doppler mini SODAR (Model4000, Atmospheric Systems Corporation, Santa Clarita, CA) collected high vertical resolution, three-axis wind velocity data at a 1 Hz per beam sampling resolution. SODAR data were averaged over 10-minute intervals to calculate mean horizontal and vertical wind speed, direction, latitudinal, longitudinal and vertical turbulence intensities, and turbulence kinetic energy at 10 meter intervals at heights 20-200 m above ground level (AGL). The data was quality controlled according to accepted SODAR standards (Antoniou et al., 2003; Wharton and Lundquist, 2012a). SODAR 10-minute intervals are compared with instantaneous model output at 10 minutes.

The time series and profile figures in the next few sections are located at the SODAR site, at the center of each domain, and are representative of other locations in the domain. SODAR data are available at 10 meter intervals from 20-200 m AGL, however at elevations above 100 m the data are sparse. To quantify the comparisons, error tables (such as table 2.4) show the root-mean-square errors (RSME) and mean absolute errors (MAE) between the SODAR data and the simulations over 20-200 m above the ground, averaged over 48 hours. They are defined as:

	Simple Terrain				Complex Terrain			
$\triangle h$ (m)	(nx,ny,nz)	$\triangle z_{min}$ (m)	$\triangle z_{avg}$ (m)	$\triangle t$ (s)	(nx,ny,nz)	$\triangle z_{min}$ (m)	$\triangle z_{avg}$ (m)	$\triangle t$ (s)
8100	(96,96,49)	35	246	30	(348,252,54)	32	232	30
2700	(96,96,49)	35	246	10	(348,252,54)	32	232	10
900	(96,96,49)	35	246	3.33	(348,252,54)	32	232	3.33
300	(96,96,49)	35	246	1.11	(348,252,54)	32	232	1.11
300	(96,96,40)	60	309	1.11	(348,252,40)	63	402	1.11
300	(96,96,70)	10	177	0.74	(348,252,70)	12	228	1.11

Table 2.1: Simulation parameters for each grid resolution for both the simple and complex terrain sites.

Abbreviation	Description of Event	Actual Ramping Time	Actual Ramping Magnitude
STS	**S**imple **T**errain case, **S**ynoptically-forced	Frontal passage 24 hours into simulation (3 hrs after sunrise)	4 to 16 m/s in 3 hrs
STL	**S**imple **T**errain case, **L**ocally-forced	Appears 37 hours into simulation (10 min after sunrise)	10 to 3 m/s in 3 hrs
CTS	**C**omplex **T**errain case, **S**ynoptically-forced	Cold front 10 hours into simulation (4 hrs before sunrise)	10 to 20 m/s in 2 hrs
CTL	**C**omplex **T**errain case, **L**ocally-forced	no ramping	no ramping

Table 2.2: Abbreviations and event descriptions for the different cases investigated.

Run name	Configuration
300m_49	simple terrain (ST) base case simulation, 4 1-way nested grids, 49 vertical levels, 300 m horizontal resolution
300m_54	complex terrain (CT) base case simulation, 54 vertical levels
300m_70	70 vertical levels
300m_40	40 vertical levels (chosen by WRF)
300m_49_2way, 300m_54_2way	4 2-way nested grids
900m_49, 900m_54	900 m horizontal resolution, 3 1-way nested grids
2700m_49, 2700m_54	2700 m horizontal resolution, 2 1-way nested grids
8100m_49, 8100m_54	8100 m horizontal resolution, 1 grid
300m_49_sat, 300m_54_sat	all grids initialized with saturated soil
300m_49_dry, 300m_54_dry	all grids initialized with dry soil

Table 2.3: Simulation configurations and naming (everything is the same as base case unless otherwise noted).

$$MAE = \frac{1}{M} \sum_{j=1}^{M} \frac{1}{N} \sum_{i=1}^{N} |A_{i,j} - B_{i,j}|$$

$$RMSE = \sqrt{\frac{1}{M} \sum_{j=1}^{M} \frac{1}{N} \sum_{i=1}^{N} (A_{i,j} - B_{i,j})^2}$$

where M is the number of time steps; N the number of vertical grid points; A observation data; and B simulation data. RMSE and MAE may be insufficient for evaluating model performance during ramp events, although industry practice still heavily relies on these metrics. Newer techniques, including the critical success index, need to be further developed and studied to evaluate ramp forecasts (Marquis et al., 2011). The evolution of wind speed and wind direction during these events is presented in figures (such as figure 2.3) comparing different cases at 80 m AGL. The observations are, in most sections, compared to 1-way nested run resolutions: 300m (4 grid nests), 900m (3 grid nests), 2700m (2 grid nests), and 8100m (1 grid).

Effects of resolution

Topography resolution

The required grid resolution depends greatly on the nature of the local topography. The chosen horizontal resolutions (see table 2.1) seem to easily capture the topography of the simple terrain site. Figure 2.2a shows how all the resolutions, fine and coarse (except for the 8100 m case), capture the hill and general topography of the wind farm quite well. Conversely, it is not as easy to capture the terrain of the complex topography site (figure 2.1b). Figure 2.2b indicates that the coarser horizontal resolutions (8100m and 2700m) do not capture the complexity of the terrain, but the finer resolutions do.

Effects of horizontal resolution during locally-forced events

We first examine locally-forced events over simple (Case STL) and complex terrain (Case CTL) and compare output from 1-way nested runs to evaluate the impact of grid resolution. Case STL shows an increase in wind speed on the first day at 16 UTC that is slightly more gradual and starts earlier than what is shown by the SODAR and does not capture the minimum wind speeds observed by the SODAR (see errors in table 2.4 and figure 2.3a). The down-ramping event on day 2 from 13 UTC to 16 UTC, where the wind speed decreases from 10.5 m/s to 3 m/s, is well captured by the simulations when compared to the observations, however, the minimum of the ramp is not. Case CTL corresponds well with the SODAR for most of the first day including the increase in wind speed from 17 UTC to the end of the day, but fails to capture the lower wind speeds the observations show for the second day and instead shows a large increase in wind speed.

(a) Simple terrain (ST) site

(b) Complex terrain (CT) site
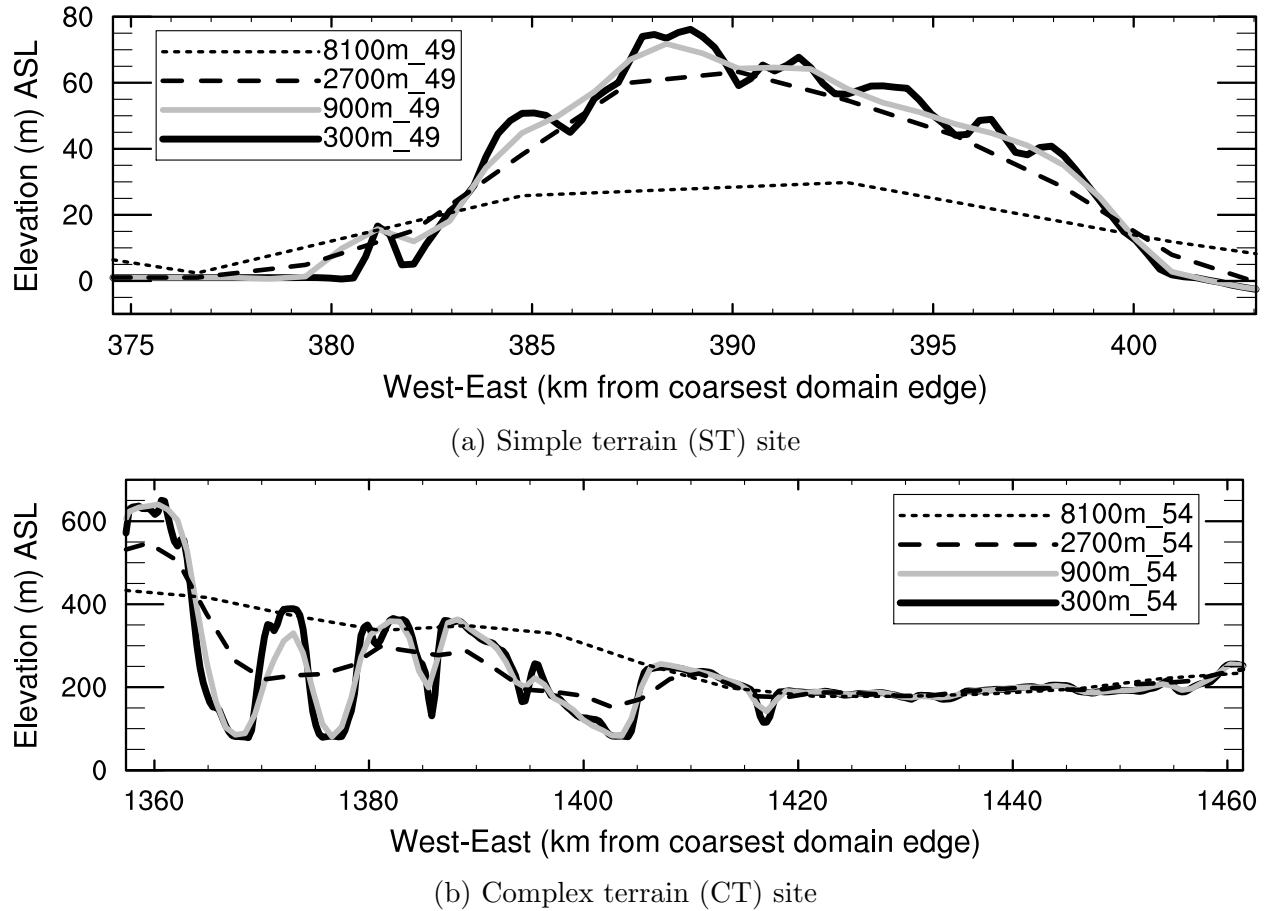
Figure 2.2: West-East cross-section of topography through the center of the 300 m resolution domain for simulations at different horizontal resolutions (see table 2.3).

The difference in performance for the various grid resolutions for Case STL is small, as seen in the error metrics listed in table 2.4. The results are very similar across all resolutions with the finest producing a slightly smaller error than the coarser ones preceding it. This is somewhat surprising as we expected to see more distinct differences between the resolutions. The vertical profiles in figures 2.4a and 2.4b show time slices at the SODAR location from two different times, with varying levels of agreement with the SODAR. Under these conditions relatively coarse horizontal resolution (2.7 km) appears to be adequate for capturing the shift in wind speed at the wind turbine hub heights (~80-100 m) for Case STL as there is little improvement for the finer resolutions. These results agree with other simulations such as those from Yver et al. (2013), which showed improvement from 12 km horizontal resolution to 4 km but not from 4 km to 0.8 km for a California coastal area. Deppe et al. (2012) did not register any improvement from 10 km to 4 km horizontal resolution for their simple terrain site in Iowa. The terrain is adequately resolved on all grids in the simple terrain case

and the mean flow patterns are very similar.

The dependence on grid resolution for Case CTL is much more significant as the error metrics show in table 2.4. In this case the two finer resolutions (900 and 300 m) compare better to the SODAR observations than the two coarser resolutions, as shown in figures 2.3c and 2.3d. The improvement from 8100 m to 2700 m resolution is most noticeable, while improvement from 2700 m to 900 m is less and 900 m to 300 m even less. The vertical profiles in figures 2.4c and 2.4d show two different time slices at the SODAR location; Case CTL shows a clear advantage to using high resolution simulations during certain times of the day, particularly resolution finer than 8100 m. It is worth noting in the vertical profiles (figure 2.4) that WRF may not always accurately capture the magnitude, but does somewhat more accurately represent the vertical wind shear profile. More accurate comparisons to the SODAR are observed with finer resolution in complex terrain because the details of the topography are better resolved, which can dramatically influence winds.

Case STL seems to predict wind speeds close to those of the SODAR but the timing is slightly off for the increased wind speed event that starts at 16 UTC on the first day and wind speeds are over-predicted just before the increase when comparing to observations. While there is clear improvement with higher resolution in the first hours, Case CTL over-predicts wind speeds after the first 25 hours of the simulation and skews MAE and RMSE calculations so that the finest resolution does not give the lowest value. Errors calculated separately for just the first day show much smaller values (table 2.4). These inaccuracies are later found to be at least partially attributed to misrepresentation of soil moisture in WRF (see section 2.4).

Effects of vertical resolution during locally-forced events

Vertical spacing may have a significant effect on the accuracy of wind speed and direction predictions, particularly when wind shear is strong, e.g. in the case of nocturnal low level jets which can also be responsible for ramping events (Storm et al., 2009). To examine the need for high vertical resolution in high-shear regions, 4 sets of grids (with 1-way nesting) are examined. The grids were generated as follows: 300m_49 (and 300m_54) uses a $tanh$ function to stretch the vertical grid spacing so that there is minimum spacing near the ground of ˜30 meters which is stretched higher up into the atmosphere; 300m_70 uses specified grid levels that provide spacing of about 10 m in the lowest 200 m of the atmosphere and then stretched above (for Case STL) or start at 10 m and are stretched above (for Case CTL); 300m_40 is created by specifying 40 levels in WRF and using the default spacing (the minimum spacing is ˜55 m and average spacing is ˜309 m). Figure 2.5 shows the evolution of wind speed. Table 2.5 shows the RMSE and MAE between simulations and observations along with the average vertical spacing in the range where observation data exists (20-200m). Surprisingly, the grids all give very similar results for the Case STL ramping event, with the lower resolution 300m_40 providing slightly worse results. The less computationally intense option in this case appears adequate for predicting ramping. This agrees with other studies such as Floors et al. (2013), which compared 41 vertical levels against 63 vertical levels within

lidar range over the simple terrain coast of Denmark and found almost no improvement with vertical resolution.

Case CTL shows quite a bit more variation with vertical resolution. Table 2.5 appears to show that the WRF chosen 40-level setup gives the most accurate results followed by the 70 vertical levels stretched case, and finally the 54-level *tanh* stretched case. However, if the second day (during which the simulations over-predict the wind speed due to land-surface conditions mismatch between WRF and observations [discussed in section 2.4]) is excluded, the different resolutions seem to perform similarly, with the two finest vertical resolutions outperforming the coarser resolution. This suggests that for locally-forced complex terrain cases the results benefit slightly from an increase in the number of vertical levels used. The differences from changing the vertical resolution appear less significant than the horizontal resolution effects described above. Zhang et al. (2013a) and Talbot et al. (2012) made similar conclusions from their simulations over complex terrain, where increased vertical resolution improved comparisons to observations to some degree, but not as significantly as horizontal resolution.

Effects of horizontal resolution during synoptically-forced events

In this section we compare the effects of horizontal resolution in simulating the two synoptically-forced events. Once again output is compared from 1-way nested runs to evaluate the impact of grid resolution for both simple and complex terrain. The SODAR observations of the evolution of wind speed 80 m above the surface are presented for Case STS (figure 2.6a) and Case CTS (figure 2.6b). Simulations for Case STS compare rather well with the SODAR observations at all resolutions as the errors in table 2.6 show. All resolutions accurately capture the major ramping event at 18 UTC to 21 UTC on the second day, where wind speed increases from 4 m/s to 16 m/s, and match the observations quite well over the rest of the simulation. A cold frontal passage results in the increase in wind speeds for Case CTS at about 12 UTC on the first day and passes the next day at about 12 UTC as the ramping indicates. The simulation for Case CTS corresponds with SODAR observations with almost all grid resolutions as the error comparison in table 2.6 indicates. The simulations are slightly off in capturing the large ramping event on the first day from 10 UTC to 12 UTC, where wind speed increases from 10 m/s to 20 m/s. The largest differences between the resolutions are observed at 2 UTC on the second day, but there is no observation data for that time period. The MAE error for Case CTS of around 3.5 m/s is likely due to a forcing problem (initial/boundary conditions) because the different resolutions give very similar results for quite complex terrain. Most of the errors occur at the ramp up or after the cold front. Zhang et al. (2013a) also found that the magnitude of errors is generally greater in the strong forcing than weak forcing cases as the errors appear more closely related to the influence of the weather systems.

It is of note that noticeable differences are observed with grid resolution for the complex terrain case during local forcing (section 2.4) but not during synoptic forcing. It may be that lateral boundary condition errors dominate under strong synoptic forcing. It is not

surprising that Case STS does not show any improvement with increased resolution when Case STL did not show any either due to the ease with which the various resolutions capture the simple terrain. Furthermore, the simulations for the synoptically-forced cases do not deviate as much from the observations as the locally-forced cases discussed previously. The strong synoptic forcing likely dominates over any other local forcing parameters that might have a significant effect on the wind fields such as soil moisture variation.

Effects of land-surface conditions during locally-forced events

Overall, there appear to be relatively small differences between results from different grid configurations except for the locally-forced complex terrain (CTL) case, as described above. Both locally-forced events, however, showed large errors when compared to SODAR observations. This is especially true in capturing the lower wind speeds at hub height (˜80 m), so there is certainly room for improvement in the simulations. Here we examine the effect of land-surface forcing for Cases STL and CTL. These simulations are designed to test the role of soil moisture in the locally-forced cases, which are anticipated to be more sensitive to land-surface forcing (Chow et al., 2006). Two soil moisture extremes are compared to the base case for both locally-driven terrain cases. In one extreme, the initial soil moisture value is set to 90 percent or almost fully saturated for the whole domain and left to adjust in time according to soil type. In the other extreme, the soil moisture value is initialized at 0.02 percent or almost completely dry for the whole domain. Figure 2.7a shows that when the soil for Case STL is initialized as dry, it over-estimates the wind speeds slightly more than the base case. When Case STL is initialized as saturated, however, it is much better able to match the full extent of the down-ramping at 16 UTC on the second day, while not capturing the later peaks as well. For the complex terrain domain, figure 2.7b shows that saturated initial conditions for Case CTL yield results similar to the base case. The dry soil initialization, 300m_54_dry, however, captures the minima of the SODAR much better for the second day. The dry case shows reduced error when compared to the base and saturated cases as shown in table 2.7. The surface energy fluxes can be drastically affected by the soil moisture and strongly influence wind speeds at hub-height. This suggests that hub-height winds are sensitive to soil moisture and that accurate representation of land-surface conditions may be just as important for accurate simulations in this case, rather than just looking at differences in resolution or other model configuration parameters.

Difference between 1-way and 2-way nesting

In 1-way nesting, the finer domains do not influence the parent domains. With 2-way nesting, the finer grid feeds information back to the coarser parent domain. The coarser grid is then updated with higher resolution fields which theoretically leads to a more accurate simulation result. 2-way nesting is thought to be important when fine-scale features that are resolvable on the finer domain affect meteorological conditions on a larger scale. Harris and Durran (2010) found that 2-way nesting is in general superior to 1-way nesting in an

| Resolution | Simple Terrain Case (STL) | | Complex Terrain Case (CTL) | | | |
| | MAE | RMSE | MAE | RMSE | MAE | RMSE |
					1st day	
300m	2.14	2.57	2.19	3.06	0.83	1.05
900m	2.16	2.57	2.10	2.93	0.95	1.19
2700m	2.17	2.62	2.31	3.17	1.12	1.43
8100m	2.27	2.74	3.24	3.88	2.04	2.28

Table 2.4: MAE and RMSE (m/s) for horizontal wind speed compared to SODAR over 48 hours for locally-forced simple and complex terrain cases (STL and CTL) at different horizontal resolutions.

| Resolution | Simple Terrain Case (STL) | | | Complex Terrain Case (CTL) | | | | |
| | MAE | RMSE | Avg. Vertical Spacing in 0-200m range (m) | MAE | RMSE | MAE | RMSE | Avg. Vertical Spacing in 0-200m range (m) |
						1st day		
300m	2.14	2.57	38.05 (5 points)	2.19	3.06	0.83	1.05	42.95 (5 points)
300m_40	2.19	2.65	73.50 (3 points)	1.90	2.72	1.03	1.28	75.65 (3 points)
300m_70	2.15	2.57	9.90 (20 points)	2.06	2.89	0.80	1.00	19.53 (11 points)

Table 2.5: MAE and RMSE (m/s) of horizontal wind speed for different vertical resolutions of the locally-forced simple and complex terrain cases (STL and CTL) compared to SODAR over 48 hours.

| Resolution | Simple Terrain Case (STS) | | Complex Terrain Case (CTS) | |
	MAE	RMSE	MAE	RMSE
300m	1.65	2.28	3.50	4.26
900m	1.60	2.21	3.55	4.29
2700m	1.60	2.12	3.39	4.15
8100m	1.73	2.25	3.54	4.36

Table 2.6: Horizontal wind speed MAE and RMSE (m/s) over a 48 hour period for a synoptically-forced event over simple and complex terrain (STS and CTS) comparing different horizontal resolutions to SODAR.

idealized comparison of the linear 1-D shallow-water model. 1-way nesting performs better only when very poorly resolved waves strike the nest boundary. Liu et al. (2011) tested WRF-LES for wind energy with data assimilation over real terrain and compared 1-way and 2-way nesting. They found that, in general, 2-way nesting agrees best with the observations.

Figure 2.8 shows time series of wind speed for the 1-way nested base case and the 2-way nested case each with the same four nesting levels. Under strong synoptic-scale forcing, it is likely that 1-way nesting will be adequate for feeding information from the larger scales to the finer scales. Case STL (simple terrain locally-driven forcing) in figure 2.8a shows an insignificant difference between 1-way and 2-way nesting even with local forcing. The similarity is most likely due to the negligible benefit of finer horizontal resolution (see section 2.4) for this case that results from the simplicity of the topography. Case CTL (complex terrain locally-driven forcing), in figure 2.8b, shows a noticeable improvement with 2-way nesting when compared to the 1-way nested base case. Table 2.8 quantifies these differences and indicates that the terrain at finer resolutions affects the coarser domain results because improvement with higher resolution is observed in this case due to the complexity of the terrain. There is little difference between 1-way and 2-way nesting for both synoptically-forced simulations, Cases STS and CTS, where the strong synoptic forcing overwhelms any local influences on winds due to terrain complexity.

Comparing WRF Planetary Boundary Layer (PBL) schemes

Other works have examined the effects of Planetary Boundary Layer (PBL) schemes in WRF (see section 2.3 above for descriptions) and most have found that no single PBL scheme can be recommended for all circumstances as each scheme has its own strengths and weaknesses (Yver et al., 2013; Zhang et al., 2013a). Xie et al. (2013) compared two nonlocal mixing schemes, YSU and ACM2, with two local mixing PBL schemes, MYJ and MYNN2, at 3 km horizontal resolution over Southeast England for numerous stability conditions. They found that local PBL schemes considerably underestimate the entrainment heat fluxes for convective cases, while the nonlocal schemes exhibit stronger mixing and agree better with large-eddy simulation studies. However, the 10 m wind speed RMSE values for the four schemes for the months of June and November vary by less than 0.1 m/s and were quite similar for all the cases. Yver et al. (2013) compared 4km horizontal resolutions of the YSU, MYJ, QNSE, MYNN2, ACM2, BouLac, UW, and TEMF schemes over a one month period along the California Coast and found that all the schemes present similar results and generally agree with the observations. Xie et al. (2012) compared the YSU, ACM2, MYJ, and BouLac PBL schemes over Hong Kong for June and November at 1 km resolution. The 10 m wind speed RMSE showed that ACM2 and YSU perform slightly better than MYJ and BouLac by about 0.25 m/s. Most other works looked at wind speed comparisons near the surface at 10 m elevation, where surface friction effects are strong, because of the availability of data, but Deppe et al. (2012) compared the YSU, MYJ, QNSE, MYNN, and ACM2 PBL schemes with ensemble simulations at turbine hub height (80 m) in Iowa at 10 km horizontal resolution. They found that nonlocal schemes (YSU and ACM2) overall performed better

than local PBL schemes (MYJ, QNSE, MYNN) by MAE differences of about 0.15 m/s on average for month long simulations. Here we compare almost all the PBL schemes available in WRF at turbine hub height at fine horizontal and vertical resolution and at the simple and complex terrain sites.

Figure 2.9 shows how the different PBL schemes in WRF perform in each of the four cases tested at 300 m horizontal resolution. The RMSE for each case (STL, STS, CTS, and CTL) along with the average of all the cases (Total AVG) is shown for each PBL scheme. The average of all the cases (Total AVG) is calculated based on the time duration of each case (Case CTL has half the weight of the other cases because we only consider the first 24 hour period for which the results are reasonable and not the full 48 hours). The PBL schemes are ordered along the x-axis from lowest case average RMSE to highest case average RMSE (left to right) with the average RMSE indicated below the PBL scheme name in units of meters per second. The GBM PBL scheme performs the best with the lowest averaged RMSE of 2.54 m/s compared to the base case MYJ PBL scheme, which is third best with an average RMSE of 2.74 m/s. The PBL schemes all seem to perform rather similarly with less than 0.14 m/s RMSE separation between each scheme, except for the poor performance from the MRF PBL which is 0.28 m/s worse than the second to worst performer (YSU). MRF is a legacy PBL scheme in WRF and is improved on by YSU. Neglecting MRF, the different PBL schemes differ less than an average RMSE of 0.5 m/s for the tested cases, though this difference could be significant from a forecasting perspective. The TKE based PBL schemes seem to cluster together and overall outperform the non-local vertical eddy viscosity schemes (YSU and MRF), which perform the worst. The ACM2 scheme, which uses a hybrid approach, places fourth overall with an average RMSE of 2.78 m/s.

Certain PBL schemes perform better for specific cases. GBM does particularly well for Case CTS, however, all the schemes have their highest RMSE error for this case. MYJ has the lowest RMSE for Case CTL, and all the PBL schemes have their lowest RMSE error for this case except MRF. ACM2 does best for Case STL along with the MYNN schemes, and UW outperforms the others for Case STS. The PBL schemes, for the most part, do not show any significant improvement from 2700 m to 300 m horizontal resolution for all the cases except Case CTL. The average RMSE improvement, if any, for Cases STL, STS, and CTS does not exceed 0.025 m/s with the largest single improvement for a scheme not exceeding 0.18 m/s (QNSE for Case STL, with MYJ's 0.08 m/s improvement coming in second). MRF is the only exception with a 0.6 m/s improvement for Case CTS, but this scheme performs much worse than any other scheme in this case (QNSE's 0.11 m/s improvement is second highest). The PBL schemes show more significant improvement with resolution for Case CTL with an average RMSE improvement of 0.39 m/s. The largest improvement is 0.66 m/s for GBM and YSU, while the smallest improvement is 0.16 m/s for UW.

It is difficult to recommend one PBL scheme for every situation, but general guidelines can be extracted from this comparison. The TKE based PBL schemes clearly outperform the non-local vertical eddy viscosity schemes. MRF has a significantly higher average RMSE than the rest of the schemes and this is mostly a result of its particularly poor performance for the complex terrain cases. While its RMSE is closer to average for the simple terrain

cases, it is never in the top four PBL schemes. It is not recommended to use the MRF PBL scheme for wind energy applications. YSU's average RMSE error is closer to the other PBL schemes than MRF's, but it too never rates better than fifth place for any of the cases. However, it does not show the large errors associated with MRF for the complex terrain cases and might be an acceptable alternative for cases in which computational resources are limited, because it does not calculate the TKE equation. It is still not recommended for periods dominated by stable conditions, because the use of a non-local eddy viscosity scheme is not best suited to cases where the turbulent eddies are of a smaller scale than the vertical grid spacings of the model (Pleim, 2007). ACM2 is a top performer in this study, especially for Case STL. It is able to switch between stable conditions (local eddy diffusion as in MYJ) and unstable conditions (local and nonlocal transport). MYJ, the base case, performs respectably by coming in third overall with an average RMSE of 2.74 m/s and does particularly well for Case CTL. It is a good base case choice because it makes use of the TKE equation and is the second oldest scheme implemented into WRF after MRF.

Effects of grid resolution on week-long simulations

In addition to short-term forecasts, there is interest in longer-term performance of simulations to assist with forecasting and wind resource characterization. A week-long simulation is performed using the locally-driven simple and complex terrain test cases to further examine grid resolution effects on predicted disturbances of wind speed and turbulence intensity distributions for a specific site. The simulation is for 7 days after the start of Case STL and Case CTL respectively. Changes in long-term distributions could be useful for more detailed site evaluations for turbine placement.

Week-long results for wind speed

The results obtained from week-long simulations for horizontal wind speeds fall in line with the shorter term 48 hour simulations. The finer resolution runs for Case STL show little variation in wind speed distributions from the coarser resolutions as shown in the probability density function (PDF) in figure 2.10a though there is an advantage to using 2700 m or finer grid spacing for representation of faster, less frequent winds as suggested in the error metrics (table 2.9). The PDFs are created at hub height above ground and binned into 18 equally spaced bins that span the minimum and maximum range for each category at the SODAR location during a week of summer. They all show, along with the SODAR, that during this summer week, wind speeds are rather high and favorable for producing wind energy.

The week-long simulations for Case CTL also show similar results compared to the shorter term 48 hour simulations. Figure 2.10b and table 2.9 show improvement with higher resolution, though the improvement beyond 900 m is small. Zhang et al. (2013a) looked at errors in 10 m surface wind from WRF simulations in complex terrain for both 3 day and month long simulations for horizontal resolutions ranging from 27 to 1.11 km. They found that higher resolution simulations do not outperform coarser simulations in many cases most

likely because of the inability of the numerical model to depict near-surface structures even with better terrain representation. Yver et al. (2013) also found that there is improvement in month-long simulations from 12 km to 4 km horizontal resolution, but not from 4 km to 0.8 km.

Week-long results for turbulence intensity

Turbulence intensity is also vital to consider in determining potential wind farm locations, because a value that is too high (roughly greater than 20% of the mean wind speed) will result in feathered wind turbines to avoid damage (and hence a loss in power production). The definition of turbulence intensity is:

$$TI = \frac{\sqrt{\sigma_u^2 + \sigma_v^2 + \sigma_w^2}}{U_{mean}} \qquad (2.1)$$

where U_{mean} is the average horizontal wind speed over a time period, $\sigma_u; \sigma_v; \sigma_w$ are the standard deviations of wind speed over that same time period in the East-West, North-South, and vertical directions respectively. The turbulence intensity for the SODAR is calculated by averaging the wind speed at every recorded second over a 10 minute period and calculating the standard deviation of each component of wind speed. The turbulence intensity for the simulations is obtained using WRF's output of TKE from MYJ, $\frac{\sqrt{TKE}}{U}$.

As figure 2.11a shows, there is little difference in the distribution of TKE among the various resolutions (except the coarsest 8100 m case) for Case STL. They all show similar results and estimate probability areas close to the SODAR. The peaks for the turbulence intensity are slightly off, with the simulations predicting slightly lower turbulence intensity when compared to the SODAR. However, as the number of bins increases the peaks come closer together. This site seems to be almost ideal during this particular time of year for wind turbines, as turbulence intensity only exceeds 20% less than 4% of the week.

The week-long simulations for Case CTL, shown in figure 2.11b, appear to greatly under-predict turbulence intensity for the time period. The finer resolutions are slightly better compared to the SODAR observations and predict a greater occurrence of higher turbulence intensity for the week. Overall, the simulations seem to under-predict higher instances of turbulence intensity. This could be a problem when evaluating potential turbine siting locations, as Case CTL shows the simulations predict turbulence intensity exceeding 20% only about 20% of the week while observations show this threshold exceeded about 75% of the week. It is important to note that the SODAR turbulence measurements have a degree of uncertainty. These uncertainties generally bias the turbulence intensity magnitudes towards higher values (see Wharton and Lundquist (2012a) for full discussion). The observations show more instances of low wind speed than the simulations (figure 2.10b); this may be why turbulence intensity for the observations is much higher than for the simulations, because for the same standard deviations of the wind speed components, lower wind speed (see denominator of equation 2.1 above) results in higher turbulence intensity even when there may not be more turbulence. However, even when wind speeds are higher for both (as in Case

	Simple Terrain Case (STL)		Complex Terrain Case (CTL)	
Resolution	MAE	RMSE	MAE	RMSE
300m	2.14	2.57	2.19	3.06
300m_sat	1.54	1.95	2.22	3.10
300m_dry	2.67	3.27	1.37	1.87

Table 2.7: Horizontal wind speed MAE and RMSE (m/s) for locally-driven simple and complex terrain (STL and CTL) cases comparing different soil moisture initializations to SODAR over a 48 hour period.

	Simple Terrain Case (STL)		Complex Terrain Case (CTL)	
Resolution	MAE	RMSE	MAE	RMSE
300m (1-way base case)	2.14	2.57	2.19	3.06
300m_2way	2.17	2.60	1.71	2.38

Table 2.8: MAE and RMSE (m/s) for wind speed comparing SODAR to 1-way vs. 2-way nesting for the locally-driven simple and complex terrain cases (STL and CTL) over a 48 hour period.

	Simple Terrain Case (STL)		Complex Terrain Case (CTL)	
Resolution	MAE	RMSE	MAE	RMSE
300m	2.24	2.74	1.85	2.64
900m	2.29	2.8	1.97	2.76
2700m	2.23	2.67	2.12	2.94
8100m	2.45	2.86	2.62	3.40

Table 2.9: Horizontal wind speed MAE and RMSE (m/s) for locally-driven events over simple and complex terrain (STL and CTL) compared to SODAR for a week-long period at hub height.

STL), the simulations still seem to under-predict turbulence intensity. The results for both cases show a higher frequency of low turbulence intensity than the observations indicate. Most of these values appear to correspond to the minimum turbulent kinetic energy (TKE) (0.1 m^2/s^2) set in the MYJ model. This agrees with Xie et al. (2013), who found that MYJ appears to under predict TKE when compared to observations and MYNN. These results suggest that there is room for improved turbulence closures for wind turbine siting purposes.

2.5   Conclusion

There is increasing demand to provide higher resolution, high precision, forecasts of winds for wind energy applications. Little guidance exists to aid numerical modelers as they push numerical weather prediction models to their limits. This chapter illustrates the sensitivity, or lack thereof, of the numerical results to various model configuration parameters. Case study simulation results were presented using WRF to capture both synoptically and locally-driven events at two different sites where terrain complexity varies greatly to develop preliminary insight into the ability to capture shifts in wind speed that are important to wind farm operators.

The effects of grid resolution, 1-way vs. 2-way nesting, turbulence closure models, and week-long simulation results were examined in this chapter. Large changes in wind speed were reasonably represented with all grid resolutions and grid nesting configurations tested for the simple terrain simulations (Cases STL and STS). These results are counter-intuitive when considering general recommendations to use higher resolution. Given the simple terrain of this wind farm it may be concluded that resolution does not necessarily bestow the benefit of increased accuracy. There was improvement with higher resolution and 2-way nesting when simulating a locally-forced event over complex terrain. Terrain as complex as at the complex terrain site discussed in this chapter warrants higher resolution simulations to predict winds, especially during weak forcing. During strong synoptic forcing, the complex terrain site showed minimal sensitivity to grid resolution, indicating that the forcing greatly dominates over local topographic influences. This suggests that computational resources may be spared by wind farm operators and forecasters if the site consists of simple terrain or even in certain cases with synoptic forcing over complex terrain. Simulations at high resolution could be most important in complex terrain and under local forcing.

It is of interest to note that the synoptically-driven events were better simulated (compared to observation data) than the locally-driven events for both wind farms; this is expected because the strong synoptic forcing in most cases overshadows other parameters. Land-surface parameters had more of an effect on the simulation results than resolution or the options used for turbulence closure during the locally-forced events, as demonstrated here by varying soil moisture conditions. Initialization conditions could be responsible for errors in the simulation results in some cases. It is difficult to recommend one PBL scheme that works best for every situation. The choice of a PBL scheme for a certain case may vary significantly depending on the meteorological forcing and terrain. On average, the prognostic

TKE equation schemes gave more accurate results when compared to observations (particularly GBM, UW, and MYJ). The non-local vertical eddy viscosity schemes (YSU and MRF) performed worse on average, most likely due to their weakness during strongly stable situations, but YSU might be acceptable in some cases in which computational resources are limited. Week-long simulations showed similar results to the short-term simulations. The MYJ turbulence closure seemed to consistently under-predict turbulent kinetic energy in both cases.
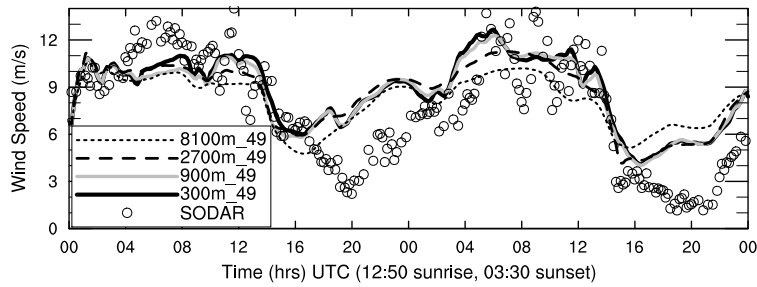
(a) Case STL
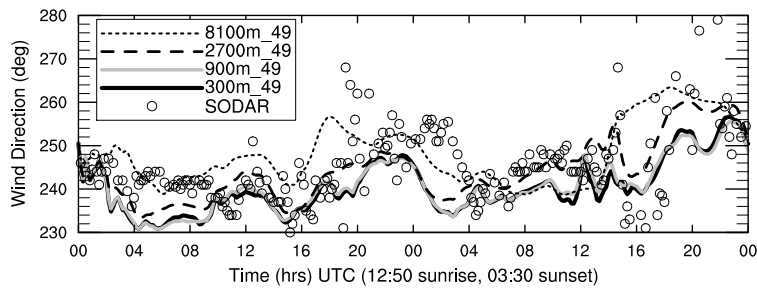
(b) Case STL
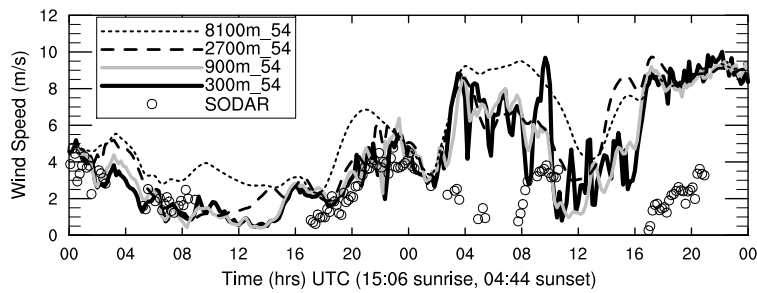
(c) Case CTL
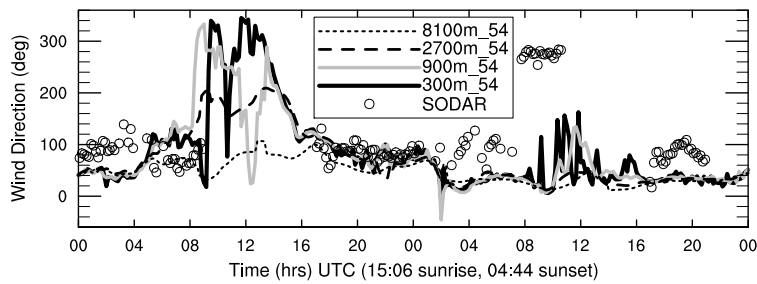
(d) Case CTL

Figure 2.3: Horizontal wind speed and direction 48 hour time series for locally-forced simple and complex terrain simulations at different horizontal resolutions at 80 m hub height compared to SODAR.
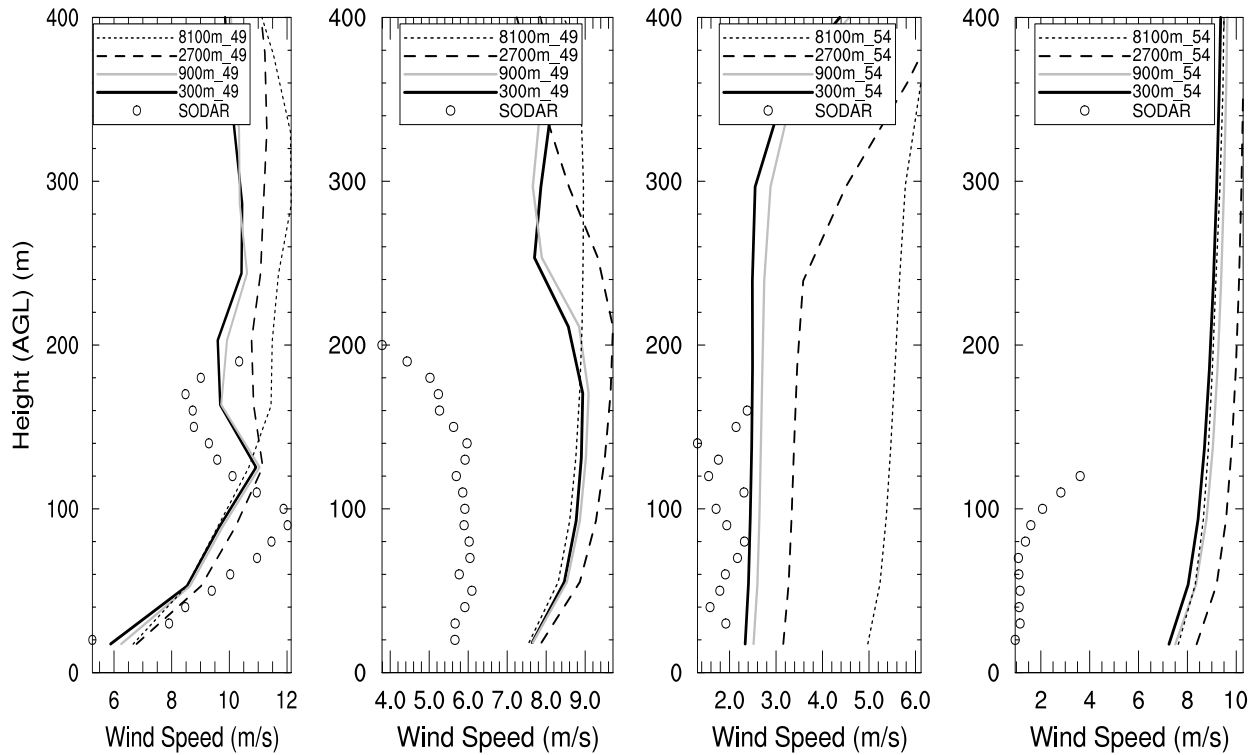
(a) Case STL at 5 UTC on first day.

(b) Case STL at 22 UTC on first day.

(c) Case CTL at 19.4 UTC on first day.

(d) Case CTL at 22 UTC on second day.

Figure 2.4: Vertical profiles of horizontal wind speed for locally-forced simple and complex terrain simulations at different horizontal resolutions compared to SODAR at single time slices.
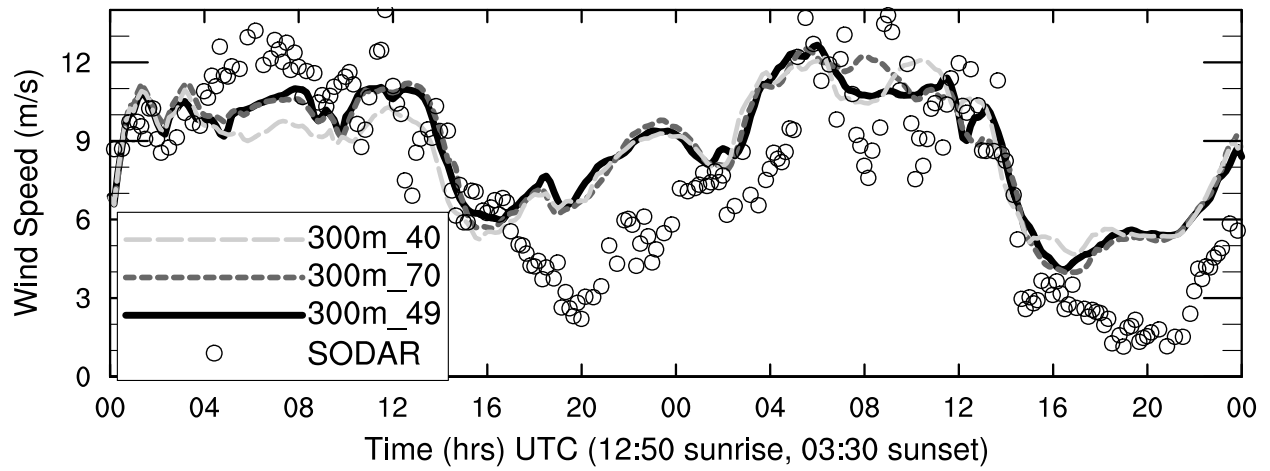
(a) Case STL
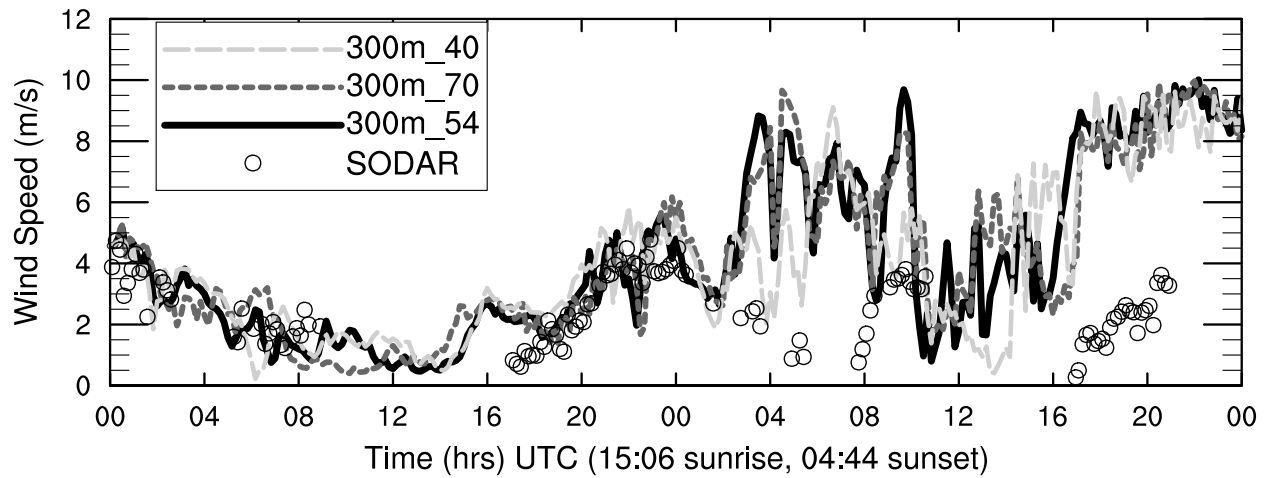
(b) Case CTL

Figure 2.5: Horizontal wind speed 48 hour time series for different vertical resolutions for the locally-driven complex and simple terrain cases at 80 m hub height compared to SODAR.
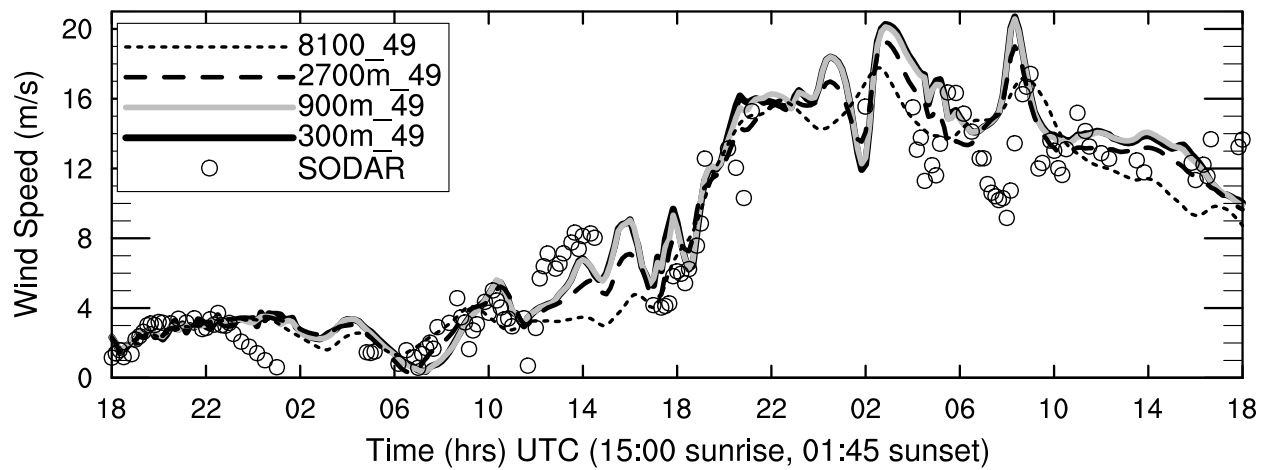
(a) Case STS
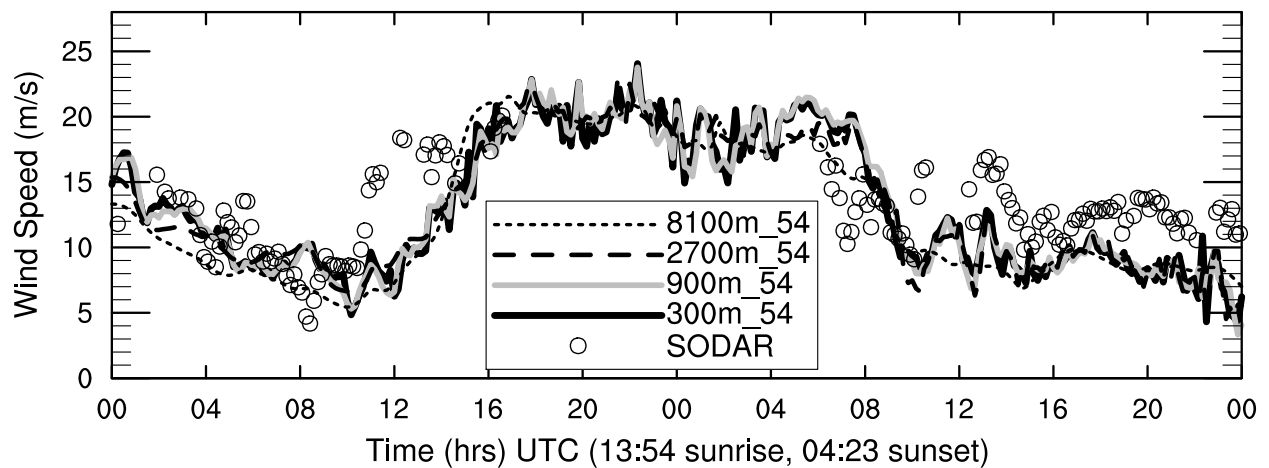
(b) Case CTS

Figure 2.6: Horizontal wind speed over a 48 hour time series for synoptically-forced simulations over simple and complex terrain (STS and CTS) at different horizontal resolutions compared to SODAR at 80 m hub height.
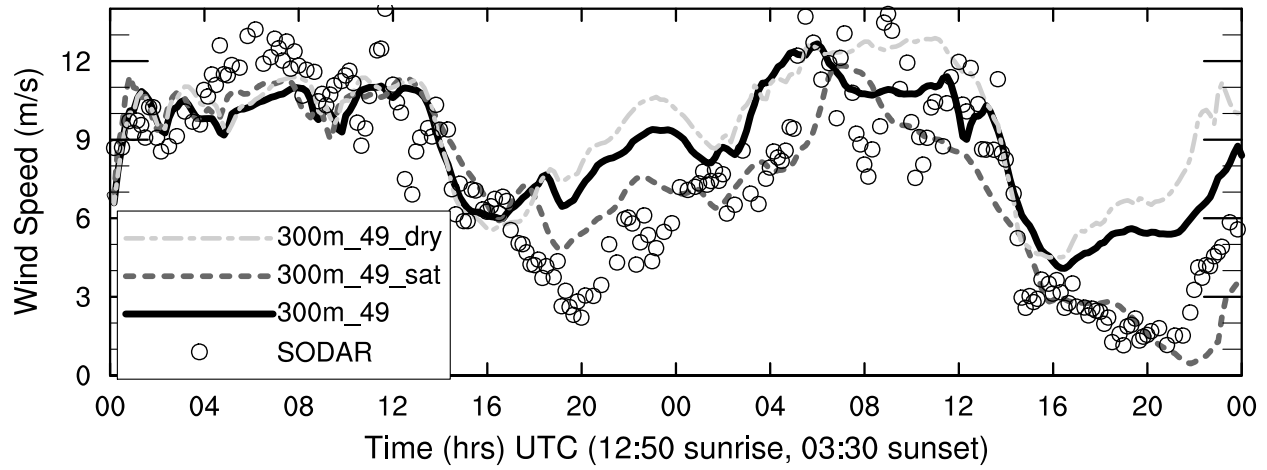
(a) Case STL
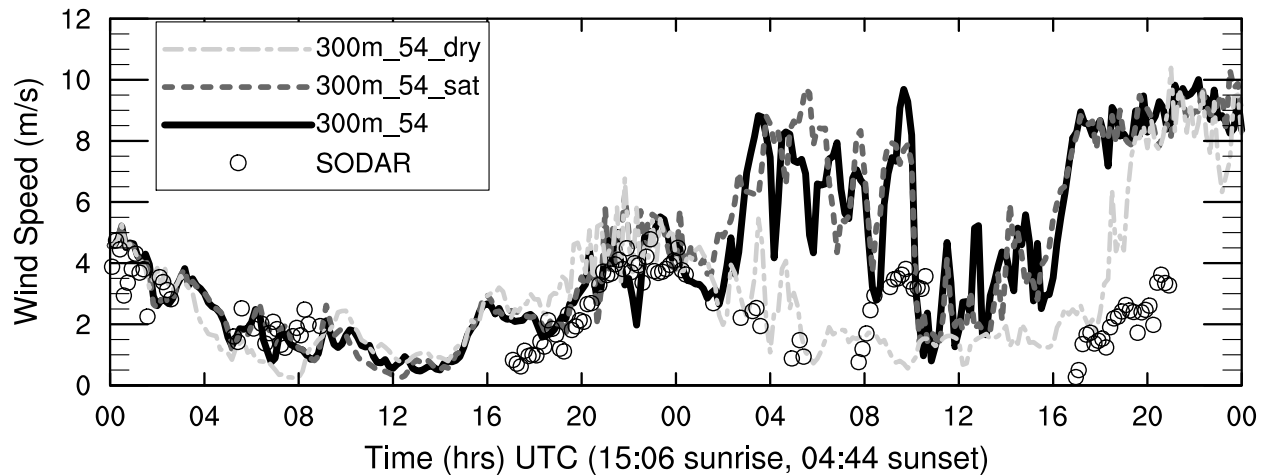
(b) Case CTL

Figure 2.7: Horizontal wind speed for saturated and dry soil moisture initializations compared to the base case and SODAR for a 48 hour locally-driven time period over both simple and complex terrain (STL and CTL) at 80 m above ground.
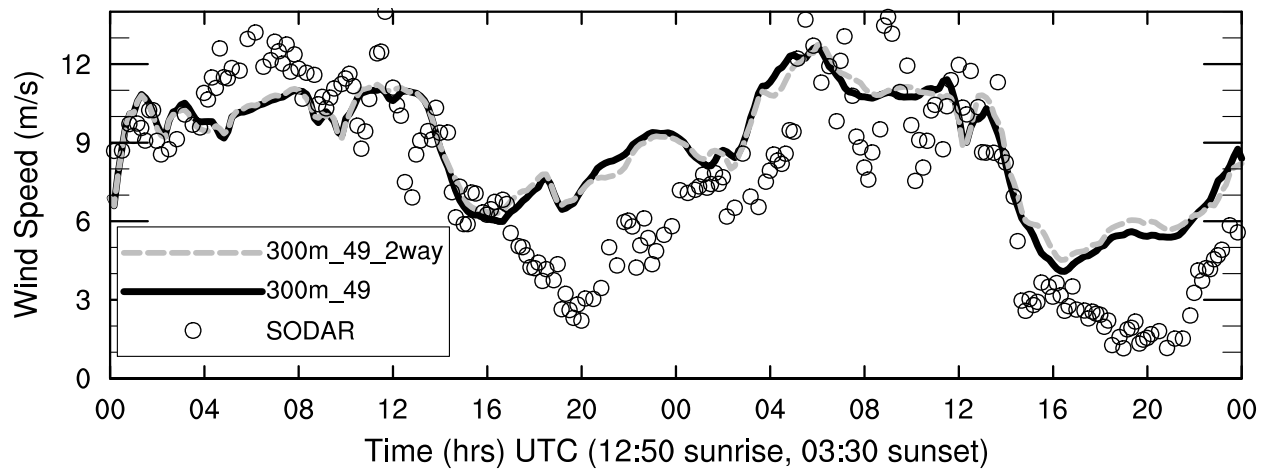
(a) Case STL
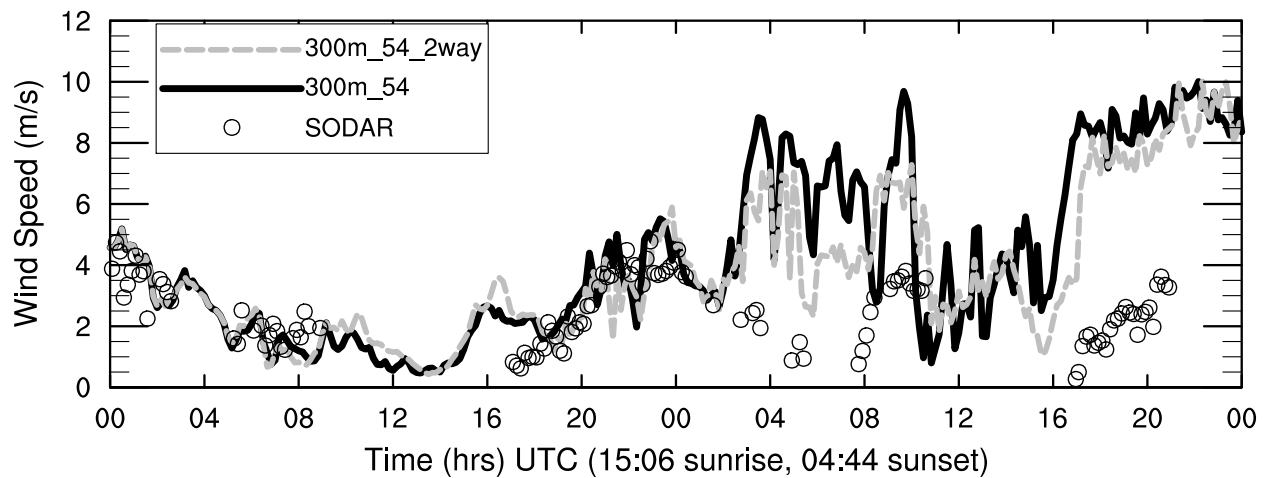
(b) Case CTL

Figure 2.8: Horizontal wind speed 48 hour time series comparing SODAR observations to 1-way (base case) and 2-way nesting for the locally-driven simple and complex terrain sites (STL and CTL) at 80 m hub height.
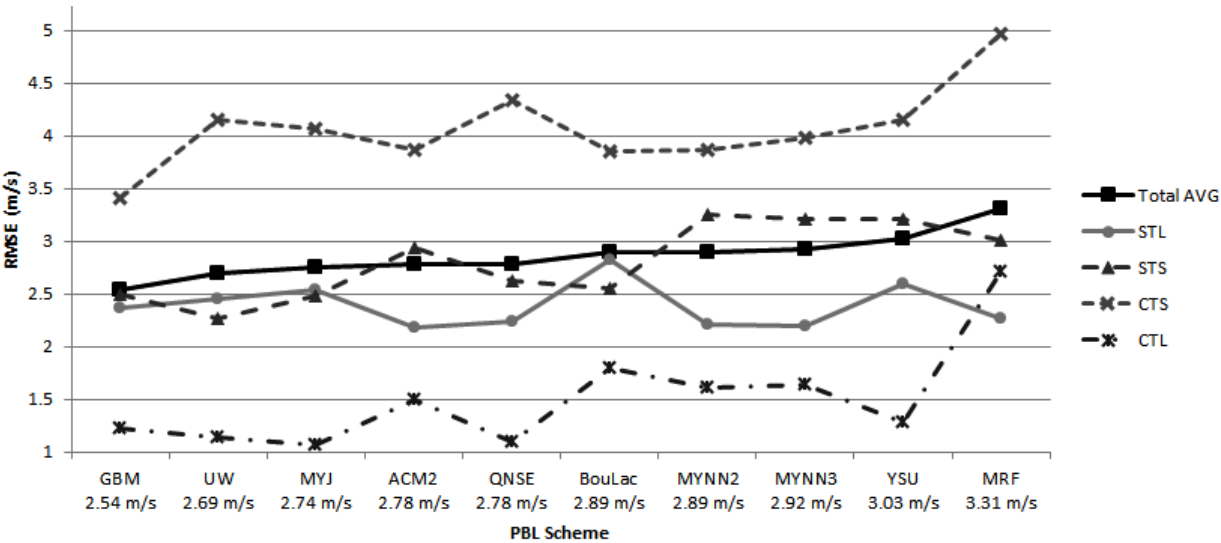
Figure 2.9: Horizontal wind speed RMSE (m/s) comparing 300 m horizontal resolution simulation results for different WRF PBL schemes against SODAR observations for each individual case (STL, STS, CTS, CTL) and a time based average for all the cases (Total AVG). PBL schemes are arranged from lowest average RMSE on the left to highest average RMSE on the right.
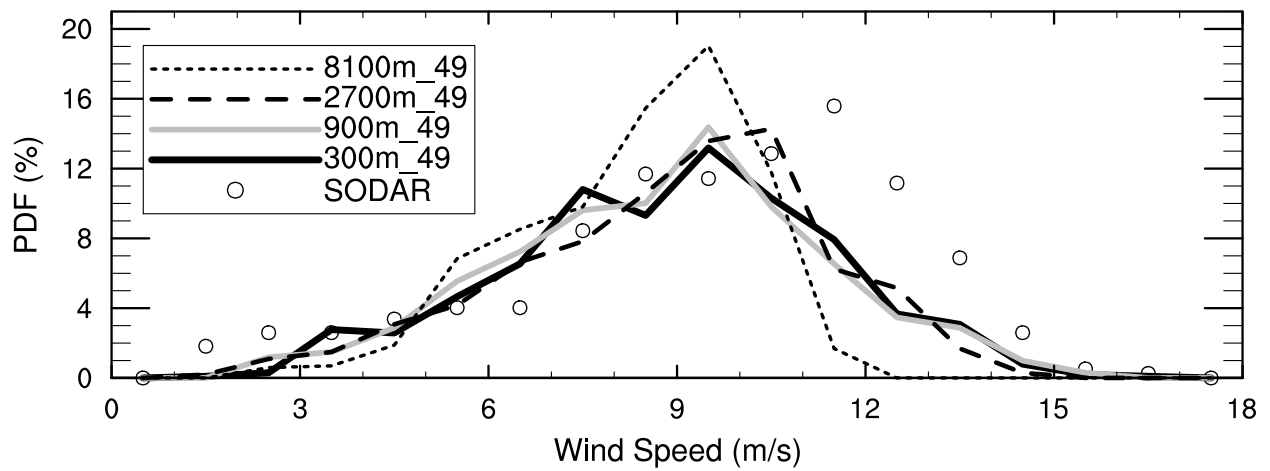
(a) Case STL
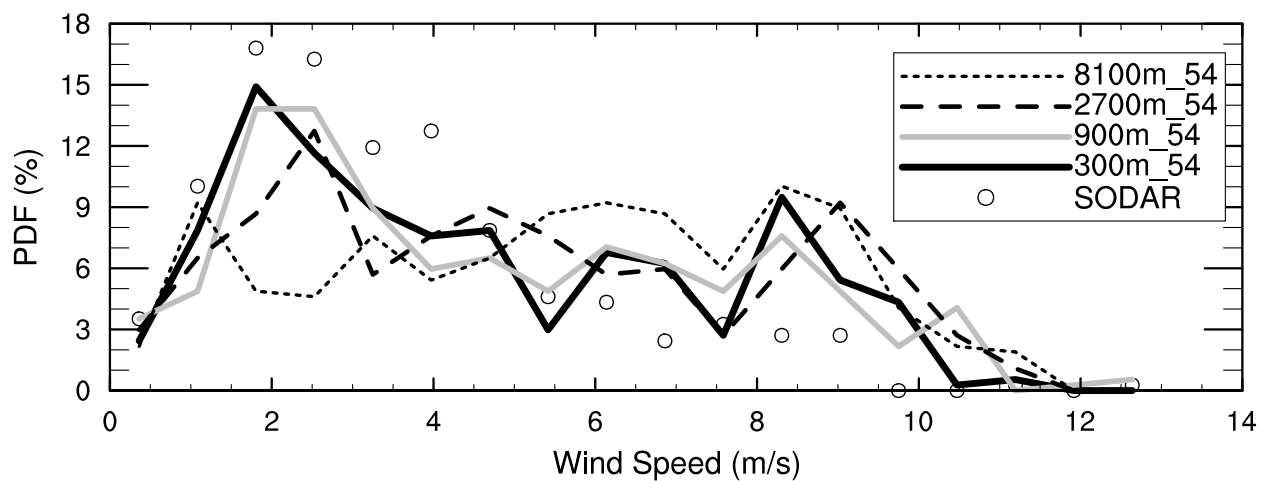
(b) Case CTL

Figure 2.10: Horizontal wind speed PDF for locally-forced week-long simulations comparing different horizontal resolutions over simple and complex terrain (STL and CTL) to SODAR at hub height.
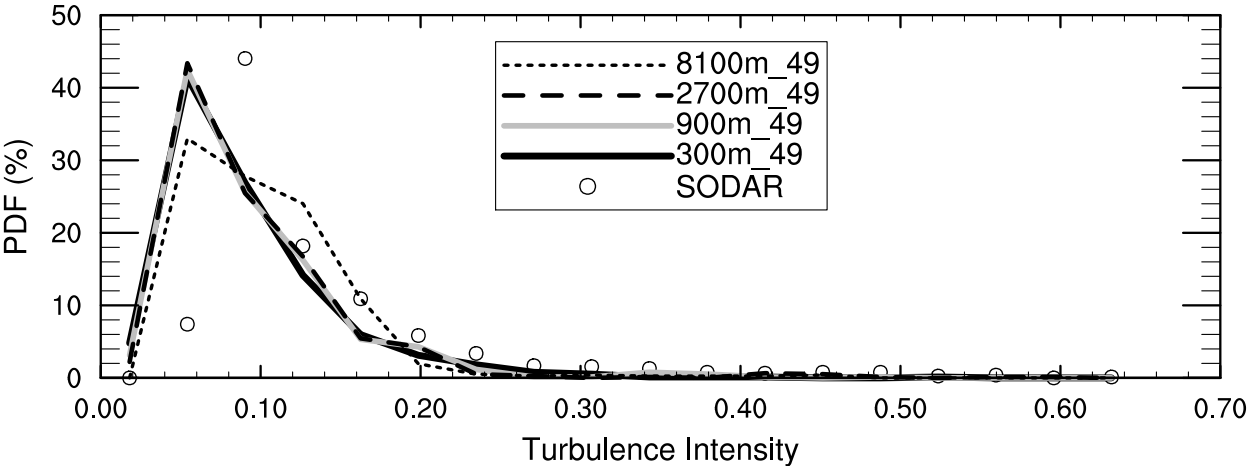
(a) Case STL
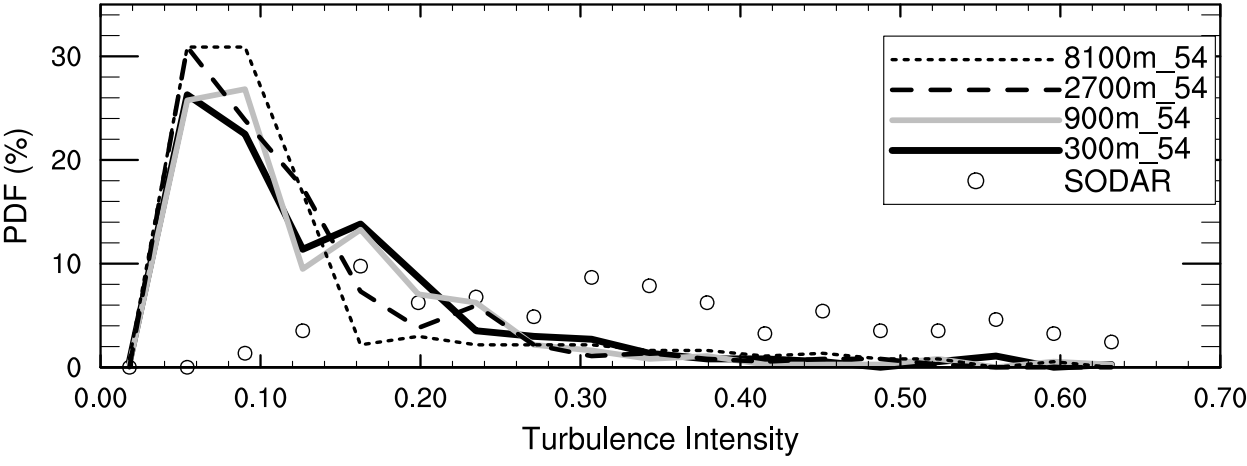
(b) Case CTL

Figure 2.11: Turbulence intensity PDF for locally-forced week-long simulations comparing different horizontal resolutions over simple and complex terrain (STL and CTL) to SODAR at hub height.

Chapter 3

Implementation of a GAL Parameterization

3.1 Abstract

A generalized actuator line (GAL) wind turbine parameterization is implemented within the Weather Research and Forecasting (WRF) model to enable high-fidelity large-eddy simulations of wind turbine interactions with boundary layer flows under realistic atmospheric forcing conditions. Numerical simulations using the GAL parameterization are evaluated against both a generalized actuator disk (GAD) wind turbine parameterization already implemented into the WRF model as well as against measurements from two field campaigns, the Turbine Wake and Inflow Characterization Study and the Crop Wind Energy Experiment, each of which measured the inflow and near-wake regions of a single turbine. The two datasets permit validation under weakly convective and weakly stable conditions. The GAD and GAL parameterizations produce similar aggregated wake characteristics in simulations of both stability classes, verifying the correct implementation of the GAL parameterization into WRF. The applicability of each approach to the representation of wake wind speed, variance and vorticity distributions is examined by comparing fine-resolution GAL and GAD simulations, as well as GAD simulations at both fine and coarse-resolutions. The higher-resolution GAD and GAL simulations show slightly larger and more persistent velocity deficits in the wake, and substantially increased variance and vorticity when compared to the coarse-resolution GAD. The GAL generates distinct tip and root vortices that maintain coherence as helical tubes for approximately one rotor diameter downstream, whereas the GAD produces rings of vorticity surrounding the rotor and hub. While vorticity distributions differ in the near wake region, those differences become nearly indistinguishable at distances greater than approximately 2 rotor diameters downstream. Providing both GAD and GAL parameterizations within the WRF model supports a range of applications. Coarse-resolution simulations using the GAD produce similar aggregated wake characteristics to both fine-scale GAD and GAL simulations, at a fraction of the computational cost.

The GAL parameterization provides a capability to resolve near wake physics, including vorticity shedding and wake expansion, for applications requiring the increased fidelity.

3.2 Introduction

Wind turbine wakes, via reduced wind speeds and increased turbulence, play an important role in power production and fatigue loading of downstream turbines (Högström et al., 1988; Magnusson and Smedman, 1999). Power losses of greater than 40% have been observed in downstream turbines (Barthelmie et al., 2010) as a result of upwind wakes. Moreover, increases of turbulence intensities of greater than 50% above background values have been measured at distances of 10 rotor diameters downstream of large turbines (Elliott and Barnard, 1990). Several numerical simulations (e.g Churchfield et al. (2012) and Meyers and Meneveau (2012)), and experimental studies (Aitken et al., 2014a; Hirth et al., 2012; Smalikho et al., 2013) have demonstrated that wind turbine wakes commonly persist for large distances downstream, often beyond 10 rotor diameters, distances far greater than typical turbine spacings within wind farms. While reduced velocities in turbine wakes reduce power output, the increased turbulence levels increase strain on downstream turbine's mechanical components, leading to increased downtime, maintenance, and a shorter life span (Churchfield et al., 2012; Kelley et al., 2005; Shaw et al., 2009; Thomsen and Sorensen, 1999). Consequently, the ability to accurately model the effects of wind turbine wakes is critical to improving wind turbine design, performance, and reliability.

Wake characteristics impacting both downstream power production and fatigue loading are strongly influenced by atmospheric processes (Kelley et al., 2005; Vanderwende and Lundquist, 2012; Wharton and Lundquist, 2012a; Wharton and Lundquist, 2012b). Most engineering computational fluid dynamics (CFD) tools used to estimate these parameters are not able to represent these atmospheric drivers of wake variability (Mehta et al., 2014; Sanderse et al., 2011). Many engineering wake models are based on the assumption that the vertical profiles of velocity deficit and turbulence intensity are roughly Gaussian, axisymmetric, and self-similar in the far wake (Mehta et al., 2014). Multiple studies have shown that these assumptions are not always valid (Barthelmie et al., 2001; Gomez-Elvira et al., 2005). Further, many such models represent turbulence using the Reynolds-Averaged Navier-Stokes (RANS) equations, which may not adequately capture transients in turbulence dynamics. Engineering CFD models are computationally inexpensive, quick, and can provide acceptable predictions of wind power production in many applications, but they provide limited insight into the physics of wind farm aerodynamics (Mehta et al., 2014) required to address contemporary challenges in wind plant design and optimization.

Even the highest-fidelity engineering tools lack the necessary atmospheric physical process parameterizations and boundary conditions to simulate complex atmospheric flows influenced by realistic variability in environmental forcing. Environmental drivers such as weather events, terrain and other surface characteristics can strongly modulate both atmospheric boundary layer (ABL) structure and the turbulence field, and subsequently wake formation

and evolution processes.

In contrast, mesoscale weather prediction models can be utilized to provide information influencing atmospheric flow variability not captured in current wind farm CFD tools. These include both realistic initial and boundary conditions, and representation of important physical processes required to improve the realism of atmospheric flows at wind farm sites influenced by diverse weather phenomena and surface and terrain characteristics.

As such, incorporating mesoscale input into microscale wind farm CFD simulations, which resolve atmospheric turbulence and turbine/airflow interactions explicitly, is an active area of research. One approach is to couple a mesoscale with an off-line CFD model (Churchfield et al., 2013; Gopalan et al., 2014; Zajaczkowski et al., 2011). An alternative approach is to use a unified model that can couple mesoscale simulations with microscale wind farm simulations internally. The Weather Research and Forecasting (WRF) (Skamarock et al., 2008) model is a promising framework within which to develop mesoscale-microscale coupled wind farm simulation capabilities, due to its support of both mesoscale and microscale simulation, a wide user base, and an active development community that has contributed several improved capabilities of relevance to wind energy research needs, including wind farm parameterizations appropriate for both mesoscale (e.g. Fitch et al. (2012)) and microscale (e.g. Mirocha et al. (2014)) simulation.

The WRF model achieves coupling between mesoscale and microscale wind farm simulation via grid nesting, which permits a subset of a computational domain(s) to be resolved at higher resolution, with lateral boundary conditions for the nested domain(s) obtained from the bounding domain(s). Downscaling via grid nesting can be pursued to sufficiently fine resolutions to support large-eddy simulations (LES) on the microscale domains(s). By explicitly resolving the energetically important scales of atmospheric turbulence, including important transients impacting turbulence dynamics, LES provides a high-fidelity simulation framework for wind turbine and wind farm simulations in turbulent flows. The ability to incorporate mesoscale weather and environmental drivers into turbulence resolving LES provides a promising framework to study the physics of wind farm aerodynamics and wake evolution in realistic operating environments. WRF allows canonical idealized LES, but also offers an ability to incorporate elements of contemporary mesoscale simulations, including atmospheric radiation, cloud processes, surface physics, data assimilation, and ensemble techniques, among others (Mirocha et al., 2014).

To enable wind farm simulations in nested LES within WRF, wind turbine parameterizations at the appropriate level of fidelity must also be implemented. An actuator disk parameterization is one approach to simulate turbine-airflow interactions and wake formation that is gaining popularity. The actuator disk represents the turbine as a two-dimensional disk formed by the rotation of its blades. Forces on both the disk and the atmosphere are computed by combining analysis of momentum balance in rotating, annular rings intersecting the disk, with lift and drag forces computed along isolated, two-dimensional blade elements, using two-dimensional aerodynamic theory. The actuator disk parameterization is most applicable for simulating the far wake (greater than 2 to 4 rotor diameters (D) downstream), due to its inability to represent near-wake physics, including the small-scale wake vortic-

ity features emanating from individual blades and other turbine components (Pijl, 2007). Mirocha et al. (2014) and Mirocha et al. (2015) and Aitken et al. (2014b) showed that a generalized actuator disk (GAD) parameterization implemented into WRF produced wakes with physically consistent rotation and velocity deficits that compared well with measurements at distances of 2 to 6D.

Suitable simulation of the near wake, occupying the first 2 to 4D downstream (Vermeer et al., 2003), requires a higher fidelity parameterization than an actuator disk, one that is capable of representing small-scale vorticity production from the blades' tips and roots (and other turbine components). The tip vortices are particularly important due to their role in mixing low momentum air in the wake with higher momentum background flow (Mehta et al., 2014). Thin layers of strong shear created at the blades' tips expanding into the wake with downstream distance, interact with instabilities within the tip vortices (Sørensen, 2011) causing those structures to break down. The break down and merging of the tip vortices with the background shear signifies the transition into the far wake (Mehta et al., 2014). This transition contains the greatest turbulence intensities and velocity deficits (generally between 2 to 6D downstream) (Wu and Porté-Agel, 2012).

To more realistically capture near-wake physics, a generalized actuator line (GAL) parameterization is implemented into WRF, building upon the GAD parameterization implemented previously by Mirocha et al. (2014). Unlike the GAD, which applies aerodynamic forces averaged over annular elements within the disk to represent the impacts of the blades within, the GAL applies aerodynamic forces along each of the turbine blades as they primarily rotate within the disk. While vorticity in the GAD parameterization is shed into the wake as a continuous sheet surrounding the disk, the GAL parameterization produces distinct tip and coherent periodic helicoidal vortices within the near-wake region (Ivanell et al., 2009; Lundquist et al., 2015; Sorensen and Shen, 2002; Troldborg et al., 2007), allowing the GAL parameterization to capture higher fidelity characteristics of the near wake.

Previous studies that have compared GAD with GAL parameterizations for idealized uniform inflow (Martınez et al., 2012; Troldborg et al., 2010), and to wind tunnel measurements (Porte-Agel et al., 2011) have shown GAL parameterizations perform better in the near wake, while both perform comparably in the far wake region. Herein, a GAL parameterization is implemented into the WRF model (see appendix section 3.7 for details of the implementation) in a step towards utilizing actuator parameterizations of varying levels of fidelity in increasingly realistic ABL flows. We verify the implementation of the GAL parameterization into WRF in idealized LES setups similar to Mirocha et al. (2014) and Mirocha et al. (2015) by comparing the GAL against the validated GAD parameterization. Working toward a capability for general atmospheric conditions, we investigate each approach under varying atmospheric stability conditions; simulations are performed for two different field sites, including observations for weakly convective and stable conditions.

3.3   Case studies and measurements

Two observational data-sets are used to evaluate the GAL against the GAD parameterization in WRF, the Turbine Wake and Inflow Characterization Study (TWICS), which represents weakly convective conditions, and the Crop Wind Energy Experiment of 2011 (CWEX-11), which provides observations during stable conditions.

TWICS measured the inflow to and wake from a 2.3-MW wind turbine located at the National Renewable Energy Laboratory's National Wind Technology Center (NWTC) near Boulder, CO. The turbine has a hub height of H = 80 m and rotor diameter of D = 101 m.

We simulate the afternoon of 22 April, 2011 between 13:00 and 17:00 following Mirocha et al. (2014), which featured nearly steady wind speeds and direction, and was characterized by weak to moderate convective instability. Herein we duplicate the weakly convective simulation (from Mirocha et al. (2014)), for which simulated wake properties showed good agreement with the observations, and also examine the performance of the GAL parameterization under canonical neutral conditions. The forcing conditions for the WRF GAD and GAL simulations were specified using data from both meteorological tower and profiling lidar system (WindCUBE version 1) observations located upstream from the turbine. Wake characteristics were evaluated using plan-position indicator (PPI) scans from the National Oceanic and Atmospheric Administration's High-Resolution Doppler Lidar (HRDL) research-grade scanning lidar system (Mirocha et al., 2014). See Figure 3 from Aitken et al. (2014a) for a map of the site.

Data from the CWEX-11 experiment were utilized for stably stratified conditions. CWEX-11 took place within a 300 MW wind farm in Central Iowa, and utilized two vertical profiling lidars, positioned at 2.2D to the south (L1) and 3.5D to the north (L2) of a GE 1.5SLE wind turbine, with H = 80 m and D = 77 m (Rajewski et al., 2013). Rhodes and Lundquist (2013) (Rhodes and Lundquist, 2013) described CWEX-11 lidar performance and show a map of the lidar locations relative to the turbine in their Figure 1. Profiles of wind speed, wind direction, and lidar derived variance of velocity (a proxy for turbulence) were utilized by Mirocha et al. (2015) to examine the impacts of the turbine on the flow and to force and evaluate their GAD simulations. The lidars provided two-minute averages (from 1-Hz instantaneous measurements) of horizontal wind speed, direction, and variance of each velocity component at ten measurement heights from 40 to 220 m above ground level at 20 m intervals. Additional instrumentation at CWEX-11 provided surface energy budget and other surface and flow parameters within the lowest 10 m of the atmosphere (Rajewski et al., 2014, 2013).

Data from the 48-hour stable period occurring July 17, 04:30-08:30 UTC, investigated in Mirocha et al. (2015) are utilized herein to evaluate the GAD and GAL parameterizations during CWEX-11 stable conditions. This time period includes relatively uniform vertical gradients of both upstream wind speed and direction (from L1 lidar) across the measurement heights. It is also characterized by variability about relatively constant mean values of those parameters, as shown in Figure 5 from Mirocha et al. (2015).

3.4   Simulation setup

We utilize a fine LES domain nested one-way within a bounding LES domain following Mirocha et al. (2014) and Mirocha et al. (2015). Periodic lateral boundary conditions are utilized on the coarse domain, allowing a turbulent, steady-state ABL to develop. The coarse-domain solution provides turbulent ABL inflow (and outflow) for the fine LES nested within. The coarser LES is run for several hours to develop turbulent flow consistent with the specified surface forcing and geostrophic wind. The actuator parameterizations are used only on the nested LES domains.

For each case study, three simulations are performed: coarse LES with the GAD, fine LES with the GAD, and fine LES with the GAL. While finer resolution is required for the GAL to resolve individual blade motion, GAD simulations are also performed using the same resolution as the GAL to compare the effects of the different parameterizations, relative to the influence of model resolution. The domain sizes were chosen to be large enough to allow for both the equilibration of LES to the finer resolution on the nested domain before encountering the turbine ($\approx$200 grid points), and to provide ample space for the wakes to develop downstream ($\approx$11D). Identical simulations using no wind turbine parameterizations are also executed for each case study and resolution to assist the examination and quantification of turbine impacts and wake characteristics.

Each case is identified (see table 3.1) with an abbreviation which indicates the stability class (CON for weakly convective, NEU for neutral, or STA for weakly stable), turbine parameterization (GAD or GAL), and grid resolution (F for fine and C for coarse) used for the simulation. CON-GAD-F is, for example, the name for the weakly convective case with the GAD parameterization at fine resolution, while STA-GAL-C would denote stable, GAL simulations with coarse resolution. A list of domain dimensions and parameter values is also provided in table 3.1.

The (TWICS) weakly convective (CON) and neutral (NEU) cases are forced with surface heat fluxes of 20 and 0 W m^{-2} respectively. Neutral conditions are included both to verify the GAL implementation in canonical neutral LES, and to evaluate the response of the GAL to small changes of stability. For the TWICS simulations, the coarse GAD simulations (CON-GAD-C and NEU-GAD-C) use horizontal resolutions of $\Delta x = \Delta y = 30$ m (outer domain) and 10 m (nested domain), while the GAD-F and GAL-F simulations (CON and NEU) each use $\Delta x = \Delta y = 6$ m and 2 m.

The coarse GAD simulation of the stable CWEX-11 case (STA-GAD-C) utilizes horizontal resolutions of $\Delta x = \Delta y = 18$ m and 6 m on the outer and nested domains, respectively. These resolutions are used to account for the smaller diameter wind turbines at CWEX-11 when compared to TWICS and the need to use higher resolution to capture the smaller turbulence structures that occur during stable conditions. Fine resolution GAD and GAL CWEX-11 simulations (STA-GAD-F and STA-GAL-F) use the same resolutions as the fine resolution TWICS (CON and NEU) simulations. The turbine locations within the nested domains are provided in Table 3.1.

Each simulation uses Δz values on both domains approximately equal to Δx on the

nested domain. Values of Δz are constant within the lowest 200 m of the boundary layer, and increase by 5% per grid index above 200 m. As WRF uses a pressure-based vertical coordinate system, precise specification of Δz values is not possible, however departures are small and do not appreciably influence the results. The vertical pressure levels are specified using the hypsometric equation, with a surface pressure of 1×10^5 Pa and atmospheric temperatures from the standard atmosphere. Domain depths are provided in Table 3.1. A Rayleigh damping layer with a coefficient of 0.003 s^{-1} is applied to the upper 700 m and 1 km of each domain for TWICS and CWEX-11, respectively. A zero vertical velocity and zero stress boundary condition are applied at the model top. The default fifth and third-order horizontal and vertical advection schemes, respectively, are used.

Turbulence is represented using the Smagorinsky LES closure (Lilly, 1967; Smagorinsky, 1963) for the subgrid-scale (SGS) stresses and fluxes during the TWICS simulations following Mirocha et al. (2014), while the CWEX-11 case utilized the nonlinear backscatter and anisotropy (NBA) model (Kosovic, 1997; Kosovic and Curry, 2000), to better simulate the SGS stresses during stable conditions following Mirocha et al. (2015) (see Appendix section 3.7 for details on SGS models). The surface boundary conditions use Monin-Obukhov similarity theory (Monin and Obukhov, 1954). The TWICS simulations are forced using specified heat flux values, while CWEX-11 utilizes a surface cooling rate to better capture stable boundary layer dynamics (Basu et al., 2008). TWICS and CWEX simulations use a roughness length of 0.1 m and 0.2 m respectively, reflecting the divergent land cover at the two sites, with tall grass and isolated brush at TWICS, and a tall corn canopy at CWEX-11.

The computational setup is simplified by orienting the geostrophic wind vector such that the flow is approximately parallel to the x-axis, permitting the placement of the GAD/GAL within the y-z plane to be nearly perpendicular to the inflow. The yaw angle is held fixed during the simulations. For the same geostrophic wind vector, changes to either the spatial resolution or surface forcing conditions will influence the wind speed and direction within the ABL, due to different resolved turbulence structures and vertical gradients (Brasseur and Wei, 2010). To account for this sensitivity, slightly different geostrophic forcing values, shown in Table 3.2, are used in order to provide similar inflow wind speed and direction values at the location of the actuators for all of the simulations.

All the simulations are initialized dry, and no radiation, cloud, or land surface models are used. The simulations are initialized with uniform potential temperature profiles of 300 K below 500 m, increasing by 10 K per km above, providing a capping inversion to damp turbulence at the ABL top. To initiate turbulence, small perturbations of ± 0.5 K, obtained from a pseudo-random uniform distribution, are added to the initial values of potential temperature below 500 m, as a decreasing cubic function of height (Mirocha et al., 2014).

Forcing idealized LES with geostrophic wind speed and direction results in inertial oscillations which alter boundary layer characteristics over the first several hours of a simulation. For the TWICS cases (CON and NEU), a spinup LES is run for 15 hours with the surface heat flux specified (20 and 0 W m^{-2} for weakly convective and neutral, respectively) to allow the solution to come into balance with the geostrophic wind vector. Thereafter, the nested domain with the GAL or GAD parameterization is introduced, and instantaneous velocity

fields output every 10 seconds from hour 16 to 18 are examined.

For the CWEX-11 cases (STA), a spinup LES is run for 15 hours with neutral forcing at the surface. At hour 15, the surface temperature is uniformly prescribed as the horizontal average temperature at the first model gridpoint above the surface, providing neutrality in the aggregate, after which a constant cooling rate of $-\frac{2}{3}$ K hr^{-1} is applied, resulting in stable stratification of the flow. Thereafter, instantaneous velocity fields are output each second for 40 minutes.

Upon introduction of surface cooling, the subsequent stabilization of the simulated flows results in changes of the flow direction over the ensuing several hours, as observed in Mirocha et al. (2015). The higher-resolution GAL and GAD simulations conducted herein, however, feature much slower rotation of the wind direction. The much slower change of wind direction within the finer resolution simulations (STA-GAD-F and STA-GAL-F) is due to the higher resolution capturing more energetic resolved turbulence structures, which maintain vertical exchanges of momentum within the lower ABL. The coarser resolution simulations (STA-GAD-C) are unable to maintain robust resolved turbulence, resulting in laminarization, and a much more rapid change of wind direction.

Estimation of simulated wake effects and comparison with observations requires alignment of the flow with the actuator and the upstream and downstream sampling locations. For the coarse simulation (STA-GAD-C), alignment of the flow with the instrumentation was achieved after 5 hours and 20 minutes of surface cooling, with output sampled from 22:20 to 23:00. Beyond 23:00, the wind direction no longer aligned with the instrumentation. Due to more robust resolved turbulence, the fine simulations (STA-GAD-F and STA-GAL-F) required an additional 13 hours of simulation for the wind direction to rotate into alignment with the instrumentation. Simulation output was collected from hour 33:00 to 33:40, matching the wind profiles for the same length of time as the coarse simulation. The nested domains with the actuator parameterizations are introduced 20 minutes prior to the analysis period to provide for spinup of the flows within the nested domains.

3.5 Results

Characteristics of turbine wakes and how they vary in response to actuator parameterization type, simulation resolution, and atmospheric stability are compared and evaluated against observations. These characteristics include velocity, variance, and vorticity distributions.

Velocity Comparison

While all simulations exhibit a velocity deficit in the wake, the wide range of velocity deficits suggest that the simulation method and resolution impact the velocity deficit. Figure 3.1 shows instantaneous horizontal wind speed at 80 m above the surface, a typical hub height for contemporary utility scale turbines, including those used in both TWICS and CWEX-11.

The GAD-C (Figures 3.1a to 3.1c), GAD-F (Figures 3.1d to 3.1f), and GAL-F (Figures 3.1g to 3.1i) simulations under CON (Figures 3.1a, 3.1d, 3.1g), NEU (Figures 3.1b, 3.1e, 3.1h), and STA (Figures 3.1c, 3.1f, 3.1i) forcing conditions are shown. The turbine wakes are clearly evident in each simulation, emanating downstream from the turbine parameterization at $x = y = 0$ in this and subsequent figures. Significant differences in spatial variability, both within the wakes and the ambient flow, are evident. These differences are due primarily to divergent turbulence characteristics resulting from the different forcing conditions. The greatest variability and largest turbulence structures occur within the weakly convective TWICS simulations (CON), and the smallest within the stable CWEX-11 simulations (STA).

The overall wake structures appear similar between the GAD-F (Figures 3.1d to 3.1f) and GAL-F (Figures 3.1g to 3.1i) simulations. Wake attenuation is slightly more rapid under CON than NEU conditions, due to stronger turbulence mixing of the wakes with the background flow (Zhang et al., 2013b). Wakes are more persistent during the stable simulations due to weaker background mixing. Due to the higher resolution simulations being able to resolve a broader range of scales of motion, within both the wakes and the background flows, differences between the simulations at different resolutions are evident. Differences between GAD and GAL simulations at the same resolution, however, are difficult to discern from examination of instantaneous velocity cross sections alone.

Differences between the wake characteristics can be better ascertained by averaging the flow field to reduce variability within the background due to random turbulence fluctuations. Figures 3.2 and 3.3 show averaged values of u (left), v (middle), and w (right) in the y-z plane (0.1D downstream from the turbine) for the CON and STA cases, respectively. Results from the NEU simulations are nearly indistinguishable from those of the CON conditions, due to the small differences in ABL flow characteristics, and thus are not shown henceforth. The distributions are slightly asymmetric, due to differences between the mean flow direction and the rotor plane, which was held fixed, velocity shear in the vertical (lower wind magnitudes closer to the surface), and the tilting of the rotor plane (details on tilting implementation in Appendix section 3.7) (Aitken et al., 2014b). Values of u primarily show the effects of turbine thrust, which results from a drag force opposite the inflow direction. The v and w components show both flow divergence around the GAD and GAL, and rotation due to torque forces within the rotor swept area.

Magnitudes of the u velocity component are smaller in the lower than the upper portions of the rotor disk for both parameterizations due mainly to wind shear, but also to tower and hub drag effects, which are better resolved by the fine resolution simulations. The turbine hub and tower are not readily discernible in the GAD-C parameterization due to the much smaller cross section of the hub and tower when compared to the grid spacing, resulting in small drag forces being applied to the grid-cell average velocity. As a result, the largest velocity deficits are observed in the lower portion of the turbine immediately behind the tower due to the additive effect of both tower and turbine drag (Figures 3.2d to 3.2i and 3.3d to 3.3i). Apart from differences due to resolution of the hub and tower, the averaged velocity distributions are similar in both magnitude and spatial distribution for each resolution, and for each parameterization.
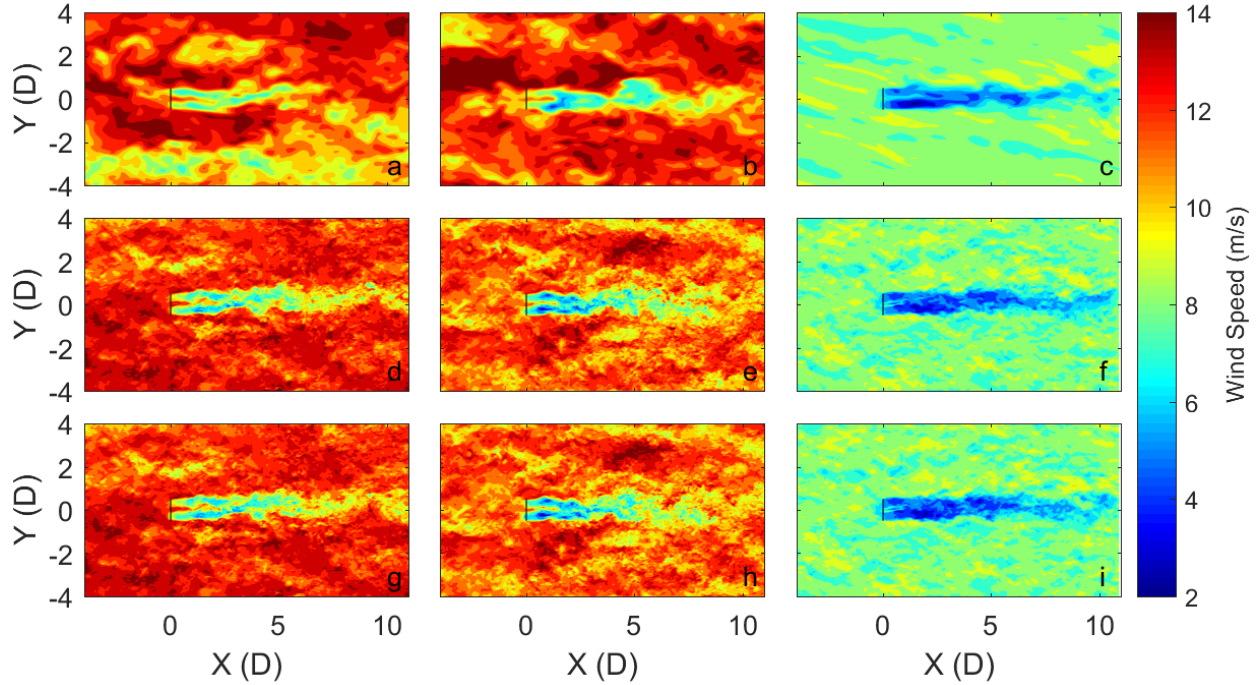
Figure 3.1: Instantaneous horizontal wind speed values at 80 m hub height for the CON (a, d, g), NEU (b, e, h), and STA (c, f, i) cases. The top row shows GAD-C (a, b, c), the middle row shows the GAD-F (d, e, f), and the last row shows the GAL-F (g, h, i) for each stability case. The CON and NEU cases are both at hour 17, while the STA case is at hour 22:40 for the coarse resolution (C) and hour 32:50 for the fine resolution (F) simulations. The black line indicates the location of the GAD or GAL parameterization.

Mean velocities in the turbine wakes show differences between the fine and coarse resolutions. Figures 3.4 and 3.5 show the evolution of mean u and w velocities with downstream distance in the x-y and x-z planes during both CON and STA conditions, respectively. Differences in resolution are clearly evident immediately downstream from the GAD and GAL, for which the fine resolution (F) is able to capture the additive impact of the blade and tower below the hub, as well as small regions of lower u velocity in the near wake. The finer resolution also captures slightly larger vertical velocity magnitudes immediately downstream (Figs. 3.4g to Figs. 3.4i and Figs. 3.5g to Figs. 3.5i). The vertical velocities indicate wake rotation that is opposite the clockwise rotation of the turbine (viewed from upstream).

Grid resolution is also observed to impact the rate of wake attenuation during the CON, but not the STA conditions (for reasons discussed in the following section), with the coarser resolution (C) accelerating wake attenuation. The different stability conditions strongly impact the rates of wake attenuation in both the streamwise and spanwise directions. This is due to the larger eddies more efficiently mixing wake momentum with the background flow
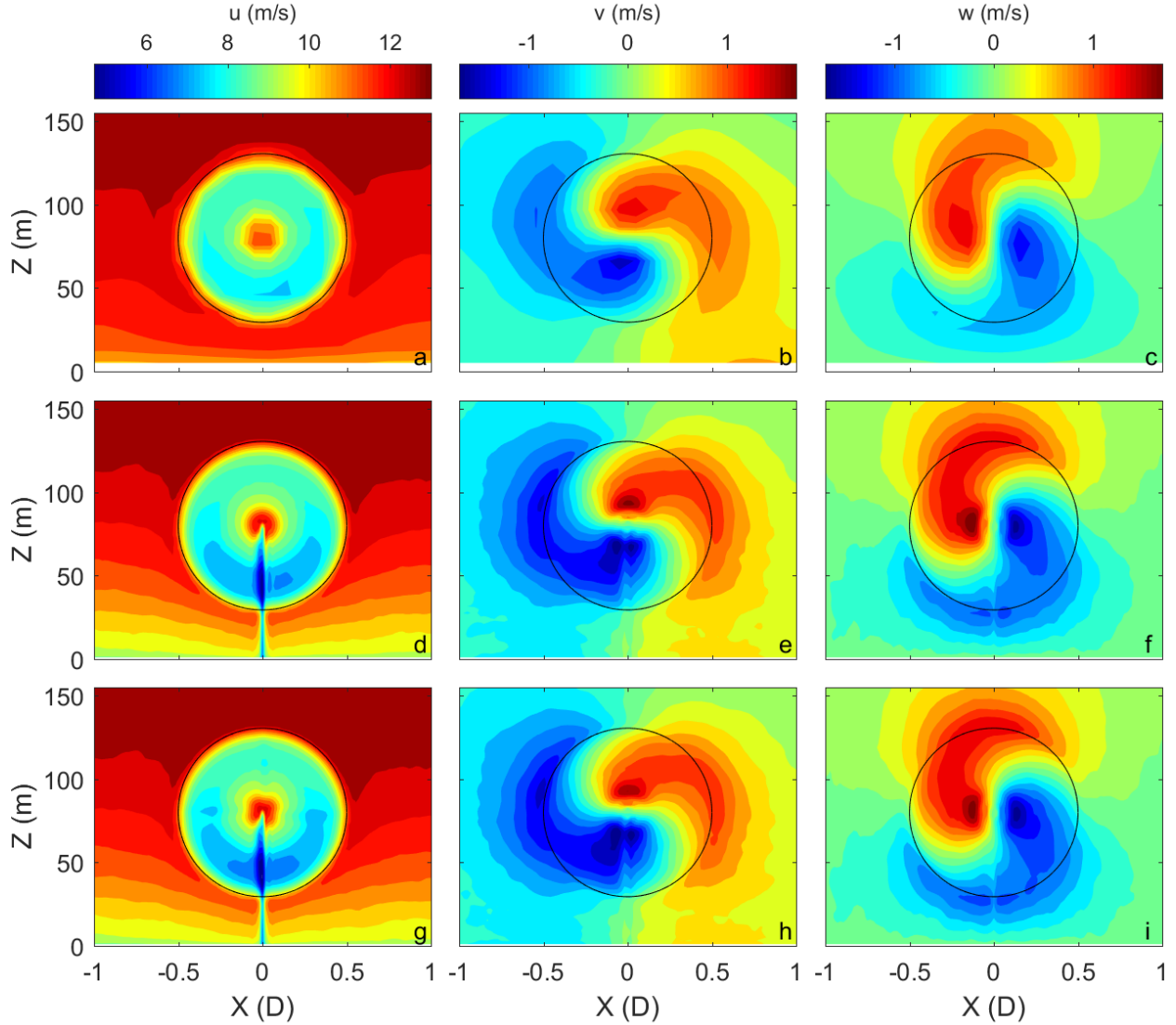
Figure 3.2: Two hour averaged velocity components (u-(a, d, g), v-(b, e, h), w-(c, f, i)) at the location of the GAD-C (a, b, c), GAD-F (d, e, f), and GAL-F (g, h, i) in the y-z plane for the CON case at 0.1D downstream. The black circle indicates the location of the GAD or GAL parameterization.

during weakly convective conditions. Wakes within the high-resolution simulations appear very similar whether using the GAL or GAD.

The velocity deficit (VD) imparted by the wind turbine parameterizations onto the flow are shown in Figures 3.6 and 3.7 for the CON and STA cases, respectively. VD values are obtained from $VD = 100(U_{LES} - U_{LESG})/U_{LES}$, where U_{LESG} is the simulation with the turbine and U_{LES} is an identical simulation without the turbine parameterization; VD

values are time averaged for comparison.

Distributions of VD values from the various simulations are consistent with those of average u-velocity from Figures 3.4 and 3.5. Maximum VD values in the wakes (disregarding tower effects) occur at approximately 2 to 4D downstream, in agreement with literature discussed previously in the introduction, and consistent with TWICS and CWEX-11 observations (discussed in Sect 3.5). Negative VD values are due to the increase of wind speed around the rotor swept area.

The evolution of the wind turbine wake for the GAD/GAL parameterizations can be compared through vertical wind profiles at distances away from the hub. Averaged horizontal wind speed profiles are shown in Figure 3.8 for all the parameterizations from the CON case at distances of -1D, 0D, 1D, 2D, 3D, 5D, 7D, and 10D in the x- (streamwise) direction from the turbine. Differences between the GAD-F and GAL-F simulations for all stability cases are insignificant. The GAD-C simulation attenuates to the background flow faster than the fine resolution (F) simulations. This is not true for the STA simulations (not shown), in which case the attenuation rates of the coarse and fine resolution simulations are comparitively indistinguishable. The CON case attenuates slightly faster to the background flow than the NEU case (not shown), and they both attenuate faster than the STA case. All profiles show similar trends for the same normalized distances away from the turbine.

Variance Comparison

Differences between the GAD-C, GAD-F, and GAL-F simulations, within each stability class, are difficult to discern solely from average velocity fields. This is especially true for differences between the GAD-F and GAL-F simulations. Examination of velocity variance reveals more differences across the different resolutions and parameterizations.

For the CON simulations in Figure 3.9, turbulence is well resolved on both the coarse and fine domains. The higher resolution domains (F), however, resolve a broader range of turbulence scales than the coarser resolution (C) simulations. Since the coarser resolution cannot capture the smaller scale motions that could break up the larger structures, the coarser-resolution simulations produce fewer, larger resolved structures (see Figure 3.1) that dominate the variance of the background flow. These larger, higher variance structures interact with the GAD to produce a broad ring of high variance of the streamwise flow component (u) within the GAD at the coarse resolution (Figure 3.9a), compared with the narrower ring of high variances in the fine resolution simulations (Figures 3.9d and 3.9g), for which background variance levels are lower.

Differences in the variance of the background flow are also evident from the v and w components, each of which likewise show enhanced variances with increasing height at the coarser resolution. The larger background w variances occurring near the surface in the fine resolution simulations (Figures 3.9f and 3.9i) are a consequence of the larger turbulent structures breaking apart into smaller structures approaching the surface. These smaller structures, which contain vertical motions, are resolved at the finer but not the coarser resolution.

While the u variance distributions for the GAD-F and GAL-F parameterizations are similar to each other (slightly larger for GAL-F), larger differences are evident for the other velocity components, especially w, each of which show enhanced variance production at the blade tips and roots owing to the aerodynamic forces being imparted along blade surfaces using the GAL (Figures 3.9h and 3.9i), rather than averaged across annular elements when using the GAD (Figures 3.9e and 3.9f).

Unlike the CON and NEU simulations (NEU not shown), resolved turbulence was not captured at the coarser resolution during the STA simulations (Figures 3.10a to 3.10c). The absence of resolved turbulence is evidenced by very small variances both in the background flow and within the GAD. The GAD still imparts strong aerodynamic forces to the flow (e.g. Figs. 3.1c and Figs. 3.5a to 3.5i), however it imparts those forces nearly uniformly in time, due to absence of large turbulence fluctuations. The finer resolution simulations do capture turbulence, although with lower energy than during CON conditions. As with the CON conditions, the differences between the variances of u between the GAD and GAL (Figs. 3.10d and 3.10g) are smaller than for the other velocity components, which again reveal enhanced variance production at the blade tips and roots in the GAL simulation (Figs. 3.10h and 3.10i).

Variance in the wake varies for the different stability cases. Figures 3.11 and 3.12 show streamwise and vertical velocity variance with downstream distance in the x-y and x-z planes for the CON and STA case, respectively. The CON case shows higher variance in both the wake and background flow, while the STA case shows the wake persisting farther downstream.

Variance of u varies in intesity in the wakes of the different cases. Figures 3.11d to 3.11e and 3.12d to 3.12f show variance of u in the x-z plane for the CON and STA cases, respectively. The largest variance occurs downstream from the top of the rotor swept area, which result from larger forces applied on the atmosphere at the top of the rotor disk due to higher wind speeds at the higher elevation. Large variance values extend from the top of the disk to similar distances for the coarse and fine resolutions, and peak at approximately 1.5 and 5D for the CON and STA cases, respectively. Smaller local variance maxima are observed near the bottom of the rotor swept area. Local variance minima are observed near the hub and tower for the fine resolution simulations.

The variance in the x-y plane for the CON case is stronger in the wake for the coarse resolution simulation and weaker for the fine resolution simulations (particularly in the near-wake) (Figures 3.11a to 3.11c). The variability at hub height attenuates earlier downstream due to the higher background variance in the coarse resolution simulations. The coarse resolution simulation cannot resolve the range of smaller scale motions that could break up larger turbulence structures, and thus produces fewer much larger resolved structures in the flow than the finer resolution simulations, as discussed previously. Figures 3.12a to 3.12c display results from the STA simulations, showing that the coarser resolution simulations feature much smaller variance values, particularly near the wake center (in the near-wake) when compared to the fine resolution simulations.

Vertical velocity (w) variances during both CON and STA conditions are shown in Figures 3.11g to 3.11i and 3.12g to 3.12i. The fine resolution simulations show larger variance values

within the wakes than the coarse resolution simulations. The variance is slightly greater for the GAL-F simulations when compared to the GAD-F simulations.

Case(s)	Domain	n_x	n_y	n_z	Δx (m)	Δz (m)	L_x (m)	L_y (m)	L_z (m)	T_x (m)	T_y (m)
CON-GAL-F, CON-GAD-F,	outer domain	524	262	145	6	2	3138	1566	1636	-	-
NEU-GAL-F, and NEU-GAD-F	nested domain	814	406	145	2	2	1626	810	1636	417	405
CON-GAD-C and NEU-GAD-C	outer domain	268	135	64	30	10	8010	4020	1700	-	-
	nested domain	415	214	64	10	10	4140	2130	1700	2070	1070
STA-GAD-F and STA-GAL-F	outer domain	423	217	127	6	2	2532	1296	2969	-	-
	nested domain	631	325	127	2	2	1260	648	2969	418	324
STA-GAD-C	outer domain	242	57	67	18	6	4338	1008	3077	-	-
	nested domain	376	106	67	6	6	2250	630	3077	1254	318

Table 3.1: Computational and physical dimensions of the GAL and GAD simulation domains for the TWICS weakly convective (CON) and neutral (NEU) cases, and the CWEX-11 stable (STA) case. n_x, n_y, and n_z represent the number of grid points in the x, y, and z directions. Δx and Δz represent the horizontal and vertical grid spacings. L_x, L_y, and L_z represent the domain dimensions. Δz is an approximate value for $z < 200$ m, above which it is stretched. T_x is the turbine hub location from the nested domain's left side in the X direction (streamwise), and T_y is the hub location from the bottom of the nested domain in the Y direction (spanwise).

Case	Geostrophic Wind Direction (°)	Geostrophic Wind Speed (m s^{-1})
CON-GAD-C	24.8	14.8
CON-GAD-F and CON-GAL-F	26.5	14.7
NEU-GAD-C	26.8	16.3
NEU-GAD-F and NEU-GAL-F	26.5	16.5
STA-GAD-C	31	11
STA-GAD-F and STA-GAL-F	35	13.5

Table 3.2: Geostrophic wind forcing on the outer domain for each stability and grid resolution. The geostrophic wind direction is reported clockwise from the X axis.
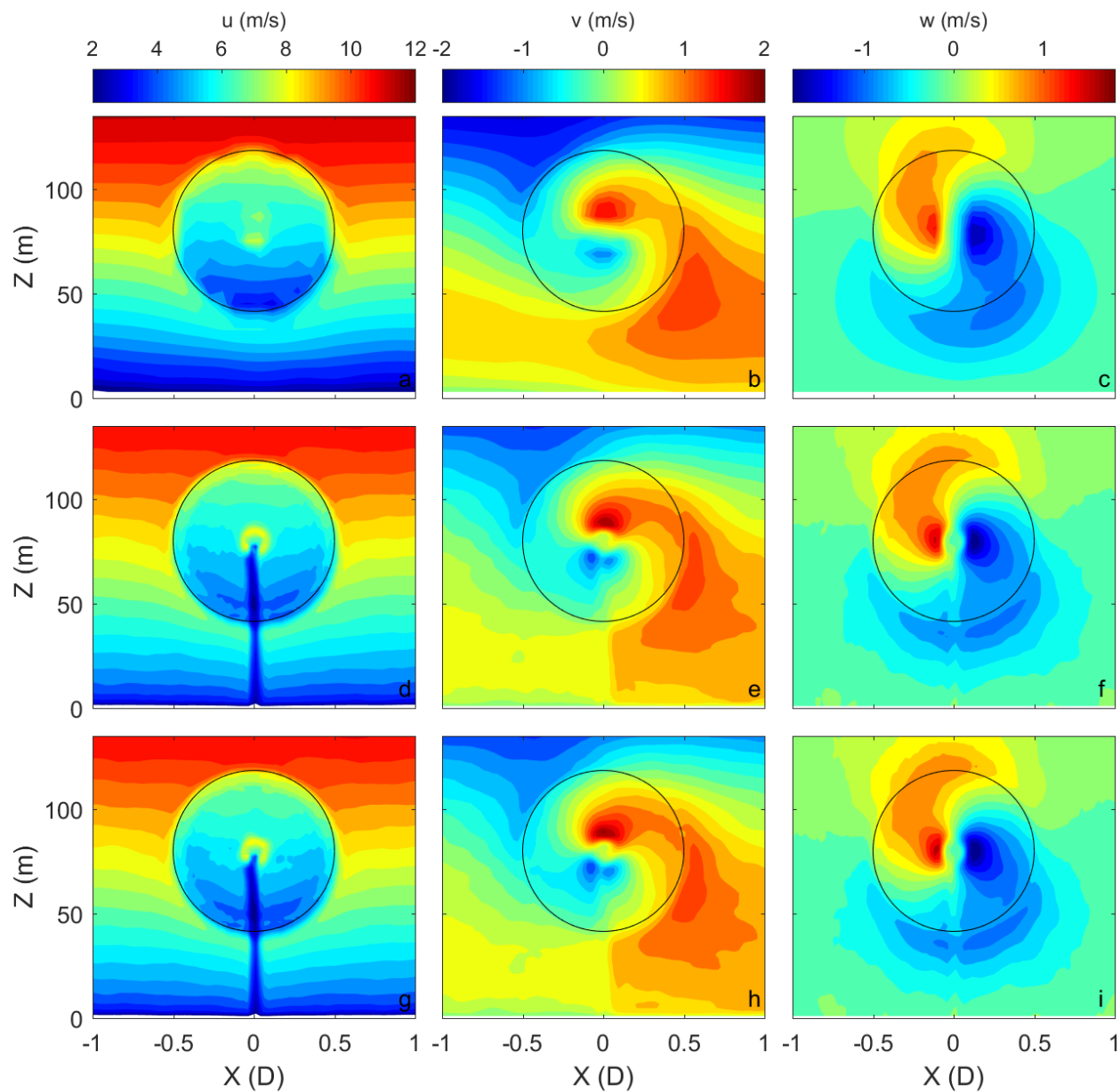
Figure 3.3: Forty minute averaged velocity components (u-(a, d, g), v-(b, e, h), w-(c, f, i)) at the location of the GAD-C (a, b, c), GAD-F (d, e, f), and GAL-F (g, h, i) in the y-z plane for the STA at 0.1D downstream. The black circle indicates the location of the GAD or GAL parameterization.
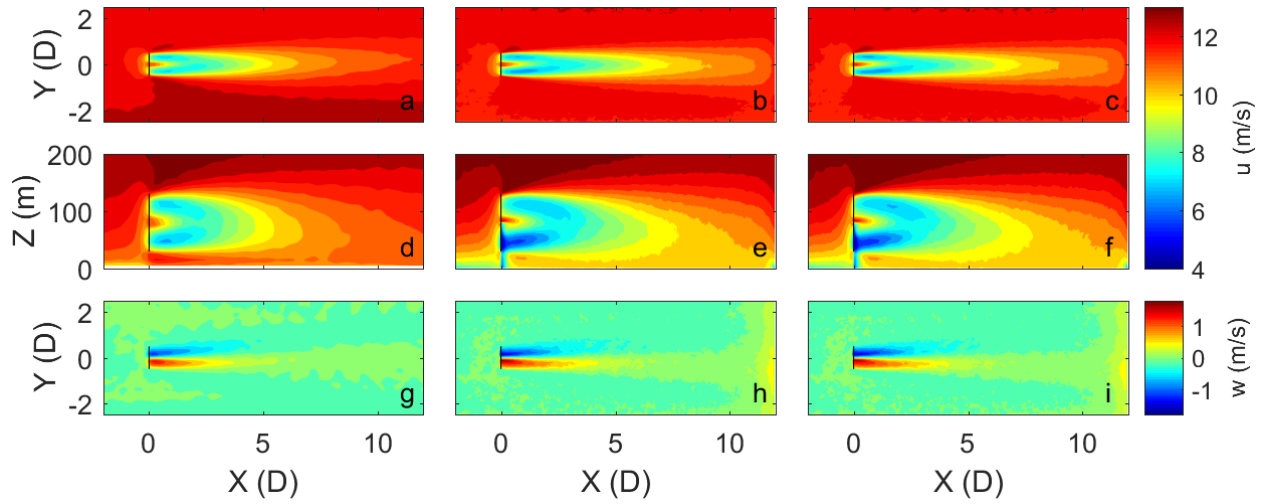
Figure 3.4: Two hour averaged velocity components (u (a-f), w (g-i)) at 80 m hub height (a-c and g-i) and turbine location in the y direction (d-f) from the GAD-C (a,d,g), GAD-F (b,e,h), and GAL-F (c,f,i) for the CON simulations. The black line indicates the location of the GAD or GAL parameterization.
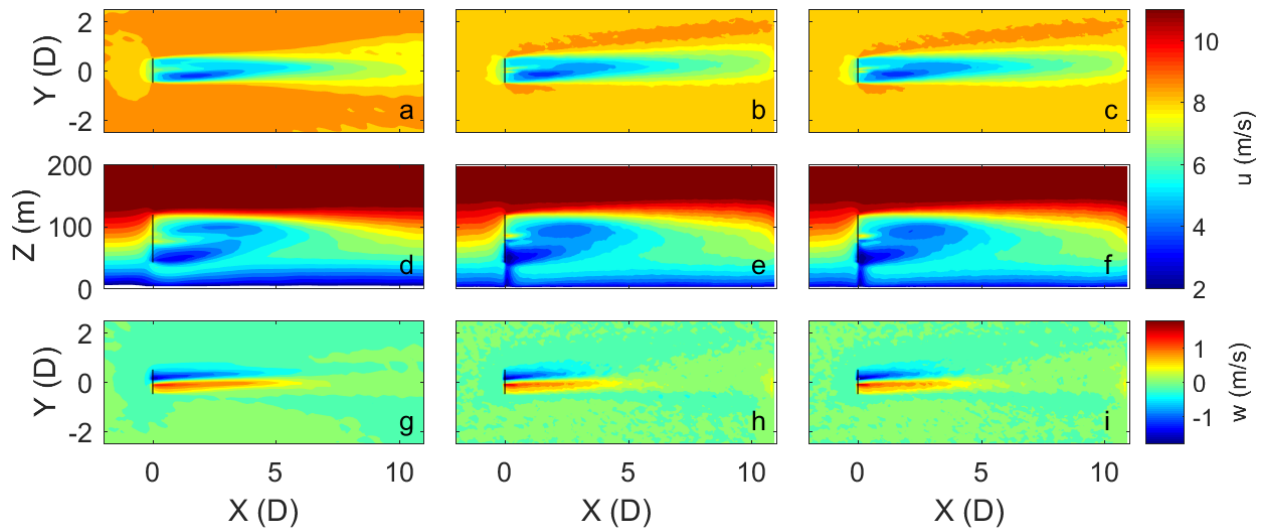
Figure 3.5: Forty minute averaged velocity components (u (a-f), w (g-i)) at 80 m hub height (a-c and g-i) and turbine location in the y direction (d-f) from the GAD-C (a,d,g), GAD-F (b,e,h), and GAL-F (c,f,i) for the STA simulations. The black line indicates the location of the GAD or GAL parameterization.

(a) (b) (c)

(d) (e) (f)
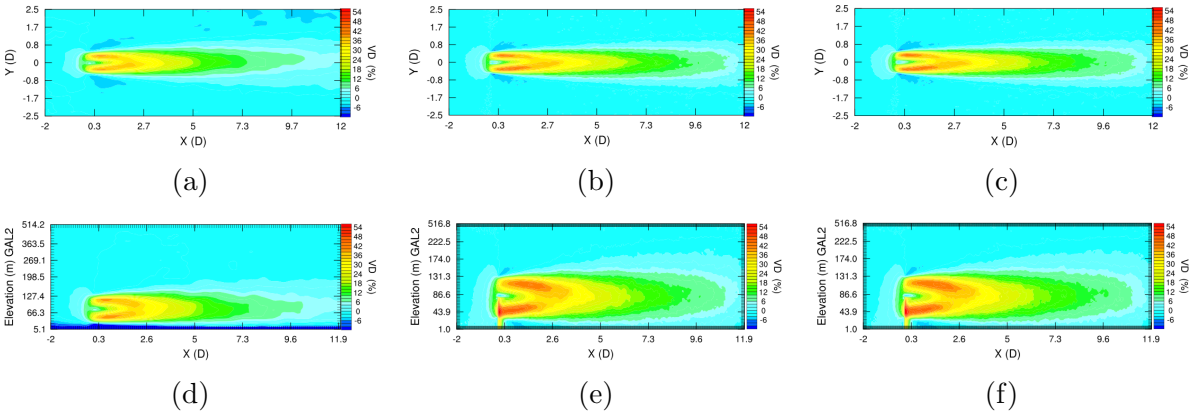
Figure 3.6: Two hour averaged velocity deficit (VD) in the x-y (a-c) and x-z (d-f) planes at hub height and hub location in the y direction, respectively. The GAD-C (a, d), GAD-F (b, e), and GAL-F (c, f) results for the CON case are shown.

(a) (b) (c)

(d) (e) (f)
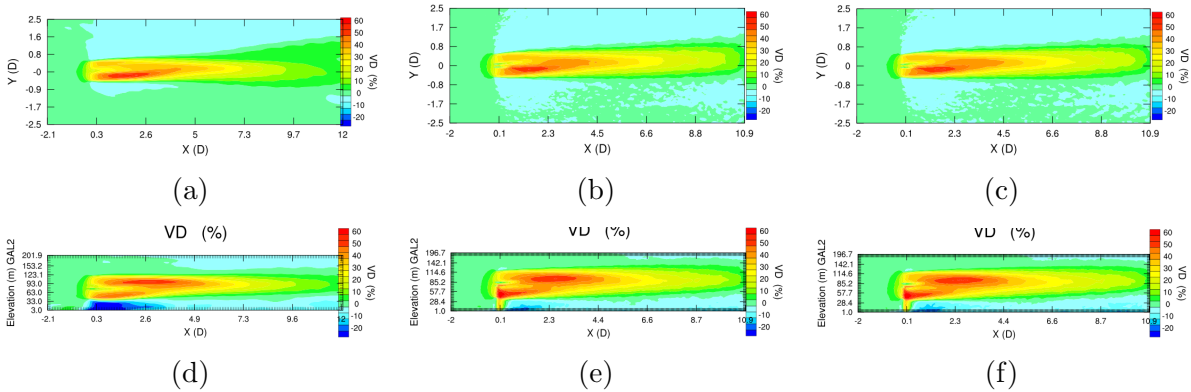
Figure 3.7: Forty minute averaged velocity deficit (VD) in the x-y (a-c) and x-z (d-f) planes at hub height and hub location in the y direction, respectively. The GAD-C (a, d), GAD-F (b, e), and GAL-F (c, f) results for the STA case are shown.
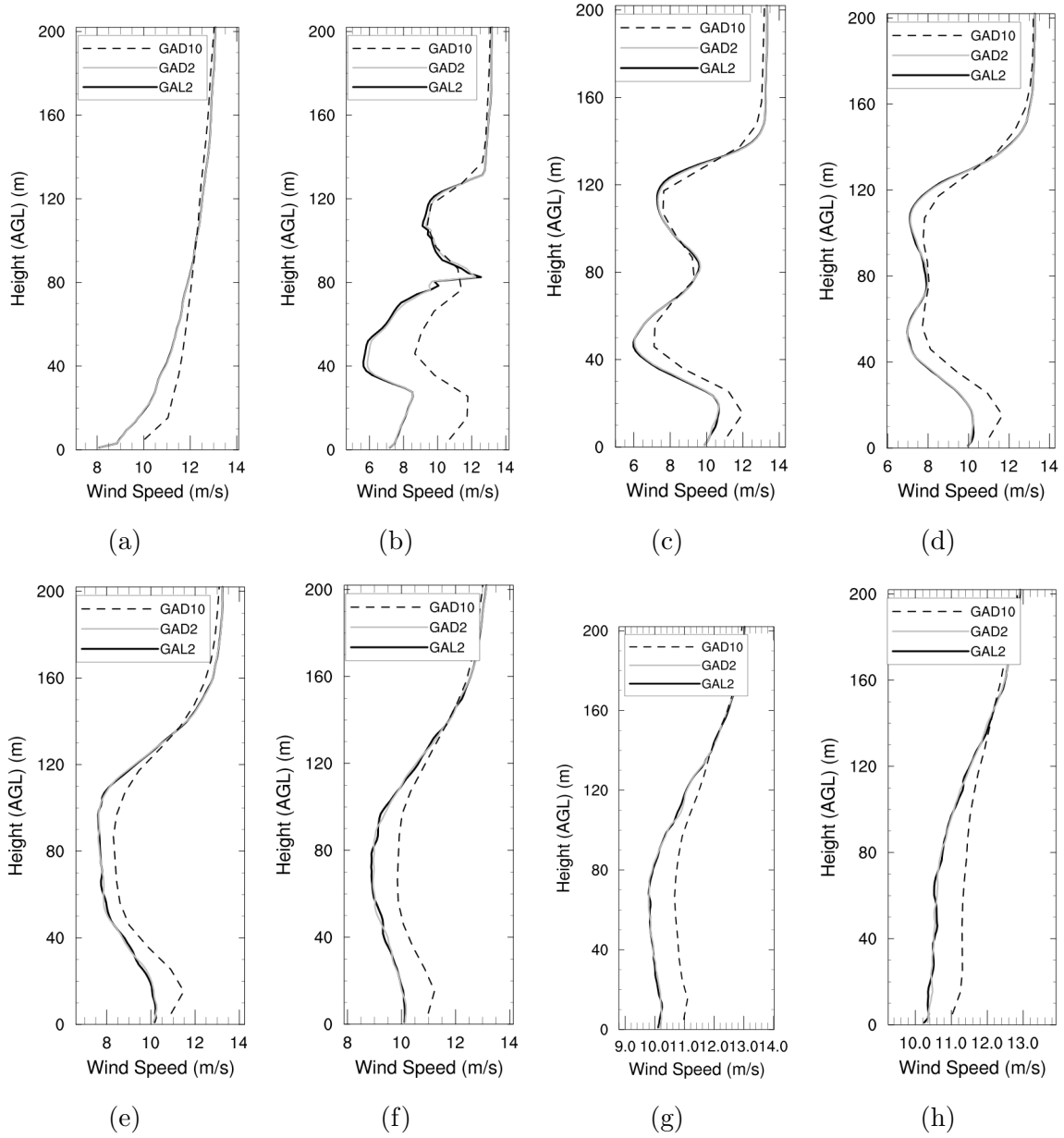
Figure 3.8: Two hour averaged horizontal wind speed profiles one rotor diameter (D) directly upwind of the turbine hub (a), at the turbine hub (b), 1D downstream of the hub (c), 2D downstream (d), 3D downstream (e), 5D downstream (f), 7D downstream (g), and 10D downstream (h) for the CON case. Results are from the GAD-C, GAD-F, and GAL-F simulations.
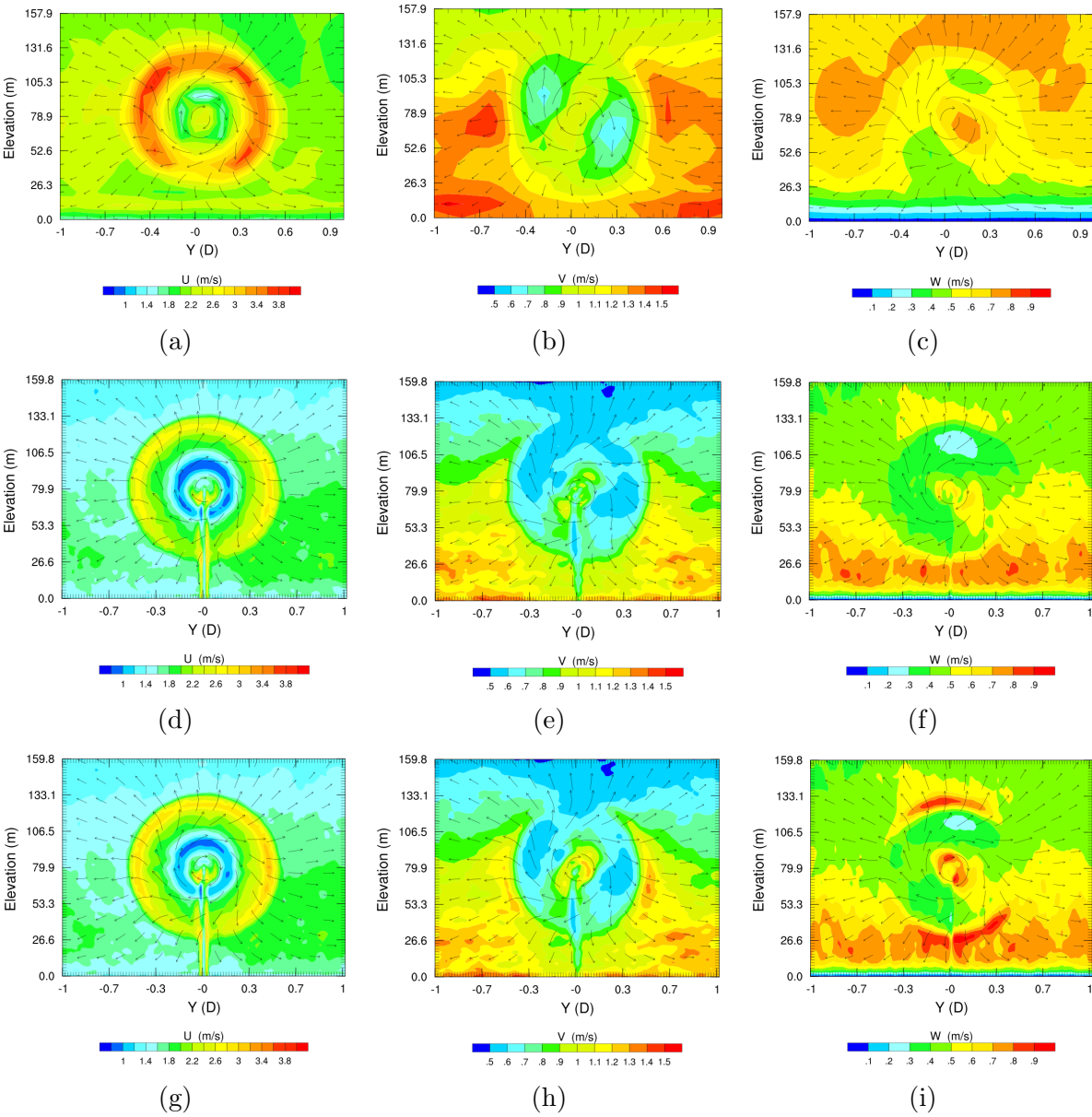
Figure 3.9: Two hour variance of velocity components (u-(a, d, g), v-(b, e, h), w-(c, f, i)) at the location of the GAD-C (a, b, c), GAD-F (d, e, f), and GAL-F (g, h, i) in the y-z plane for the CON case at 0.1D downstream.
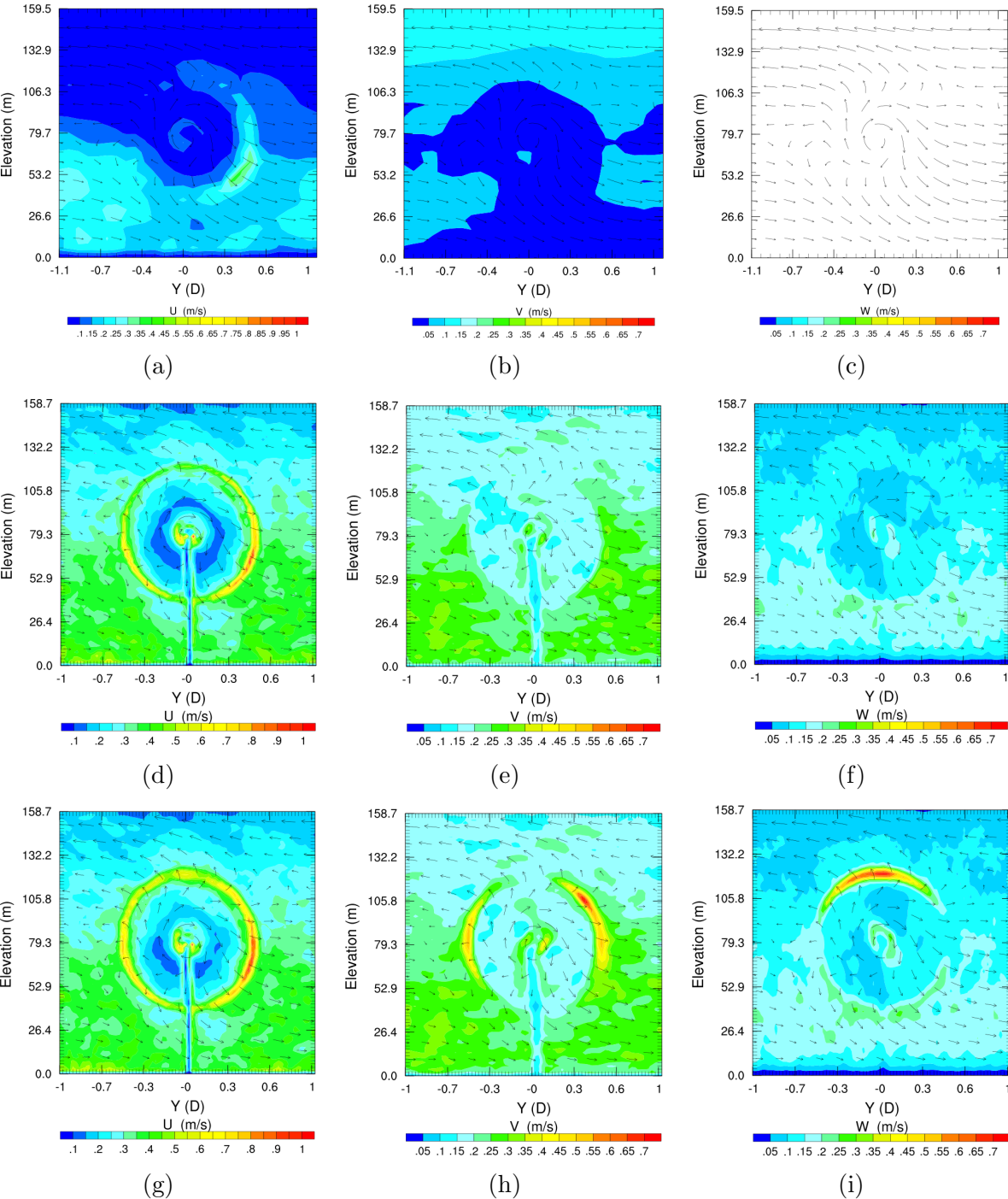
Figure 3.10: Forty minute variance of velocity components (u-(a, d, g), v-(b, e, h), w-(c, f, i)) at the location of the GAD-C (a, b, c), GAD-F (d, e, f), and GAL-F (g, h, i) in the y-z plane for the STA case at 0.1D downstream.
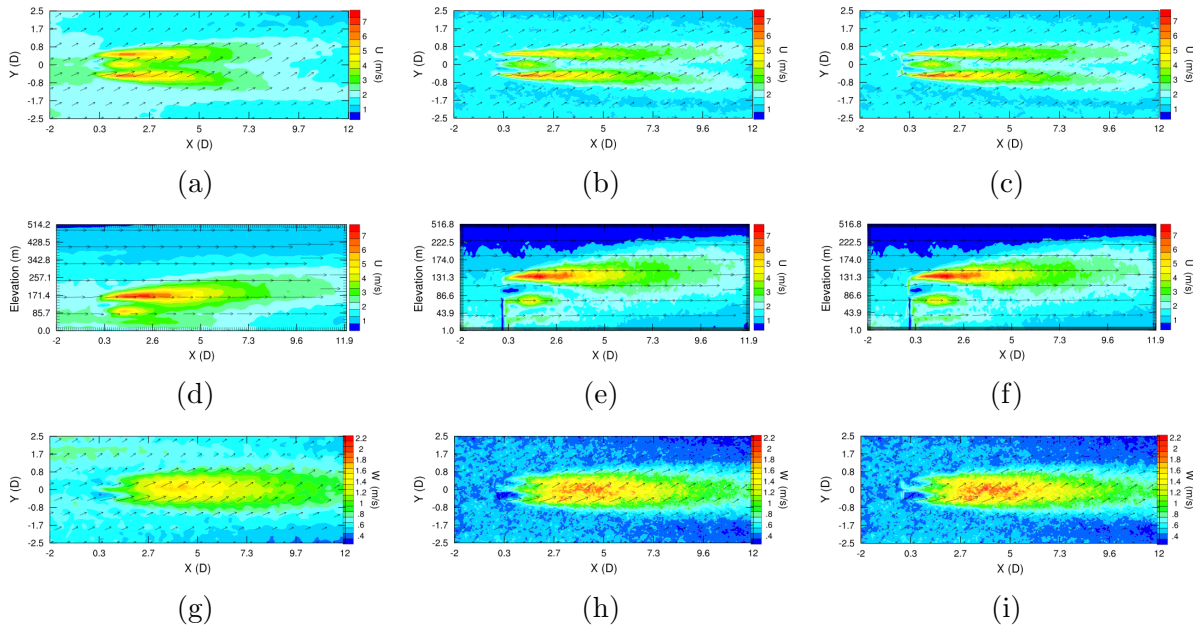
Figure 3.11: Two hour variance of velocity components (u (a-f), w (g-i)) at 80 m hub height (a-c and g-i) and turbine location in the y direction (d-f) from the GAD-C (a,d,g), GAD-F (b,e,h), and GAL-F (c,f,i) for the CON simulations.
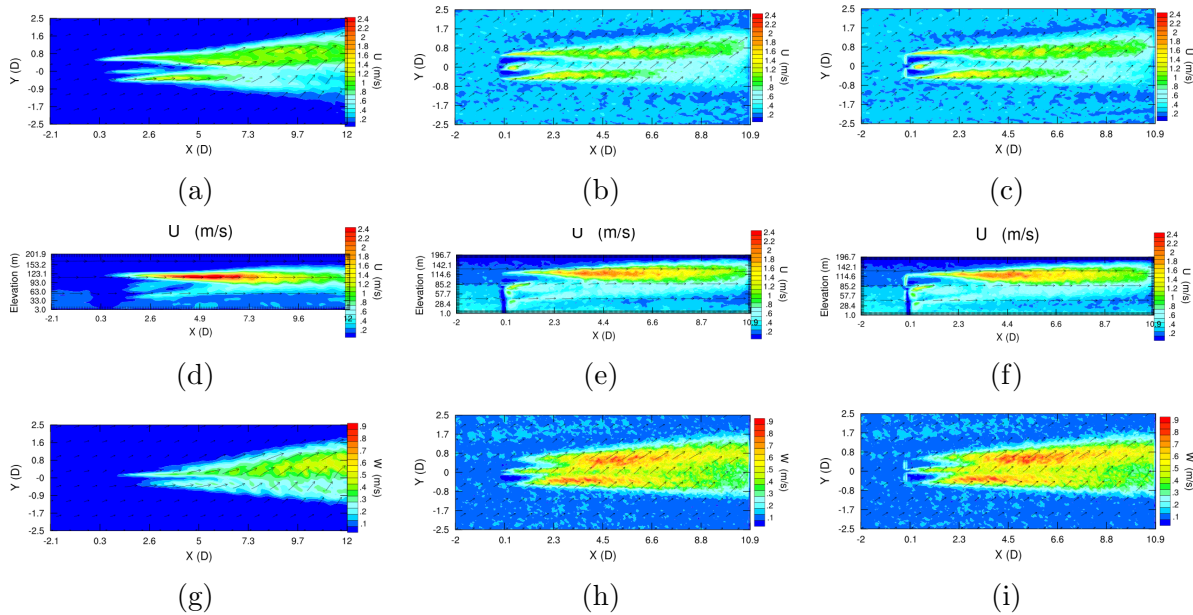
Figure 3.12: Forty minute variance of velocity components (u (a-f), w (g-i)) at 80 m hub height (a-c and g-i) and turbine location in the y direction (d-f) from the GAD-C (a,d,g), GAD-F (b,e,h), and GAL-F (c,f,i) for the STA simulations.

Vorticity

Differences between the GAD-C, GAD-F, and GAL-F are difficult to discern with comparison of their velocities, particularly between the GAD-F and GAL-F. These differences become clearer, especially between the coarse resolution and fine resolution simulations, with comparison of their velocity variance values. In this section vorticity is compared, as the GAL parameterization has the ability to impart tip and root vortices onto the wake's flow and thus better represent turbulent structures in the near wake when compared to the GAD parameterization. Unfortunately, there are no field measurements for vorticity behind a wind turbine and thus no method to quantify simulation results against observations.

Instantaneous vorticity reveals significant differences between wind turbine wakes for the GAL and GAD parameterizations. Figure 3.13 shows instantaneous three-dimensional isosurfaces of the magnitude of vorticity $(\|\omega\| = \sqrt{(\frac{\partial w}{\partial y} - \frac{\partial v}{\partial z})^2 + (\frac{\partial u}{\partial z} - \frac{\partial w}{\partial x})^2 + (\frac{\partial v}{\partial x} - \frac{\partial u}{\partial y})^2})$ from the GAL-F (left column) and GAD-C (right column) parameterizations, during CON (Figs. 3.13a to 3.13b). Both parameterizations show vorticity production around the tower and hub, however, only the GAL shows distinct vortices shed off the tips and roots of the blades and propagating downstream to form helical vortex tubes. Vorticity is likewise produced near the perimeter of the disk for the GAD parameterization, but with smaller magnitudes, hence are not depicted within the isosurface shown in Figs. 3.13b, 1c, and 1e. The vorticity isosurfaces farther downstream in the wake are similar for both GAL and GAD as the vortex tubes from the GAL eventually break down into the surrounding atmospheric turbulence as the flow transitions into the far-wake (2-4D).

(a)   (b)
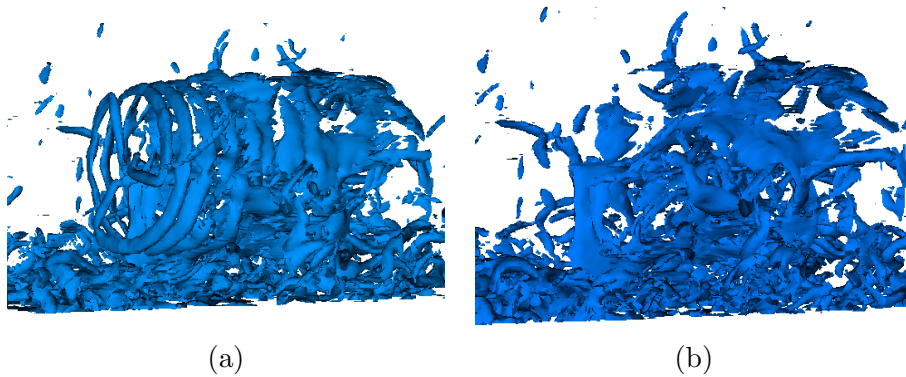
Figure 3.13: Instantaneous 3-D isosurface of the magnitude of total vorticity (ω) for the CON-GAL-F (a) and CON-GAD-F (b) simulations. All isosurfaces are valued at 1.38 s^{-1} and instantaneous at hour 16:04:40.

To further distinguish differences between the GAD and GAL parameterizations at the same (F) resolution, cross sections of instantaneous values of $\|\omega\|$ for the GAD-C, GAD-F, and GAL-F parameterizations are shown in Figure 3.14 for the CON case. Comparison of CON and STA conditions demonstrates that the coarse resolution simulations do not resolve the smaller, higher magnitude vorticity structures when compared to the fine resolution simulations. All simulations show an increase in vorticity at the edges of the rotor disk, in the center near the hub, and in the wake. The GAL-F and GAD-F simulations are able to resolve the small, higher magnitude vorticity shedding off the edges of the disk and at the center near the hub, however, only the GAL parameterization demonstrates shedding of higher magnitude tip and root vortices that manifest as helical vortex tube structures. The differences between the GAD-F and GAL-F parameterizations are only clearly evident to distances of approximately 1D downstream, after which the differences dissipate farther downstream into the far-wake where the structure of the helical vortex tubes disappears in the GAL simulation.

Averaged vorticity in the turbine wake shows differences between the cases. Figures 3.15 and 3.16 show time averaged magnitude of vorticity for the CON and STA cases. The helical vorticity structure shed off the tips and roots of the blades in the wake is not present in the averaged GAL simulations as in the instantaneous cross-sections previously discussed. As with the instantaneous cross-sections, all the cases show increased vorticity, on average, at the edges and center of the disk as well as in the wake. Vorticity is more persistent downstream in the wake for the STA case than for the CON case. This is likely due to more rapid dissipation of turbine induced vorticity by the stronger background mixing present in the CON case. The fine resolution simulations are, unlike the coarse resolution simulations, able to resolve smaller turbulent structures. The fine resolution simulations show vorticity is greater, on average, at the center of the disk (at the hub) than at the tips, most likely due to the additive effect of the resolved turbine hub, tower, and root vortices. The GAL parameterization displays stronger and more persistent vorticity in the near wake at the tips of the blades, but unlike in the instantaneous cross-sections, vorticity is also clearly larger farther downstream in the wake for the GAL-F when compared to the GAD-F.

Wake Comparison with Observations

Observations from the two field campaigns discussed in Section 3.3 provide data for comparison of wake characteristics. Velocity deficits as a function of downstream distance are compared to scanning lidar observations from TWICS during the CON simulations. During STA conditions, profiles of streamwise velocity and its variance at one location upstream and downstream from the turbine are compared to profiling lidar data from CWEX-11.

TWICS-2011 CON and NEU case comparison

Data from the High Resolution Doppler Lidar (HRDL) described in section 3.3 are used to estimate the wake velocity deficit, thus enabling comparison of results from the LES with
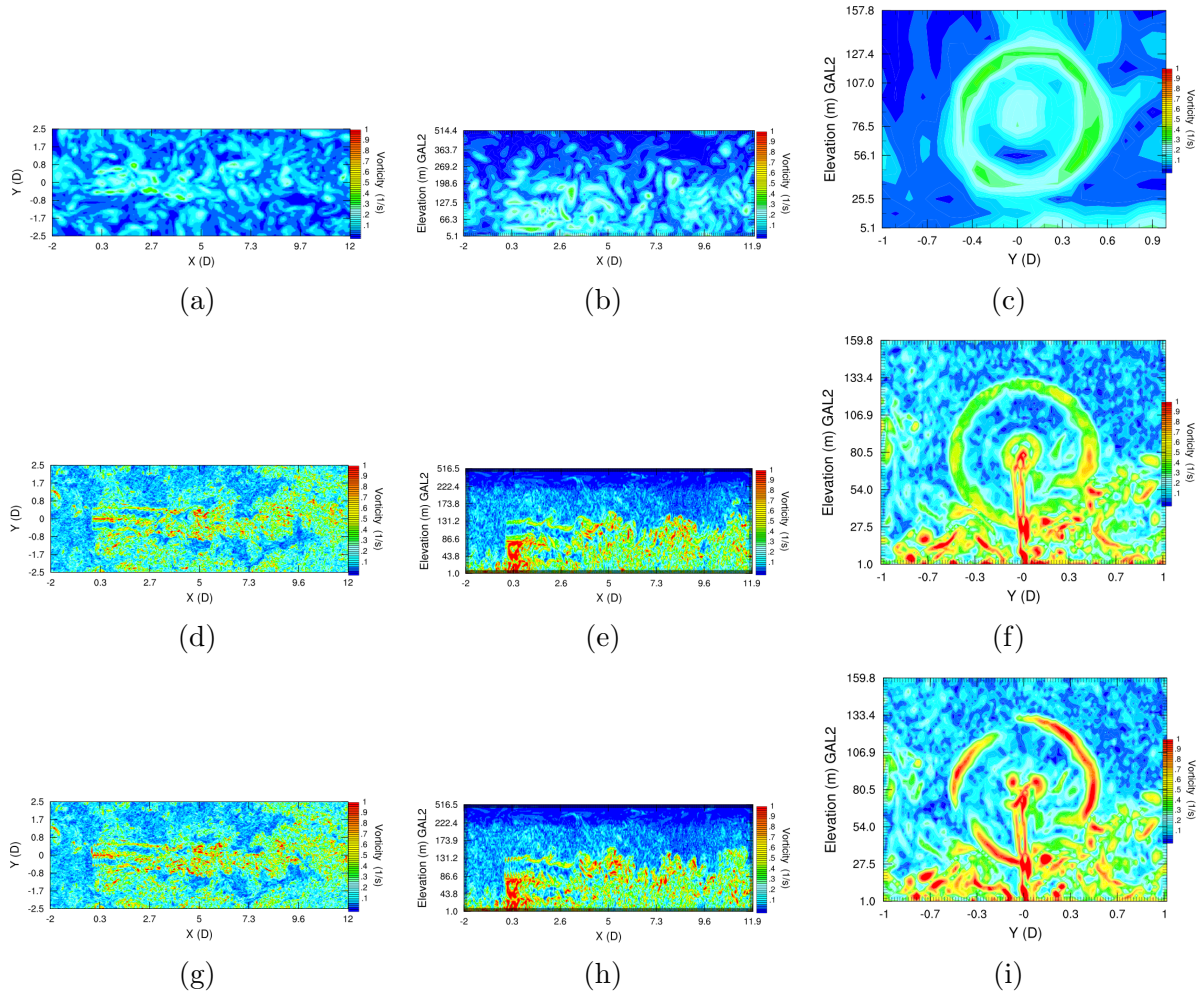
Figure 3.14: Instantaneous contours of the magnitude of vorticity for GAD-C (a-c), GAD-F (d-f), and GAL-F (g-i) in the x-y (a, d, g), x-z (b, e, h), and y-z (c, f, i) planes at hub height, hub location in y, and 0.2D downstream of hub in x, respectively. These results are at 16:40 UTC and for the CON case.

the observations. An algorithm developed by Aitken et al. (2014a) and used by Mirocha et al. (2014) enables the comparison of WRF simulation results with HRDL PPI scan observation data. To determine the horizontal structure of the wake from PPI scans, the ambient wind (outside the wake) in the scan is assumed of uniform wind speed and direction. The wake is represented as either a single or symmetric double-Gaussian function subtracted from the uniform background flow to account for the difference between the shape of the velocity deficit profile in the near and far wakes. A Gaussian function is specifically chosen because in the near wake, the velocity deficit profile in the transverse and vertical directions depends on the amount of lift produced along the span of the blade. Very little lift is generated at
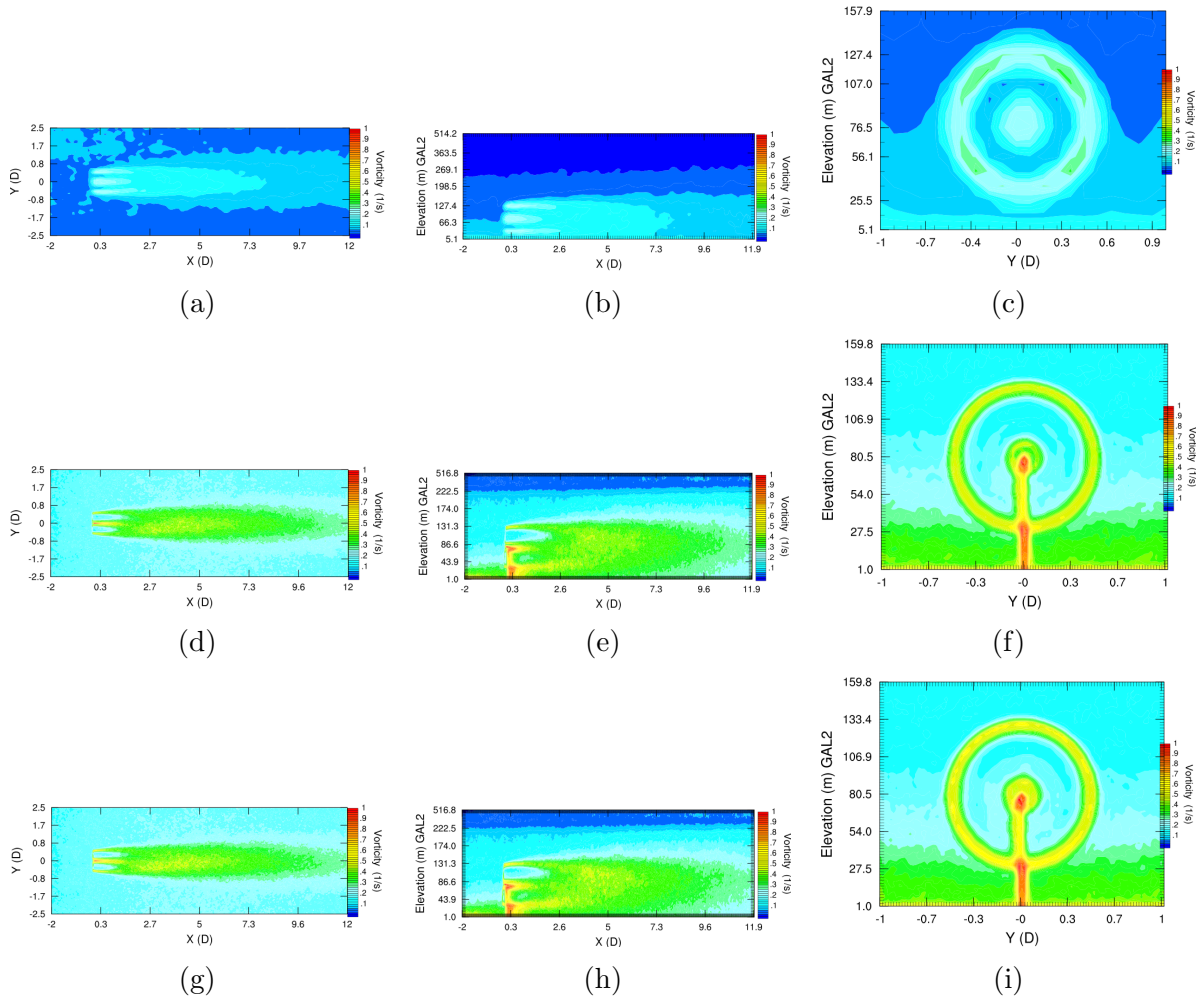
Figure 3.15: Two hour averaged magnitude of vorticity contours for GAD-C (a-c), GAD-F (d-f), and GAL-F (g-i) in the x-y (a, d, g), x-z (b, e, h), and y-z (c, f, i) planes at hub height, hub location in y, and 0.2D downstream of hub in x, respectively. These results are for the CON case.

the blade root due to its aerodynamics and at the end of the blades due to tip vortices. Maximum lift is generated at approximately 0.75R (where R is the radial distance along the turbine blade away from the root), and as a result the velocity deficit profile contains two local minima that correspond roughly to these points along the blades. In the far wake, turbulent mixing results in the merging of the two troughs (minima) to form a single trough, which is approximately Gaussian in shape (Magnusson and Smedman, 1999). A parameterized statistical model (Aster et al., 2013) for the Gaussian distribution is fit to the measured transverse horizontal wind speed profile at each range gate within each scan. The velocity deficit (VD) between the ambient wind speed and that inside the wake (Vermeer

et al., 2003), along with various other wake characteristics, is determined from parameters in the statistical model, whose best-fit values are obtained using weighted nonlinear regression, in which observation weights are specified using the Cramer-Rao lower bound (Rye and Hardesty, 1993). For more details, refer to Aitken et al. (2014a).

Mirocha et al. (2014) used horizontal plan-position (PPI) observation scans of radial velocity obtained at an elevation of 2 degrees, which intersected the turbine near hub height (see Figure 7 from Mirocha et al. (2014)). Each PPI scan provides a quasi-instantaneous snapshot of the flow field and lasts about 20 seconds. The VD values used in this study are the same as those calculated from the HRDL data (outlined by Aitken et al. (2014a)) as in Mirocha et al. (2014), which depict the distribution of VD as a function of downstream distance from all PPI scans occurring between 13:00 and 17:10 MST on 22 April, 2011 at 80 m hub height. These are shown in Figure 3.17. The blue central line depicts the median value, while the shaded region indicates one standard deviation on either side. VD values from the LES, computed using the same algorithm as applied to the observations, are also shown for the CON and NEU cases for the GAD-C, GAD-F, and GAL-F LES simulations.

While the GAD-C simulations show smoothly varying VD values, those from the finer resolution simulations oscillate within the first 1D downstream. These oscillations are likely due to the fine resolution simulations capturing more variability in the near wake which prevents the algorithm from consistently discriminating wake signatures from the background turbulence variability. VD values from the GAD-C simulations differ somewhat from those in Mirocha et al. (2014) due to subsequent improvements to the turbine operational parameterizations, as well as incorporation of hub and tower drag, and turbine tilt and offset from the tower. The coarse resolution simulations agree better with the median observation values in the near wake, and the fine resolution simulations agree better in the farther wake closer to 5.5D, however, they are both in the envelope of the observations. The GAL-F and GAD-F parameterizations compare very similarly to the observed VD values in the wake, according to the wake detection algorithm. The CON and NEU cases compare similarly, with the NEU case for both coarse resolution and fine resolution simulations showing slightly larger VD values.

Root-mean-square (RMSE) and mean-absolute (MAE) errors for the differences between the mean of the observation and simulation VD, averaged over the range gates from 0 to 5.5D, all show similar values. These range from a low RMSE of 3.29% and MAE of 2.65% for the CON-GAD-C case to a high RMSE of 6.52% and MAE of 5.64% for the NEU-GAD-F case. The smallest errors are present in the GAD-C simulations and the differences between the GAD-F and GAL-F simulations are minor.

CWEX-11 stable case comparison

To facilitate comparison with the lidar measurements at CWEX, a lidar-based simulation sampling strategy was utilized. Flow parameters were sampled along four lines corresponding to the lidar beams, emanating from the Windcube lidar locations at 2.2D upstream (L1) and 3.5D downstream (L2) of the turbine, as at CWEX-11. Real lidars sample Doppler shifts

along lines of sight to derive the velocity components. For the simulation results, grid cell-centered points within the horizontal grid spacing distance, Δx, of the beam path were interpolated and weighted (Gaussian) from their respective vertical distribution to heights corresponding to each lidar range gate (see Mirocha et al. (2015) and Lundquist et al. (2015) for details). Values from grid cells near the beams were averaged over each height within each range gate, and over all four beams (at 1 Hz). The 1 Hz values were then averaged over 2 minutes, consistent with the lidar output, with variance of u, the streamwise component, calculated for each 2-minute period.

Averaged wind profile comparison between simulations and observations helps clarify differences. Figure 3.18 shows 2-minute averaged wind speed, wind direction (λ), and variance of u (σ_u) profiles from L1 and L2 during 40 minutes of the STA simulation. Horizontal blue and red lines show the observed range of 2-minute averaged values from L1 and L2 over the four-hour period, while light blue and orange lines depict simulated data from those locations. The vertical hatch marks on the horizontal lines show the average for the observed ranges. The figure shows 20 2-minute average profiles obtained when λ at 80 m above the surface was close to 180 degrees.

Wind simulation results with the GAL implementation compare well with the GAD implementation. Figure 3.18abc shows results very similar to Mirocha et al. (2015) for winds close to 180 degrees for the coarse resolution simulations. The u velocity and wind direction in the wake at L1 and L2 are almost identical to Mirocha et al. (2015), however some of the variance values of u are slightly smaller in magnitude.

The GAL and GAD simulations both compare well with observations. Figures 3.18def and 3.18ghi show 20 2-minute average profiles for the GAD-F and GAL-F simulations, respectively, during which wind directions at 80 m are close to 180 degrees. The wind speeds from the coarse and fine resolution simulations compare well to observation data at L1 and L2, however, variance of u increases progressively at L1 and L2 from the GAD-C to the GAD-F, to the GAL-F. The GAL-F simulation shows larger variance in its profiles than the GAD-F simulation to further confirm an increase in turbulence with the GAL parameterization.

In order to determine why the simulated variances are significantly smaller in magnitude than the observed values, Fig. 3.19 shows 20 2-minute average profiles, as in Fig. 3.18, but at each vertical grid index with no weighting along the beam direction. The unweighted profiles show better agreement with wind speed lidar observations in the wake and greater variability in the simulation results when compared to the weighted profiles from Fig. 3.18. Variance of u is significantly larger for the unweighted results, especially at the top of the turbine in the wake. There is a striking increase in variance from the GAD-C to the GAD-F, which reaches its greatest magnitude for the GAL-F simulation results.

Neither weighted nor unweighted results compare favorably with the downstream lidar variance observations. Assuming observation accuracy, the GAL parameterization is characterized by larger variance at the top and bottom of the rotor disk, closer to observation values, than the GAD parameterization. Including tip vortices (as the GAL does), however, is not sufficient to produce the intensity of variance farther downwind as the observations indicate. A likely reason for this under-prediction is the inability of the parameterizations to

accurately model the interaction of the hub vortex with the rotor tip shear layer, because the parameterizations cannot resolve the geometric details of the hub region instrumental to this interaction (Kang et al., 2014). The GAD/GAL parameterizations under-predict the intense velocity fluctuations that manifest in observations and turbine resolving models as a slowly precessing spiral hub vortex that augments the tip vortices. The observations from CWEX show substantially larger variance at the bottom of the turbine rotor disk when compared to the top. Others, such as Kang et al. (2014), have shown greater TKE (analogous to velocity variance) at the top of the turbine rotor (when compared to the bottom) for GAL, GAD, and turbine resolving models. The CWEX velocity variance observations are thus possibly affected by the plant canopy on site, instrument error, or meteorological phenomena not represented in these simulations.

3.6 Summary and conclusions

A generalized actuator line wind turbine parameterization was implemented into the Weather Research and Forecasting model to provide a high-fidelity simulation capability for the examination of turbine-airflow interactions and wake formation and propagation in atmospheric large eddy simulations. The GAL, an extension of the validated GAD already implemented into WRF, provides higher fidelity simulation of the near wake region by applying the aerodynamic forces along each of the blades during rotation throughout the rotor plane, rather than averaging the forces over annular elements within the disk, as the GAD. The GAL is validated herein against both the GAD and against field data under weakly stable, neutral, and weakly convective conditions. The GAD simulations were also performed on a finer grid to isolate the effects of resolution on the differences between the GAD and GAL.

The impacts of actuator model type and model resolution on wake properties, including velocities, variances, and vorticity, were examined. Simulations from all stability classes revealed only small differences between the GAL and GAD parameterizations when comparing their instantaneous and averaged velocity fields at the same resolution beyond the near wake. Comparing the variances reveals slightly larger differences between the parameterizations, the largest of which were for the w component of velocity, especially in the downstream wake and the outer edges of the disk. While resolution and parameterization type both influence the variances, the source of significant disagreement in simulated versus observed variance profiles remains an open question.

The largest differences between the GAL and GAD parameterizations are evident when vorticity is compared for the two at the same resolution. Only the GAL shows root and tip vortices expected from a wind turbine, while the GAD shows weaker vorticity around the edges of the disk and at the turbine hub. The fine GAD simulations, however, resolve smaller and higher magnitude vorticity structures that are plausibly more accurate than those from the coarse resolution simulations. The vorticity tubes generated at the tips and roots of the blades for the GAL are visually distinguishable from the GAD up to about 1D downstream

of the turbine, until they mix in with the rest of the wake and the turbulence structure appears similar to the GAD.

While the aggregated velocity deficits beyond the near wake generally agree well across resolutions and model types, differences are significant in the small-scale structure near the rotor plane. Fine-scale structures containing large departures from the mean velocity, and high levels of vorticity, are not captured by the coarsest resolution simulations for the weakly convective case. The stable case shows similar velocity deficits for both coarse and fine resolutions due to the lack of resolved variability in the background flow. The coarse resolutions also fail to resolve much of the turbine hub and the entire tower, which further results in higher magnitude wind velocities in the near wake.

The use of fine resolution with the wind turbine parameterizations, presented in this study, indicates potential benefits over coarser resolution by providing higher-fidelity resolution of wake structures, including vorticity, and smaller turbulence structures impacting variance. For stable atmospheric conditions, resolution suitable for the GAL model is likely required to capture the boundary layer turbulence. High resolution comes at a significantly higher computational expense (due to the smaller model timestep required by the finer resolution, increasing resolution by a factor of 2 increases computational cost by a factor of 16; additional overhead from the GAL is insignificant), in which case coarse resolution GAD simulations can perform well in representing the effects of a wind turbine on the ABL. When simulation of the average wake effects of a wind turbine on wind speed (or velocity deficit) is desired, use of fine resolution GAD or GAL simulations bestows incremental benefit over what can be achieved from the use of coarser GAD simulations. If, however, accurate simulation of the turbulence or vorticity structures of a wake is desired, the use of high resolution GAL or GAD simulations shows noticeable benefit. The benefits of GAL over GAD are small, but may be important, especially within 1 to 4D downstream of the rotor, as in the case of closely spaced turbines in a windfarm. The inclusion of both the GAL and GAD parameterizations in WRF provides an ability to better assess the appropriateness of different models and resolutions under an expanded range of atmospheric forcing conditions.

3.7   APPENDIX

GAL formulation and implementation into WRF

The generalized actuator line (GAL) parameterization implemented herein builds on the generalized actuator disk (GAD) parameterization previously implemented into WRF (Mirocha et al., 2014). Both parameterizations follow the generalization of the Blade Element Momentum theory numerically implemented by Mikkelsen (2003), Sørensen et al. (1998), and Madsen (1996), and compute lift and drag forces using aerodynamic properties of the turbine blades based on inflow velocity at the rotor plane, the plane containing the turbine blades (for details see Mirocha et al. (2014)).

The primary difference between the GAD and GAL is that, while the GAD distributes

blade aerodynamic forces over annular elements, the GAL tracks each blade's position in time, and applies aerodynamic forces along lines representing the instantaneous blade locations as those rotate within the disk area. Blade position is tracked via the angle, λ, formed between each blade and the horizon. The forces imparted to the atmosphere by the blades vary in the radial direction only, to account for changing airfoil characteristics along the blade length. The forces are applied to model gridpoints as a function of distance from the blade centerlines (line positions) within a Gaussian envelope. The normal distance dl from each gridcell to the blade position at each model timestep is computed based on λ, the vertical distance between the gridpoint and the hub height (dz), and the normal distance to the axial plane (da), as shown in Fig. 3.20, from

$$dl = \frac{A(da) + B(dz) + C}{\sqrt{A^2 + B^2}} \tag{3.1}$$

.

Here, da is the normal distance from a point to the axial plane, the plane perpendicular to the surface and containing the line normal to the rotor plane and intersecting the turbine axis. By convention, da is positive to the right of the hub and negative to the left viewing the turbine from the upwind direction. dz is the signed difference in height between the grid point and the turbine hub. $A; B; C$ are the coefficients of the equation for the line representing the turbine blade, $Ax + By + C = 0$, and can be determined by treating the hub as the origin of the Cartesian plane on the rotor plane and using λ to determine the slope of the line. When viewed from upwind, equation 3.1 above gives a positive value in the clockwise direction from the line representing the turbine blade, and negative values in the counter-clockwise direction. Equation 3.1 for dl above gives the distance from a point to a continuous line even when the turbine blade, in reality, is not continuous. To account for this, the distance from the grid point to the line perpendicular to the line representing the blade and passing through the hub is calculated, dpl, as shown in Figure 3.20a, with a positive value counter-clockwise from the line and negative value clockwise. Now the forcing along each turbine blade can be implemented in the model by setting the conditions that $dplu$ must be negative and smaller in magnitude than the rotor radius, but larger than the hub radius.

For the GAD, forces are smoothed over several gridpoints normal to the rotor disk to prevent numerical instabilities resulting from large discontinuous forcing. In contrast forces from the GAL are smoothed over three dimensional cylinders surrounding each blade. A Gaussian weighting acceleration term (acc) is used to reduce the magnitude of the force around the blade such that the exact location of the blade (line) is the peak of the Gaussian function:

$$acc = \frac{\exp(-\frac{dr^2}{2\sigma_r^2} + \frac{dl^2}{2\sigma_l^2})}{2\sigma_r\sigma_l\pi} \tag{3.2}$$

where dr is the shortest distance from the grid point to the rotor plane and dl is the shortest distance from the grid point to the plane containing the turbine blade in the axial

direction as discussed above for equation 3.1. σ_r is the standard deviation or spread of the Gaussian in the axial direction (normal to the rotor plane), the same as for the 1-D Gaussian spread for the GAD implementation. σ_l is the standard deviation of the Gaussian within the rotor plane direction away from the line representing the blade.

Once calculations are performed for the first blade, the blade angle λ is increased to the position of the second blade and once the calculation for the third blade finishes, the original λ (for the first blade) is adjusted by using the revolutions per second for the blades and the simulation time-step.

Turbine rotor tilt and offset

In practice, the turbine rotor plane is slightly tilted away from the turbine tower. The tilt of the bottom of the rotor plane away from the tower is typically around 4 degrees. Aitken et al. (2014b) found that adding rotor tilt (Mikkelsen, 2003) to the GAD WRF parameterization causes the vertical location of the wake center to shift upward. This effect is taken into account here by summing the components normal to the rotor disk (found with the tilt angle) from the three velocity components (u, v, w). If tilt is non-zero, a new value for the shortest distance from the grid point to the rotor plane needs to be calculated that accounts for its tilt, drt. This is obtained by using an equation similar to equation 3.1 with the tilt angle, the distance from the rotor plane without tilt (dr), and the height of the grid point compared to the hub (dz). The value for drt is used instead of dr in calculating the acceleration term discussed above in equation 3.2. A new radius from the hub also needs to be calculated due to the tilt. The new radius is calculated using the same shortest distance from the axial plane (da) used with the old radius and a newer version of dz called dzt to account for the newly tilted plane that was horizontal and ran through the hub. This new radius is used to make sure the grid point is within the blade length and that the proper angles, chord lengths, and drag and lift coefficients are calculated. The tilt angle also provides the components of the normal and tangential forces calculated in the x, y, and z directions, resulting in projections of the horizontal forces onto the vertical direction, and vice versa.

Offset of the turbine from the tower is also accounted for. The GAL would most likely utilize resolutions of 1 to 3 meters, in which case for large turbines, the offset is resolvable when using mesh spacings of a few meters or less. This offset is implemented in WRF by adjusting the distances from the rotor plane (dr) by the offset amount in the upstream direction.

Turbine hub and tower parameterization

It may be important to take into account the drag effects of the turbine tower and hub at resolutions relevant to the GAL parameterization (1 to 3 m). These effects are parameterized in a way similar to the GAD parameterization (Aitken et al., 2014b; Wu and Porté-Agel, 2011).

Grid points below the turbine hub and within the radius of the tower are used to parameterize the effects of the tower. The radius of the tower varies linearly from a smaller value at the top to a larger one at the base. The grid point is within this radius if the shortest distance from the point to the axial plane (da) is less than the radius. The force in the normal direction of the tower is calculated using a specified drag coefficient, in this case 1.2, such that $fn = \frac{1}{2}\rho C_t v_0^2$, where C_t is the drag coefficient of the tower, v_0 is the wind speed at the tower, and ρ is the air density. The force is applied over several computational grid points in the direction normal to the rotor plane in the same manner as the GAD with the weighting based on dr.

The turbine hub is parameterized for grid points within the hub center of the turbine so that the radius of the grid point from the hub center is less than the root of the blades. The drag parameterization is implemented identically to the tower parameterization with a coefficient of 1, following Aitken et al. (2014b).

Upstream wind speed

While the gridpoint lift and drag forces obtained within disk or lines are functions of the instantaneous wind speed at that location, three turbine operational parameters, blade pitch, rotation rate, and yaw, require representative wind speed and direction values. These are determined using running time averages of the instantaneous velocity components. The averaging interval and location for these parameters are user specifiable, with default values of two minutes and 1D upstream from the hub center.

Turbulent stresses implementation in WRF

The Smagorinsky LES turbulence closure implemented into WRF (Lilly, 1967; Smagorinsky, 1963) and used for the weakly convective and neutral cases, is given by $\tau_{ij} = -2K_M \tilde{S}_{ij}$, where $K_M = (C_S l)^2 \max(0, |\tilde{S}_{ij}| - P_r^{-1} N^2)$ is the eddy viscosity coefficient for momentum, $C_S = 0.18$ is a constant, $l = (\Delta x \Delta y \Delta z)^{\frac{1}{3}}$ is an isotropic length scale, $\tilde{S}_{ij} = \frac{1}{2}(\frac{\partial \tilde{u}_i}{\partial x_j} + \frac{\partial \tilde{u}_j}{\partial x_i})$ is the resolved strain-rate tensor, $P_r^{-1} = 3$ is the inverse of the turbulent Prandtl number, and N^2 is the Brunt-Vaisala frequency which characterizes atmospheric stability and buoyant suppression of mixing. Tildes denote the resolved or low-pass filtered component of the flow, with $i = 1$, 2, 3 indicating the velocity components in the $u(x)$, $v(y)$, and $w(z)$ directions.

The Smagorinsky closure is also used to prescribe subgrid heat fluxes, given by $u_j' \bar{\theta}_{v,j}' = -2K_q \frac{\partial \tilde{\theta}_v}{\partial x_j}$, where $K_q = P_r^{-1} K_M$.

The subgrid momentum fluxes used for the CWEX-11 simulations are given by the Non-linear Backscatter and Anisotropy (NBA) model (Kosovic, 1997), whose stress tensor is:

$$M_{ij} = -(C_S l)^2 [2(2\tilde{S}_{mn}\tilde{S}_{mn})^{\frac{1}{2}}\tilde{S}_{ij} + C_1(\tilde{S}_{ik}\tilde{S}_{kj} - \frac{1}{3}\tilde{S}_{mn}\tilde{S}_{mn}\delta_{ij}) + C_2(\tilde{S}_{ik}\tilde{R}_{kj} - \tilde{R}_{ik}\tilde{S}_{kj})] \quad (3.3)$$

where $\tilde{S}_{ij} = \frac{1}{2}(\frac{\partial \tilde{u}_i}{\partial x_j} + \frac{\partial \tilde{u}_j}{\partial x_i})$ and $\tilde{R}_{ij} = \frac{1}{2}(\frac{\partial \tilde{u}_i}{\partial x_j} - \frac{\partial \tilde{u}_j}{\partial x_i})$ are the resolved strain-rate and rotation-rate tensors with tildes indicating components of the flow parameter. The model constants are $C_S = (\frac{8(1+C_b)}{27\pi^2})^{\frac{1}{2}}$, $C_1 = C_2 = \frac{960^{\frac{1}{2}} C_b}{7(1+C_b)S_k}$, $C_e = (\frac{8\pi}{27})^{\frac{1}{3}} C_S^{\frac{4}{3}}$, and the skewness parameter, $S_k = 0.5$. Each constant is given as a function of a single parameter, the backscatter coefficient $C_b = 0.36$, and formulated so that proper normal stresses are obtained for sheared homogeneous turbulence. NBA is used for stresses due to better performance during stable conditions, however the heat fluxes use the Smagorinsky formulation.
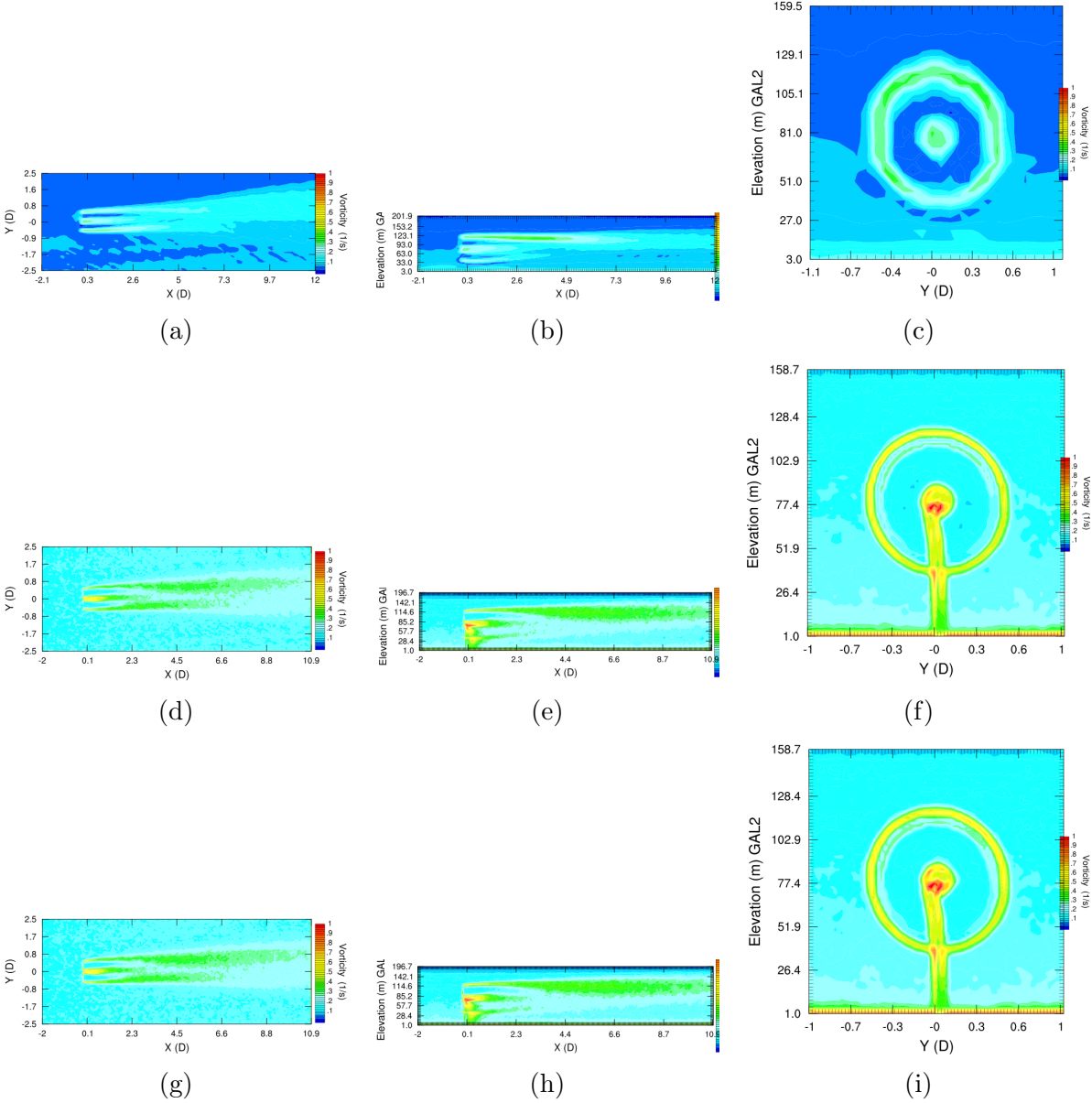
Figure 3.16: Forty five minute averaged magnitude of vorticity contours for GAD-C (a-c), GAD-F (d-f), and GAL-F (g-i) in the x-y (a, d, g), x-z (b, e, h), and y-z (c, f, i) planes at hub height, hub location in y, and 0.2D downstream of hub in x, respectively. These results are for the STA case.
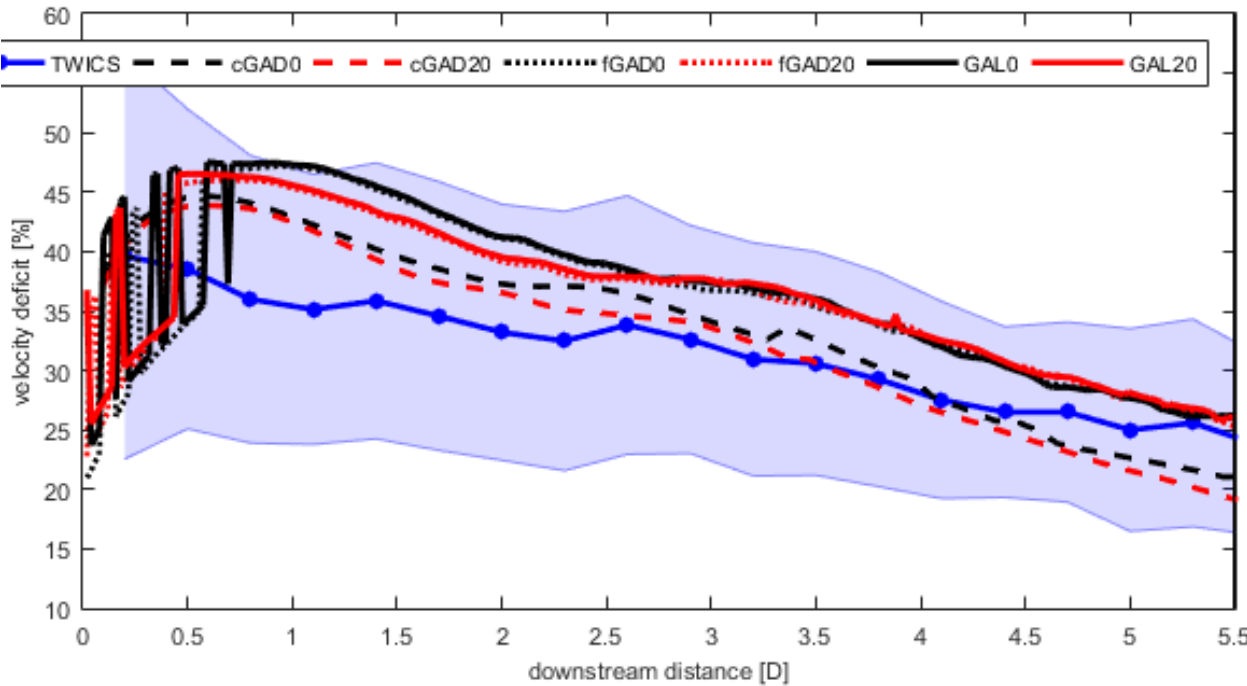
Figure 3.17: VD as a function of downstream distance occurring between 13:00 and 17:10 MST on 22 April, 2011. Median observation values are depicted by the blue, central line whereas the symmetric shaded error bars represent the standard deviation of the measurements. Mean VD values from the LES of CON (red) and NEU conditions (black) are shown for the GAD-C (dashed lines), GAD-F (dotted lines), and GAL-F (solid lines) simulations.
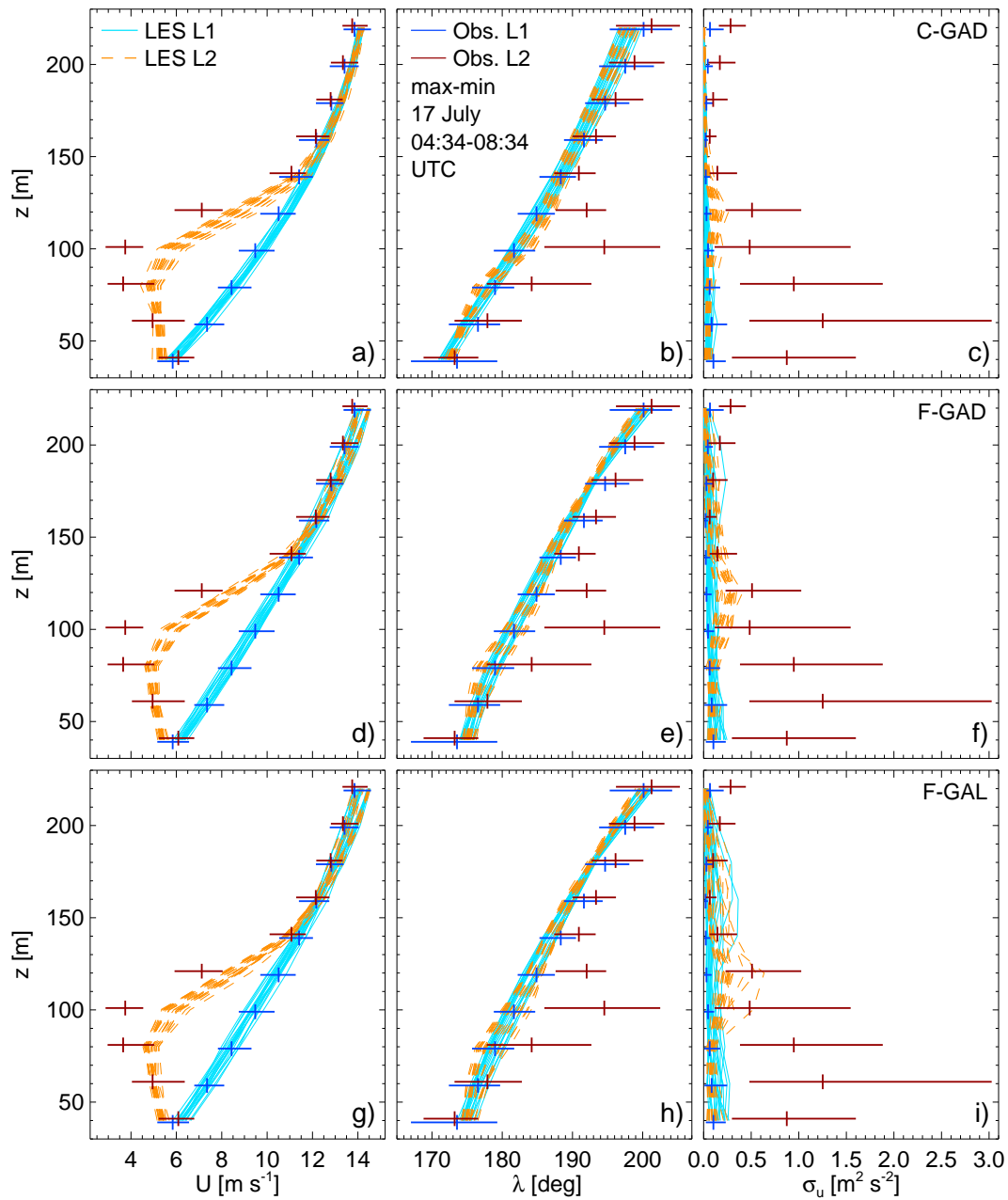
Figure 3.18: 2-minute average profiles of wind speed (a, d, g), wind direction (b, e, h), and variance of u (c, f, i) over 40 minutes of the GAD-C (a, b, c), GAD-F (d, e, f), and GAL-F (g, h, i) STA case for wind direction close to 180 degrees. Light blue and orange are from lidar locations L1 and L2, and horizontal blue and red lines show the observed range of 2-minute average values from L1 and L2, respectively. The vertical hatch indicates the mean of the observation range.
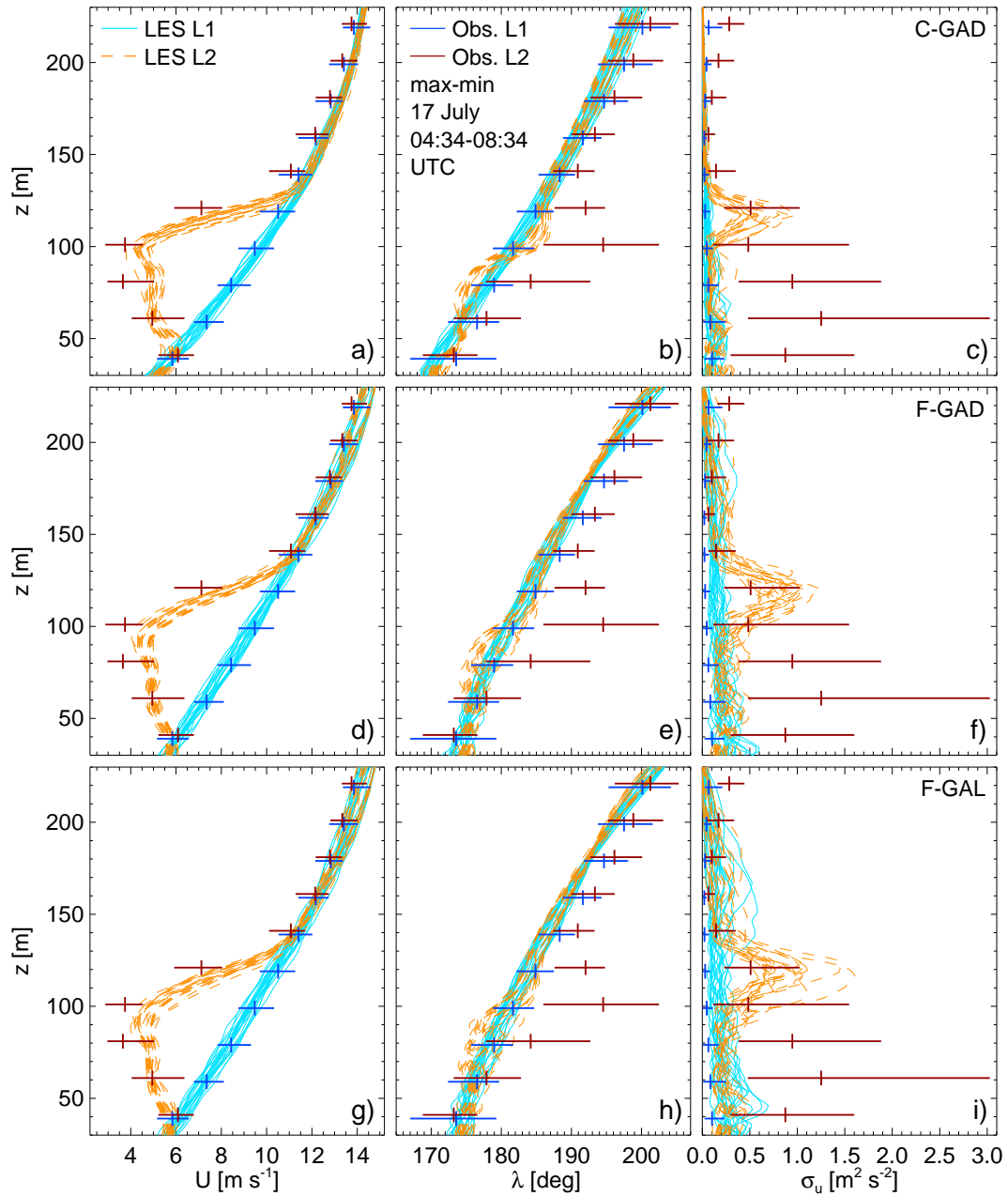
Figure 3.19: As in Fig. 3.18, but interpolated from unweighted values from the simulations' vertical distributions to the lidar range gate heights.
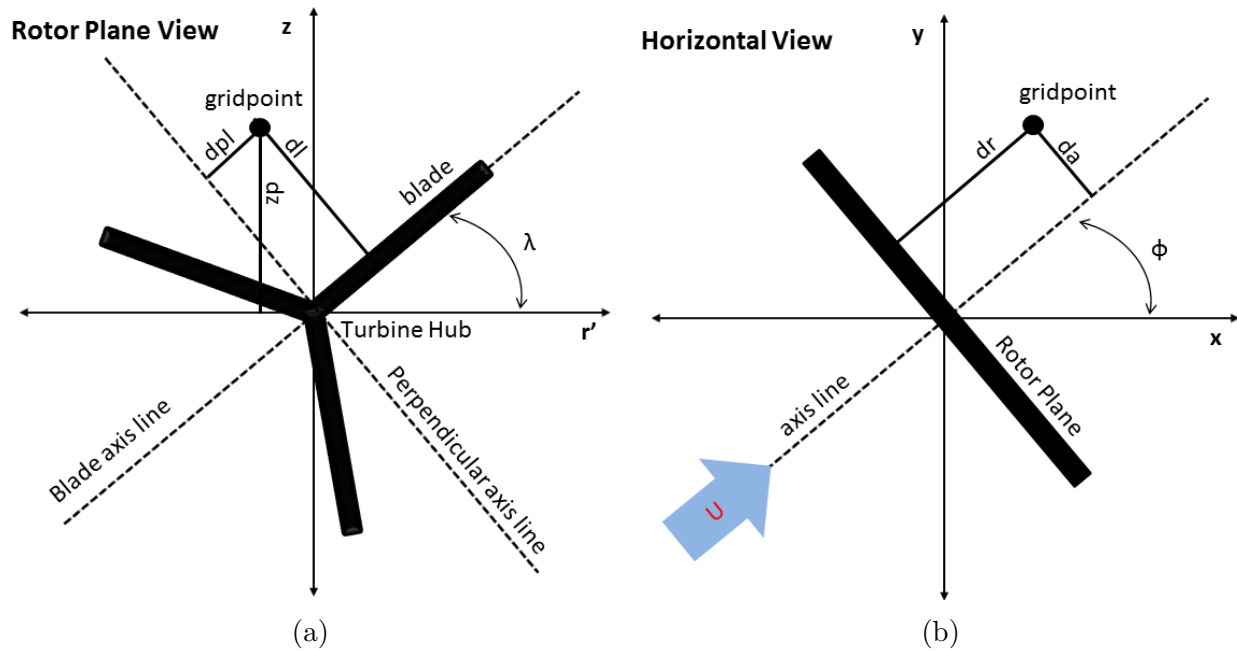
Figure 3.20: Diagram showing implementation of generalized actuator line parameterization in (a) rotor plane view and (b) horizontal view. dl is the shortest distance from a gridpoint to the line representing the blade, dpl is the shortest distance from a gridpoint to the line perpendicular to the blade and intersecting the turbine hub, dz is the height of the gridpoint in relation to the turbine hub, dr is the shortest distance from the grid point to the rotor plane, da is the shortest distance from the grid point to the axial line which is perpendicular to the rotor plane and intersects the turbine hub, λ is the angle a blade makes in relation to the horizontal axis in the rotor plane, r', z is the vertical axis or height, x is the West-East horizontal axis, y is the South-North horizontal axis, and ϕ is the angle (turbine yaw) the axis (axial) line makes with the x axis.

Chapter 4

Mesoscale to LES for a Wind Turbine Array

4.1 Abstract

A mesoscale to microscale nesting strategy is utilized within the Weather Research and Forecasting (WRF) model with a generalized actuator disk (GAD) parameterization to represent wind turbines. The result is a demonstration of how microscale domains with wind turbine parameterizations can be forced with mesoscale simulations capable of simulating real time weather conditions. This grid nesting configuration demonstrates a novel capability to capture interactions between a frontal passage and an operating array of turbines. The simulated wake velocity deficits are compared with measurements obtained from a dual doppler Ka-band radar, which provided quasi-instantaneous snapshots of wake features during the frontal passage. Mesoscale results are assessed using profiles from the wind farm and surrounding sites as well. The mesoscale simulations track the weather features well, and the simulated wakes broadly agree with the measurements. The major weather feature simulated is a ramping event in the form of a frontal passage, and the errors observed appear to be due to the large scale forcing. Simulating the interactions between mesoscale atmospheric features and operating wind turbines within the coupled mesoscale-microscale framework investigated herein can augment existing wind farm computational fluid dynamics tools that do not capture these interactions, thereby providing improved understanding of wake interactions under the range of operating conditions experienced in real world settings, and leading to more efficient turbine array operations and energy capture.

4.2 Introduction

Turbine wake effects are a significant modulator of wind farm performance and reliability due to impacts on downstream turbines, including reduced power and increased fatigue loading (Högström et al., 1988). Low magnitude wind speeds within turbine wakes have

been linked to power losses larger than 40% in downstream turbines (Barthelmie et al., 2010). Increased turbulence intensity in the wakes is implicated in increased fatigue loading of downstream turbines, likely resulting in increased maintenance, downtime, and shorter life spans (Churchfield et al., 2012; Kelley et al., 2005; Magnusson and Smedman, 1999; Thomsen and Sorensen, 1999). Increases in turbulence intensity to greater than 50% of background values have been measured as far as 10 rotor diameters (D) downstream of large turbines (Elliott and Barnard, 1990), and reduced wind speeds from turbine wakes have, in certain cases, been observed to persist at significant levels beyond 10 D (Ammara et al., 2002). These distances are farther than the typical spacing between wind turbines, and therefore underscore the importance of modeling wind turbine wakes with high fidelity to improve turbine micrositing, performance, reliability, and power forecasting. There is a need for the ability to understand how wake characteristics vary under a range of realistic operating conditions, which current CFD tools cannot provide. The absence of a tool capable of providing such predictions motivates the development of a coupled mesocale-microscale framework in combination with high fidelity turbine parameterizations, such as actuator models.

Past large-eddy simulation (LES) studies of the effects of wakes within an array of wind turbines have been utilized for different applications. Calaf et al. (2010) used a suite of LES for a large array of wind turbines parameterized by the classical drag disk concept to quantify the vertical transport of momentum and kinetic energy across the atmospheric boundary layer (ABL). Meyers and Meneveau (2012) made recommendations on optimal turbine spacing for a wind farm with a fully developed ABL using a "drag-disk" parameterization with LES. Other studies (Calaf et al., 2011; Meyers and Meneveau, 2010; Porte-Agel et al., 2011) have also used parameterized arrays of turbines within LES for different applications designed to better understand the complex interactions between wind turbines at a wind farm. These and other studies, however, have used idealized inflow initial and boundary conditions which lack representation of environmental forcing that modulate the significant variability and complexity of real atmospheric flows.

Wind turbine wake formation and evolution are strongly modulated by environmental drivers such as weather events, terrain, and other surface characteristics that affect both the ABL structure and the turbulence field. Mesoscale weather prediction models can represent the drivers that influence atmospheric flow variability, which are not adequately captured by current CFD tools. The mesoscale models use realistic initial and boundary conditions along with realistic representation of important physical processes to improve the simulation of atmospheric flows influenced by a variety of these drivers.

A simulation framework that utilizes high fidelity LES capable of explicitly resolving turbine wake interactions with realistic weather inflow is possible by incorporating mesoscale input into microscale wind farm CFD simulation (e.g. Churchfield et al. (2013), Gopalan et al. (2014), and Zajaczkowski et al. (2011)). An alternative approach is to use a unified simulation framework based on one model capable of internally coupling mesoscale with microscale wind farm simulations. The Weather Research and Forecasting (WRF) (Skamarock et al., 2008) model is used in this work to demonstrate mesoscale-microscale coupled wind farm

simulation capabilities. WRF is selected based on its support of both meso- and microscale simulation, a wide user base, and an active development community that has contributed numerous improvements and capabilities to enhance representation of realistic atmospheric conditions. WRF couples the mesoscale to the microscale simulations with grid nesting, which allows a subset of a computational domain to be resolved at higher resolution while utilizing the lateral boundary conditions from the bounding domain. Grid nesting allows downscaling to sufficiently fine resolution to support LES, which resolves the energetically important scales of turbulence and thus provides a high-fidelity simulation framework for wind farm simulations in turbulent flows. WRF therefore allows incorporation of elements of mesoscale simulations, such as cloud processes, surface physics, atmospheric radiation, and data assimilation into high-resolution LES to more realistically model the physics of wind farm aerodynamics and wake evolution.

Wake simulation requires wind turbine parameterization appropriate to the resolution of the simulation. WRF currently supports wind turbine parameterizations that imposes a momentum sink (based on drag/thrust force) and turbulence kinetic energy source on computational grid cells spanned by the wind turbine's blades (Fitch et al., 2012). This parameterization, however, is not designed to work with LES, but at much coarser resolution. LES, unlike mesoscale simulation, is able to resolve the largest and most energetic turbulent eddies thereby significantly improving the fidelity of wind turbine wake representation. In recent work, an actuator disk parameterization has been implemented into WRF Mirocha et al. (2014). This approach is appropriate for LES and capable of better representing turbine-airflow interactions and wake formation. Thrust and torque (rotation) forces computed at the turbine blades are averaged over a discretized two dimensional disk formed by the rotation of a turbine's blades. A combination of momentum balance in rotating, annular rings intersecting the disk, with lift and drag forces calculated along two-dimensional blade elements (using aerodynamic properties of the blade) is analyzed to compute the forces applied on the atmosphere. The actuator disk parameterization with rotation (includes torque force) has been shown to perform well in representing the far wake (greater than 2 to 4 rotor diameters downstream), especially when compared to the parameterization without rotation (Porte-Agel et al., 2011). Mirocha et al. (2014) and Aitken et al. (2014b) demonstrated that a generalized actuator disk (GAD) parameterization implemented into WRF produces wakes that compare well to observation data at 2 to 6 D downstream. Chapter 3 demonstrated coarse resolution simulations using the GAD produced similar aggregated wake characteristics to both fine-scale GAD and generalized actuator line (GAL) simulations, at a fraction of the computational cost (due to the lower grid resolution). The GAL parameterization only distinguished itself from the GAD parameterization with its capability to better resolve near wake physics (2 to 4 D) which is usually not as important to wind power forecasting or turbine siting as turbines are generally spaced farther apart.

Here, we demonstrate a unified modeling approach that internally couples mesoscale to microscale LES capabilities with the GAD parameterization to study turbine-wake interactions for an array of wind turbines during a frontal passage. We further modify the GAD parameterization implemented into WRF by Mirocha et al. (2014) and modified in Chapter

3 to allow for simulation of realistic wind turbine operations such as yawing with the wind direction, turbine cut-in/out control, and utilization of real terrain data (see appendix section 4.8 for details of modifications). This framework is verified here against profiles from surrounding sites as well as measurements from a dual doppler radar that provided snapshots of wake features during a frontal passage (Hirth et al., 2015).

4.3 Case Study and Observations

The array of wind turbines simulated in this work are chosen due to the availability of dual-doppler measurements of a wind ramp event at a utility-scale wind farm in Oklahoma (Hirth et al., 2015). This is, to date, the only observational case study of a wind ramp event spanning the footprint of a large turbine array as there are a limited number of remote sensing technologies capable of providing the necessary spatial and temporal data coverage that have had the fortune to be deployed during a ramping event.

Two mobile Ka-band research doppler radars were deployed at the wind farm on 21 November 2013. The deployment collected remotely sensed measurements of the wake and complex flows over a large three-dimensional domain encompassing a section of the turbine array in the horizontal and a vertical depth through the turbines' rotor sweep (see Hirth et al. (2015) for a more details on the radar deployment). Figure 4.1 shows a schematic with radar deployments, turbine locations, the dual-doppler radar analysis domain, and the terrain elevation. The dual-doppler analysis domain captured 32 operational turbines with a hub height of 80 m and a rotor diameter of 82.5 m. A cold frontal passage and accompanying wind ramp appear in the dual-doppler domain from the North-West at 15:35 UTC as the wind direction shifts from North-East to North and is accompanied by a small increase in incoming hub-height wind speed from 6 m s^{-1} to 8 m s^{-1}. A wind speed surge follows at around 15:42 UTC, when incoming wind speeds increase to 15 m s^{-1} and produce stronger wakes behind the front row of turbines (see figure 5 from Hirth et al. (2015)).

4.4 Numerical setup

Grid nesting

Five nested grids are used to downscale the mesoscale flow to simulate flow conditions for the turbine arrays at horizontal resolutions of 6.25 km to 10 m at a 1:5 grid nesting ratio. Topography and land-use data are extracted from a 0.9 km resolution data set, and terrain is smoothed near the boundary for each nested sub-domain to match the elevations for the surrounding coarser grid. A higher resolution land surface data set is deemed unnecessary due to the simple flat terrain and homogeneous aggregate land-use in the area of the wind farm (Marjanovic et al., 2014). WRF uses a terrain-following, hydrostatic-pressure vertical coordinate system with the top of the model being a constant pressure surface. The vertical grid spacing is specified at 10 m above ground for the first point above the surface and
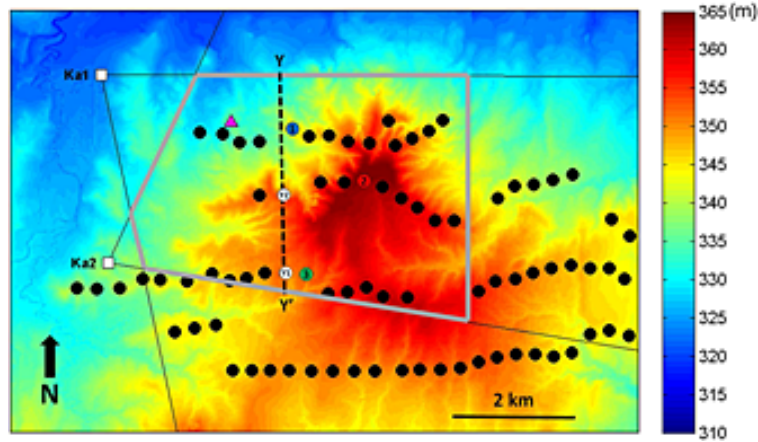
Figure 4.1: Map of mean sea level elevation (m) overlaid by dual radar deployment (Ka1 and Ka2 white squares) within the wind plant. Turbine locations are represented by black dots and the dual-doppler analysis domain is represented by the thick gray lines. The magenta triangle shows the location of a meteorological tower. (Hirth et al., 2015)

is slowly stretched to a higher value for each successive grid point above. The stretching rate follows a smooth *tanh* function that increases farther away from the ground surface, but never exceeds the previous spacing by more than 10 %. Relevant simulation parameters, such as domain dimensions, for each grid configuration are shown in table 4.1. The simulations are computationally expensive with the finest resolution (10 m) domain consisting of 650 by 550 by 177 grid points with a time step of 0.04 s. The domain height is approximately 16 km. The domains are selected so as to avoid any significant regions of steep terrain within or near the boundaries (such as the Rocky Mountains), and to allow the greatest fetch from the North and West, the direction from which the frontal passage emerges. The finest domain (with the wind turbine parameterization) contains a subset of the dual-doppler analysis domain (shown in figure 4.1). The northernmost row of wind turbines is in the middle of the domain to allow enough fetch from the North, and the southernmost (third row of turbines) is excluded due to its large distance away from the Northern turbines.

Initialization and lateral boundary conditions

Initial and boundary conditions are obtained from the National Centers for Environmental Prediction (NCEP) North American Mesoscale Forecast System (NAM) data. NAM is available at 12 km horizontal resolution and at 26 pressure levels (1000-50hPa; excluding surface) to force WRF simulations at the coarsest grid. Lateral boundary condition forcing is applied at six-hour intervals and linearly interpolated in between. Relaxation towards the lateral boundary values was applied around the edge of the domain. The three outer domains (6.25 km to 250 m) were initialized at 0 UTC (or approximately 15.5 hours before the cold front). The two inner LES domains initialize at 15 UTC with the GAD parameterization in

the innermost domain.

Other input data are also investigated to improve model agreement with surface observations (see section 4.5). The North American Regional Reanalysis (NARR) data is chosen due to its higher temporal resolution (three hour) than NAM (six hour). NARR is available at 32 km resolution horizontally and at 29 vertical levels. The NCEP Rapid Update Cycle (RUC) data is also attractive for its high temporal (1 hour) and spatial (13 km) resolution and is tested below.

Surface characteristics

WRF uses 33 land use categories (including ice and water) from USGS. The Noah Land Surface Model is utilized with initial moisture and soil temperature in four layers interpolated from NAM. The same is true for the runs using NARR. The RUC input is used with both the Noah Land Surface Model and the RUC Land Surface Model, which uses the RUC operational scheme with soil temperature and moisture in six layers.

Turbulence

WRF provides several boundary-layer turbulence parameterizations for mesoscale simulation. For this study, the three outer domains (6.25 km to 250 m) use the Mellor-Yamada-Janjic (MYJ) scheme Janjic (1994), which uses a prognostic turbulence kinetic energy (TKE) equation to predict the sub-grid TKE and a diagnosed length scale to obtain the vertical eddy viscosity. The 250 m resolution domain is in the gray zone for choice of turbulence parameterization (Wyngaard, 2004). Prior experience shows 250 m resolution is not always adequate for LES (Marjanovic et al., 2014), especially for a stable boundary layer with a thickness that is usually less than 1 km. The two inner nested domains (50 m and 10 m) use the TKE1.5 LES closure, which also uses a prognostic TKE equation to model sub-grid scale turbulence, but with a length scale directly related to the grid spacing.

Wind turbine parameterization

Following Mirocha et al. (2014) and Chapter 3, the generalized actuator disk (GAD) parameterization is utilized at the finest resolution domain (10 m), which is able to resolve the actuator disk with at least eight grid points along its diameter. Modifications are made to the WRF GAD parameterization beyond what is described in the last chapter to enable use in more realistic and variable environmental conditions. Greater detail on these changes, such as turbine yawing (rotation) and real terrain implementation, is presented in the appendix of this chapter (section 4.8). Aerodynamic properties for the 29 parameterized turbines are integrated for computation of forces on their blades. The aerodynamic properties take the form of look-up tables that provide lift and drag coefficients, turbine rotation rate, and blade twist based on location along the blade and incoming or upwind velocity. Each turbine has a hub height of 80 m, a rotor diameter of 82.5 m, a cut-in wind speed of 2.5 m s^{-1}, and

a cut-out speed of 25 m s^{-1}. The three outer "mesocale" domains (6250, 1250, and 250 m horizontal resolutions) are initialized at 0 UTC and spun up to 15 UTC, when the two inner "microscale" LES domains (50 and 10 m horizontal resolution) are introduced. This set-up allows enough spin-up time (about 20 min) for the LES domains, including the innermost domain with the GAD parameterizations, to capture conditions before and during the frontal passage along with the wind speed surge that follows a few minutes later. Simulation output is stored at 10 minute intervals for the outer mesoscale domains and at 1 minute intervals for the inner microscale domains.

4.5   Mesoscale validation with surrounding sites

The mesoscale simulations are first validated with multiple sources of observation data (such as wind speed, direction, and temperature) in the vicinity of the turbine arrays. These include a North meteorological (met) tower just North of the turbine array shown by the magenta triangle in figure 4.1 and another South tower farther to the South-East in the wind farm and not in the domain of the figure. Data is also available from a vertically profiling lidar next to the South met tower. Comparisons are made to sources farther outside the wind farm and include a vertical profiler North-East of the wind farm, a radiosonde profile North of the farm, and two surface stations (one North and one South of the wind farm). For brevity, only comparisons to the closest data source, the North met tower, are shown hereafter, as similar conclusions are drawn from all the other observations.

Comparisons of the finest mesoscale domain (250 m horizontal resolution) for the different input (NAM, RUC, and NARR) data discussed in section 4.4 are shown against observation data at the North met tower as a time series by figure 4.2. The RUC forced simulations, given RUC's high temporal and spatial resolution, perform unexpectedly poorly when compared to met tower observations, as they completely misrepresent the wind speed for the ramping event at approximately 15:30 UTC. This example demonstrates the importance of quality mesoscale input forcing data to simulation results. While NARR and NAM forced simulations follow similar trends compared to observations, NAM more accurately compares to the observations particularly at times around the ramping event.

To attempt to improve the mesoscale forcing even more, additional mesoscale simulations are performed using analysis nudging and compared to observations at the North met tower. Analysis nudging is a numerical tool that in essence forces (nudges) simulation results at each grid point closer to a value that is time-interpolated from analyses data. Figure 4.3 compares analysis-nudged RUC and NAM simulations to their simulations without nudging and to the observations at the North met tower. The nudged RUC simulation does not show significant improvement over RUC without nudging, thus further eliminating the possibility to use RUC to force the microscale GAD simulations. The nudged NAM simulation (NAM-N) shows stronger wind speeds than the NAM simulation without nudging, and compares better to the observations. NAM-N is also able to better capture the frontal cooling event shown by the observations in figure 4.3c, however, it compares worse with wind direction

observations before and during the ramping event. The mesoscale simulations forced with NAM and NAM-N both capture the features associated with the frontal passage and are used to force the fine scale domains.

4.6 GAD parameterized LES of the turbine array

The wind turbine array is simulated with the GAD parameterization and NAM forcing both with and without analysis nudging, due to neither displaying a clear advantage as discussed in the previous section. Figure 4.4 displays instantaneous horizontal hub height wind speed for the turbine array comparing the dual-doppler (DD) synthesized observations (figures 4.4a-4.4c), NAM forced microscale GAD simulations (figures 4.4d-4.4f), and NAM forced GAD simulations with analysis nudging (NAM-N) (figures 4.4g-4.4i). The first column (figures 4.4 a, d, g) shows the cold front as it approaches the array from the North-West, the second column (figures 4.4 b, e, h) shows the front passing between the first two rows of turbines, and the last column (figures 4.4 c, f, i) shows the surge of wind speed following 5 minutes after the front. The simulations display the front arriving approximately 8 to 9 minutes later than for the observations, and the rest of the simulated frontal features are delayed accordingly (except for temperature in the time series above). The NAM forced simulation without nudging is able to replicate the wind direction from the observations very well, while the NAM forced simulation with nudging does not include a strongly defined frontal passage or winds directly from the North close to the time they are shown in observations. Both simulations display wind speeds approximately 2 m s^{-1} weaker than observations (see figure 4.4). Neither simulation shows a strong surge similar to the observed, however, the simulation with nudging does display a weaker surge (by approximately 5 m s^{-1}). The nudged simulation shows a strong surge with wind speeds up to 15 m s^{-1} at approximately 16:12 UTC (not shown). The simulation forced without nudging displays turbine wake extent and interactions/behavior similar to the observations, and wind speed deficit in the wakes is also similar and approximately 3-4 m s^{-1}.

4.7 Conclusion

A mesoscale to microscale nesting strategy for a real wind farm was demonstrated for the first time within a unified model, the Weather Research and Forecasting model, with a generalized actuator disk (GAD) parameterization. Mesoscale simulations capable of simulating realtime weather conditions forced microscale domains with wind turbine parameterizations that captured interactions between a frontal passage and an operating array of wind turbines. The GAD, already implemented into WRF, was modified to allow simulation of industry practices/procedures, such as turbine yawing with the wind, during real time weather conditions. Other additions to the parameterization included turbine cut-in/out control, and utilization of real terrain data. The nesting strategy is herein assessed by comparison with

surface-based observations in the vicinity of the wind farm and from dual-doppler Ka radar (Hirth et al., 2015), which provided quasi-instantaneous snapshots of wake features during the frontal passage. The ability of different mesoscale forcing data to capture important characteristics of the frontal passage were also investigated.

RUC input data, despite its high temporal and spatial resolution compared to other input data, did not capture any features of the frontal passage including its associated wind speed ramping, whereas NAM input data captured the general trends during the ramping event. Analysis nudging was used for the different forcing data sets but did not improve wind results when compared to observations. The quality of synoptic forcing data is of great importance in capturing events like a frontal passage and may vary significantly for different input data sets (Marjanovic et al., 2014).

Microscale domains with the GAD parameterization captured the ramping event with simulated wind directions similar to the observations, however the magnitude of wind was under-estimated especially during the surge that followed the initial cold front. The length and interaction of the wakes along with the wind deficit were similar to observations, suggesting that the model framework may prove promising with better quality forcing data.

Simulating interactions between mesoscale atmospheric features and operating wind turbines within a coupled mesoscale-microscale framework with explicit turbine drag and rotation representations can augment existing wind farm CFD tools that do not capture these interactions. CFD models generally use more efficient grid meshing and are therefore the only practical models for sub-meter resolution simulations of wind turbine components or very large arrays of actuator line parameterizations. For many applications, however, disk models provide satisfactory fidelity and a unified mesoscale model is preferable for the seamlessness and simplicity it can provide for wind farm operations. With such simulations, wake interactions under the range of operating conditions experienced in real world settings can be better understood, leading to more efficient array operations and energy capture.

4.8 APPENDIX

Turbine yaw implementation

Wind turbine yaw is the rotation of the wind turbine hub and blades into the direction of the incoming wind. An algorithm is implemented in the WRF model to yaw each turbine according to common operational practices. The angle, ϕ, determines the orientation of the turbine with respect to the cardinal directions (e.g. East or West). Wind direction is determined instantaneously at the same location as the upstream wind speed, used to calculate the pitch and angular velocity of the blades, and is communicated to the other processors. The raw yaw error is calculated as the difference between ϕ and the wind direction. Yaw error accumulation is computed as a function of the squared raw yaw error, the time step, and the sign or direction of the error. The accumulated yaw error is added to that of the previous time step and stored for each individual turbine. The raw yaw errors are

saved in a variable for each time step to be averaged later if the turbine needs to yaw. The yaw algorithm does not record yaw error or its accumulation through time if the turbine is already in the process of yawing or the wind speed is below cut-in or above cut-out speed. Instead, the recorded and accumulated yaw errors are reset during these periods.

When the accumulated yaw error exceeds a user defined threshold (e.g. in this chapter the turbine yaws after 10 minutes if the average yaw error is 10 degrees; more time for smaller error and less for a larger error), the turbine yaws to the proper position. This position is determined by averaging the stored raw yaw errors to obtain an average yaw error. ϕ is adjusted by a user specified yaw speed (usually one degree per second) for each time step until the desired orientation is achieved, after which the turbine yawing stops and the tracking of yaw accumulation and error is reset.

Computation of the upstream wind speed and direction, discussed in the appendix of the previous chapter, did not take turbine yaw into account. This is remedied by utilizing the orientation angle of the turbine, ϕ, to obtain the slope of the line, in the horizontal plane at hub height, normal to the rotor plane passing through the hub. The point closest to the desired distance away from the hub along the line can then be used as the upwind location. This computation is only performed initially and every time the turbine is in the process of yawing.

Miscellaneous improvements to the GAD parameterization

The model is improved from its implementation by Mirocha et al. (2014) by reduction of computations performed. All static variables are computed at only the first time step and stored thereafter. They are only recomputed when needed, for instance during yawing or simulation restarts. Variables with a vertical component are recomputed for each time step, as the vertical coordinates in WRF are not static. The grid points around the turbine for which calculations are performed are limited to a smaller region instead of the entire domain (e.g. one rotor diameter around the hub), thereby conserving computational resources to only the area of significant impact on the turbine. This is particularly beneficial in the case of multiple wind turbines on a single domain. The ability to simulate over real terrain is added to enable more realistic representation of atmospheric boundary layer flow. An algorithm to read a user-specified input file with turbine characteristics and locations is another addition.

$\triangle h$ (m)	(nx,ny,nz)	$\triangle t$ (s)	Turbulence Closure Scheme	Simulation Start Time (UTC)
6250	(200,200,177)	15	MYJ	0
1250	(200,200,177)	5	MYJ	0
250	(200,300,177)	1	MYJ	0
50	(400,500,177)	0.2	TKE1.5 LES	15
10	(650,550,177)	0.04	TKE1.5 LES	15

Table 4.1: Simulation parameters for each grid resolution.
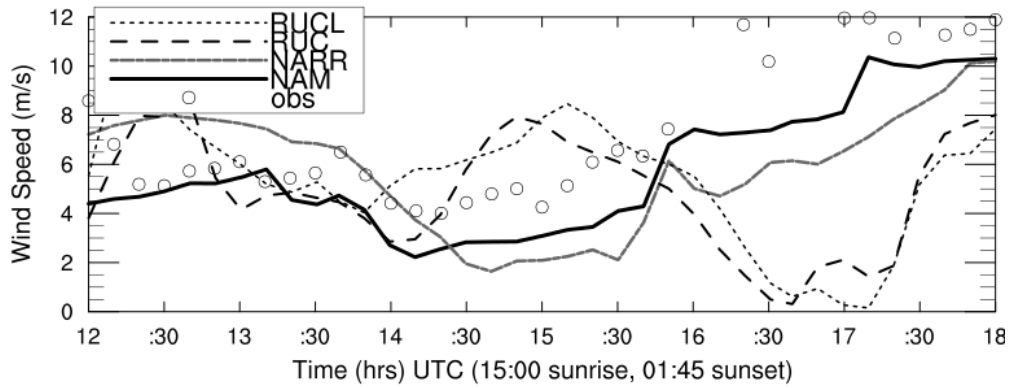
(a) Wind Speed
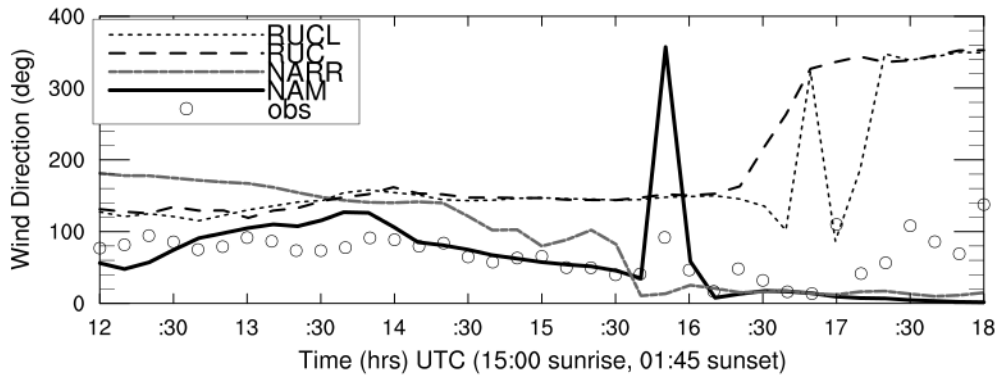
(b) Wind Direction
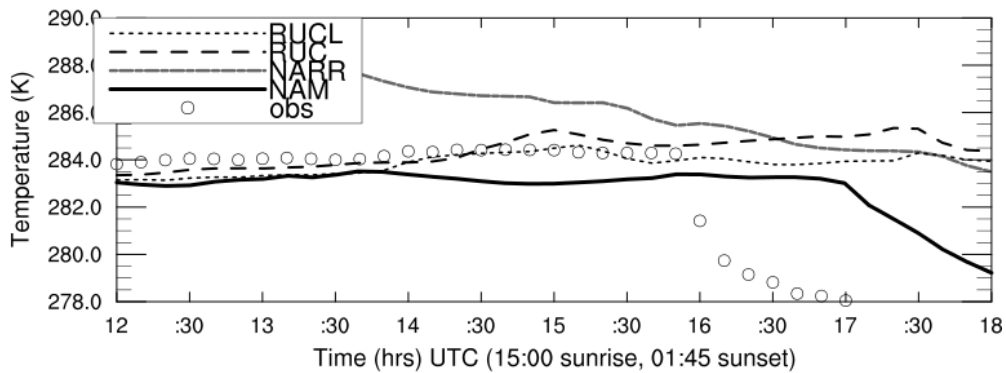
(c) Temperature

Figure 4.2: Horizontal wind speed, direction, and temperature 6 hour simulation time series input data comparisons (at 250 m horizontal resolution) to North met tower observations at 80 m hub height. Input data are for RUC, NARR, NAM, and RUCL which is RUC using the RUC land surface model.
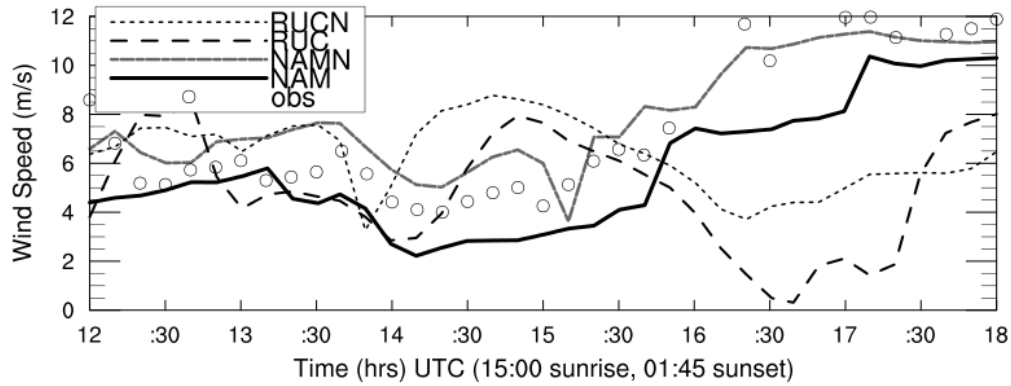
(a) Wind Speed
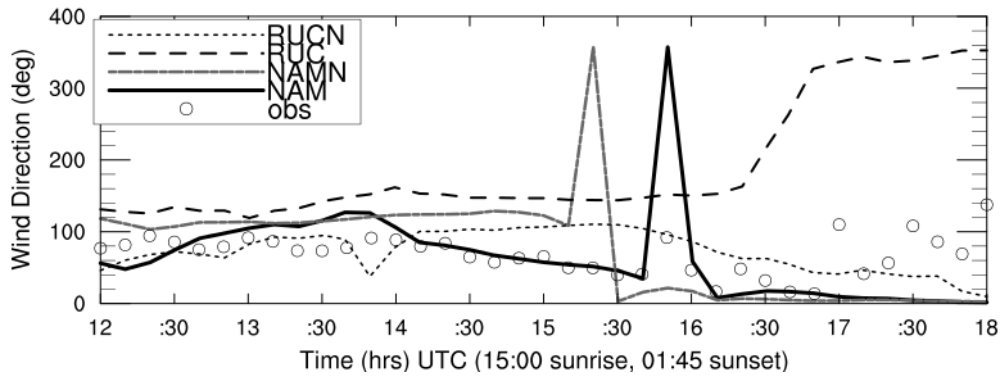
(b) Wind Direction
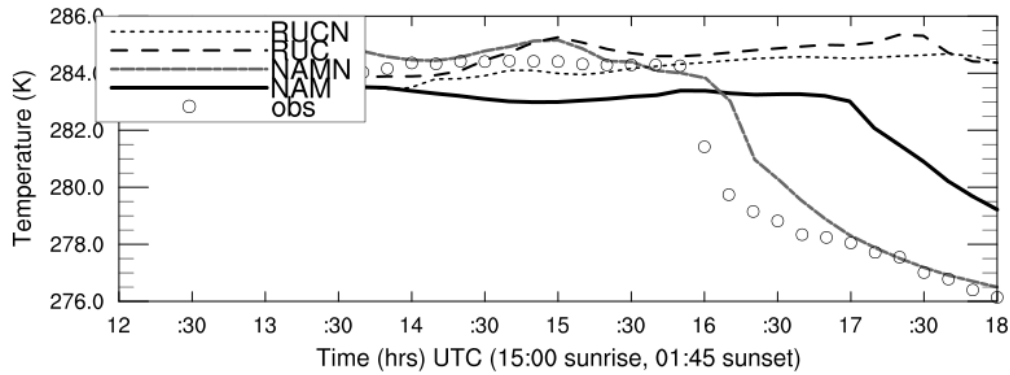
(c) Temperature

Figure 4.3: Horizontal wind speed, direction, and temperature 6 hour time series input data (at 250 m horizontal resolution) comparisons to North met tower observations at 80 m hub height. Simulation results are for RUC, RUC nudged (RUCN), NAM, and NAM nudged (NAMN).

(a) 15:35 UTC DD   (b) 15:41 UTC DD   (c) 15:46 UTC DD

(d) 15:43 UTC NAM   (e) 15:48 UTC NAM   (f) 15:53 UTC NAM

(g) 15:44 UTC NAM-N   (h) 15:50 UTC NAM-N   (i) 15:55 UTC NAM-N
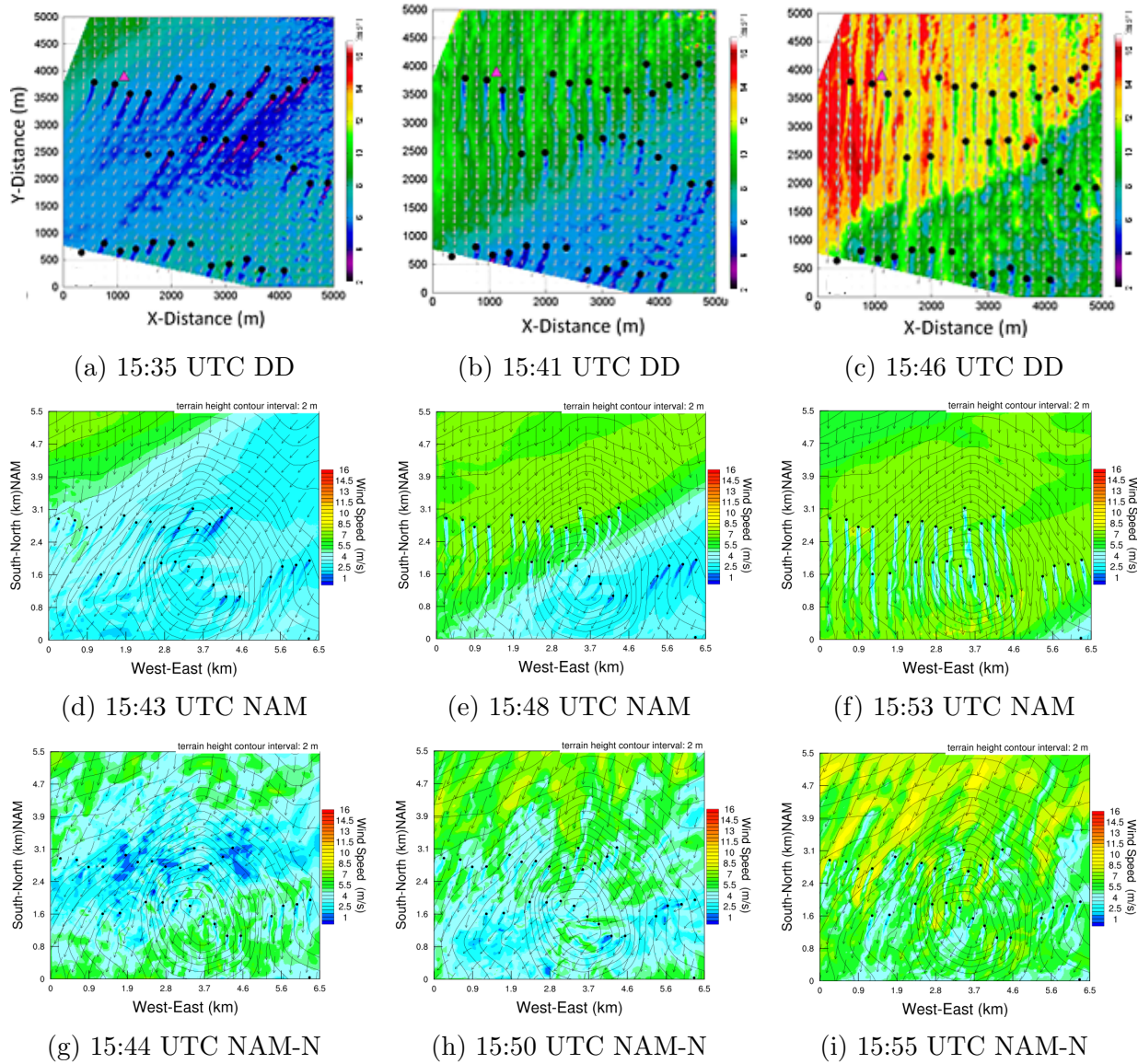
Figure 4.4: Instantaneous contours of turbine array wind speed at hub height for the dual-doppler (DD) synthesis (a-c) (Hirth et al., 2015), NAM forced GAD LES (NAM) (d-f), and NAM forced GAD LES with analysis nudging (NAM-N) (g-i). The black dots represent the location of the turbines.

Chapter 5

Summary and Recommendations

5.1 Summary

This dissertation contributes to the development of a unified computational framework capable of realistically representing atmospheric physics and dynamics spanning meso and micro scales, important to many wind energy applications. The ability to simulate wind farm operations under variable weather conditions is currently limited by the absence of representation of weather effects in wind farm computational fluid dynamics (CFD) tools. Benefits of modeling turbine and wind plant inflow, as well as turbine airflow interactions, at increased fidelity, will lead to improvements in turbine micrositing, performance and reliability, and power forecasting. A significant need is improved understanding of how wake effects vary under a range of realistic operating conditions, including atmospheric stability and mesoscale processes, which current CFD tools cannot simulate at the required fidelity. This and similar needs motivates the development of a coupled mesocale-microscale framework, integrating realistic atmospheric inflow with actuator models to represent airflow turbine interactions, and wake formation and evolution processes.

The dissertation investigates the importance of simulation configuration options, such as grid resolution and turbulence closure, in mesoscale numerical simulations for very different weather and land-surface conditions. The effect of these choices on wind dynamics relevant to the power industry is explored. Recommendations for various wind energy applications are then given, weighing simulation performance improvements relative to computational cost. Wind turbine parameterizations appropriate for microscale or large-eddy simulation (LES) are developed, compared, and evaluated. The Weather Research and Forecasting (WRF) model is used herein due to its wide user base, active development community, and support of both mesoscale and microscale simulation. Actuator turbine models are also implemented and evaluated in relevant wind energy contexts. Finally, the unified simulation framework with wind turbine parameterization capabilities is demonstrated to be able to model complex atmospheric-turbine wakes for a real wind farm during synoptic weather conditions.

WRF is used in Chapter 2 to evaluate the impact of model resolution and configuration

choices on representation of mesoscale flow at two wind farm sites with varying terrain complexity. The case studies investigate both synoptically and locally-driven weather events at each site, while also including ramping events relevant to the wind industry. Observations are used to evaluate the performance of simulations conducted with different grid resolutions, turbulence closures, and nesting configurations. It was found that simulation improvements with increasing resolution were strongly dependent upon both the nature of the forcing and the complexity of the underlying terrain. Simulation results did not improve significantly with higher grid resolution for the simple terrain site, however, there was marked improvement with increased resolution for the complex terrain site. This improvement was only during the locally-forced event. Consequently, computational resources could be conserved if the topography is adequately resolved at coarser resolution and/or during strong synoptic forcing. Other parameters and configuration choices, such as soil moisture and the two-way nesting option, which provides feedback from the nested to the parent domain, have a more significant effect on simulation results for the locally-forced events. The planetary boundary layer (PBL) turbulence closure scheme can significantly impact simulated atmospheric dynamics, and no scheme simulated results closest to the observations for all the cases. The prognostic turbulence kinetic energy (TKE) equation schemes, however, gave results that, in general, more accurately compared to the observations.

In Chapter 3, a generalized actuator line (GAL) wind turbine parameterization is implemented into WRF with the purpose of enabling higher fidelity LES of turbine interactions with realistic atmospheric boundary layer (ABL) conditions. The GAL is evaluated against a previously implemented generalized actuator disk (GAD) parameterization and measurements from two field campaigns, each of which measured the near-wake regions of a single turbine and allow for comparison during weakly convective and stable conditions, respectively. The GAL parameterization applies thrust and tangential forces on the atmosphere along resolved lines representing the locations of a wind turbine's blades, while the GAD distributes these forces over a resolved disk created by the rotation of the blades. Similar aggregated wake characteristics are produced by the GAD and GAL for both stability classes, thus verifying proper implementation of the GAL. Each parameterization is compared by its ability to represent wake wind speed, variance, and vorticity distributions at the same fine grid resolution. The GAD is also compared at a coarser grid resolution only capable of resolving the actuator disk and not the turbine blade. The coarse-resolution GAD simulation shows similar results overall, with slightly smaller and less persistent velocity deficits, but substantially less variance and vorticity in the wake when compared to the finer-resolution GAD and GAL simulations. The GAL distinguishes itself from the fine-resolution GAD via distinct tip and root vortices, which maintain coherence as helical tubes for about one rotor diameter downstream. The differences between line and disk vorticity structure disappears at distances greater than approximately 2 rotor diameters downstream.

Chapter 4 implements a unified WRF meso- to microscale real-world computational framework for an array of wind turbines at a utility-scale wind farm. Simulations are able to capture impacts of a mesoscale frontal passage interacting with an operating wind farm for the first time. Mesoscale simulation results are compared using different input data

and show the quality of forcing data is of utmost importance for realistic representation of weather events. The GAD parameterization initially used for ideal simulations is modified to function in a real simulation by making use of real terrain input, responding to operational cut-in and cut-out wind speeds, and obtaining the ability to yaw into the wind by utilizing an algorithm designed to replicate real turbine motion. Simulation results are compared to dual-Doppler measurements that provide three-dimensional fields of horizontal wind speed and direction. The model framework is able to produce realistic turbine wake effects, while differences with measurements can largely be attributed to the quality of the available weather and input/boundary data.

5.2   Recommendations

Best practices in modeling for the wind energy industry and areas for future research can be recommended based on the findings in this dissertation.

The mesoscale simulation results from Chapter 2 show there is no "one size fits all" simulation set-up for wind energy applications. Rather the results suggest that simulation set-up is very site and weather dependent. When a wind farm is (or is to be) located in an area with very simple topography, the results in Chapter 2 showed that it may be unnecessary to perform costly high-resolution simulations to obtain more accurate forecasts for wind speed or ramping at the wind farm. This could apply to wind farms located, for example, in the North American Great Plains region where the influence of topography on the large-scale flow is minimal. Over complex terrain, in contrast, high resolution is critical for resolving the underlying topography for locally forced conditions. Strong synoptic forcing, such as a frontal passage, may overshadow the effects of topography. It is important to consider any complex topography, such as mountainous or very hilly terrain, in the close vicinity (on the order of a few kilometers) of the wind farm, especially if located upstream of the expected incoming wind direction.

When there is complex terrain at or near a wind farm that could impact or disturb wind flow, more computationally expensive high resolution simulations should be considered. Examples include wind turbines a few kilometers downwind of mountainous terrain, close to or within gorges, or sited along ridges, cliffs, or very hilly terrain. This recommendation for high resolution would also apply to surface conditions, such as changes in land-use or heat capacity, as well. Wind farm operations may need to consider high resolution simulations when high resolution land-use data is available and the wind farm is located in a diverse land-use area, regardless of topography, such as close to an urban development or forest. Properly resolving these areas may significantly impact wind simulation results. If, however, the wind farm is located in a uniform area, such as a cornfield, which spans tens of kilometers in all directions, computationally expensive high resolution simulation may not be needed.

Computational resources may potentially be spared in certain situations even for wind farms with complex terrain or land-use during strongly forced synoptic weather events. Wind energy forecasters should be aware of the potential to save computational resources for time

periods during which strong synoptic events such as frontal passages are predicted by coarse resolution weather simulations, however, this is site dependent. The importance of physical parameters such as topography, soil moisture, and land-use can potentially be overshadowed by strong synoptic forcing conditions as chapter 2 showed. Hence, this dissertation's results suggest that computationally expensive high-resolution mesoscale simulations may only be needed for complex terrain or land-use situations forced by weak local weather conditions.

Other mesoscale simulation parameters such as the PBL scheme and input data may influence mesoscale simulation results. Different PBL schemes in WRF could be tested for the specific wind farm site for various situations such as weather forcing and stability conditions, because no single PBL scheme is ideal for every situation. The model forcing input and boundary condition data are fundamentally important for accurate simulation results, and the different available data-sets should be compared as one may easily misrepresent important synoptic conditions as chapter 2 demonstrated.

The mesoscale simulations presented in chapter 2 leave several modeling parameters unexplored for the two case studies. These include the different land-surface model options in WRF or the different moisture parameterizations. These are likely to have stronger influence for locally forced cases. The two case studies from chapter 2 are located in very different terrain complexity; in order to develop more specific guidelines for when to use high resolution simulations, more case studies over varying terrain, land-use, and weather conditions need to be assessed. Access to many different wind farm data sets would be necessary for this undertaking, which may prove challenging due to the proprietary nature of the wind energy industry.

High resolution LES should be considered by wind farm operators in cases where accurate representation of turbulence intensity and characteristics of wakes not obtainable from mesoscale simulations using mesoscale wind farm parameterizations. As chapter 3 showed, high resolution LES significantly improves representation of turbulence which may be useful for site assessment or scheduling turbine maintenance/downtime. The GAD and GAL parameterizations may be utilized in simulations at a wind farm with mesoscale weather input, as chapter 4 demonstrated. The GAD parameterization is currently the most computationally efficient high fidelity turbine parameterization to simulate an array of wind turbines within LES due to a lower grid resolution requirement compared to the GAL. Chapter 3 showed coarser resolution GAD simulations produced similar aggregated wake characteristics to both fine-scale GAD and GAL simulations and would be adequate for wind speed deficit estimates used for power forecasting. It is thus recommended that the GAD parameterization at coarser resolution be used to conserve computational resources if the user is only interested in wind speed and the far wake (greater than 2-4 rotor diameters downstream). The finer resolution GAL parameterization, however, should be used when the near wake and greater resolution of vorticity or turbulence are of interest as vorticity shedding and wake expansion are better represented.

As mentioned in chapters 3 and 4, a mesocale wind turbine parameterization currently exists in WRF and can be used with PBL schemes utilizing prognostic TKE. A quantitative comparison between the mesoscale turbine parameterization and a higher resolution LES

with a GAD and/or GAL parameterization for the same area would benefit operators by providing guidelines on when less computationally intensive mesoscale simulations may be useful to provide the necessary information for a given application. An example would be forecasts of wind speed deficits at a wind turbine downstream from another turbine.

Chapter 4 presented a unified mesoscale-microscale coupling strategy from mesoscale to LES. Transitioning from mesoscale to LES can present several challenges which may be better addressed by different nesting strategies. Chapter 4 uses a large physical distance/fetch and over 100 grid points upstream of the first row of wind turbines to allow for resolved turbulence to develop by the time the flow reaches the turbines. The LES boundary conditions are nested from the coarser mesocale simulation which uses a PBL scheme and does not resolve turbulence. Turbulence may develop more quickly and thus realistically over the entire domain if velocity perturbations are applied along the edges of the LES domain from which wind enters. Such a study might improve simulation results and demonstrate a more robust nesting strategy.

The preceding recommendations are based on the results from this dissertation and my not be generally applicable, but may still serve as guidelines for similar situations. They are intended to help improve wind energy forecast capabilities and resource assessment to reduce uncertainties and bolster the total renewable energy portfolio. These improvements may lead to policies and practices that mitigate the effects of climate change and improve the security and reliability of energy.

Bibliography

Adams, M and D Keith (2007). "A wind farm parameterization for WRF". In: *8th WRF Users Workshop*.

Aitken, Matthew L, Robert M Banta, Yelena L Pichugina, and Julie K Lundquist (2014a). "Quantifying wind turbine wake characteristics from scanning remote sensor data". In: *Journal of Atmospheric and Oceanic Technology* 31.4, pp. 765–787.

Aitken, Matthew L, Branko Kosović, Jeffrey D Mirocha, and Julie K Lundquist (2014b). "Large eddy simulation of wind turbine wake dynamics in the stable boundary layer using the Weather Research and Forecasting Model". In: *Journal of Renewable and Sustainable Energy* 6.3, p. 033137.

American Wind Energy Association (2012). *Wind Energy State Fact Sheets 2012*. Tech. rep. American Wind Energy Association.

Ammara, Idriss, Christophe Leclerc, and Christian Masson (2002). "A viscous three dimensional actuator disk method for the aerodynamic analysis of wind farms". In: *Journal of Solar Energy Engineering* 124.4, pp. 345–356.

Angevine, Wayne M., Hongli Jiang, and Thorsten Mauritsen (2010). "Performance of an Eddy Diffusivity Mass Flux Scheme for Shallow Cumulus Boundary Layers". In: *Monthly Weather Review* 138.7, pp. 2895–2912. ISSN: 0027-0644. DOI: 10.1175/2010MWR3142.1.

Antoniou, I, HE Jorgensen, F Ormel, SG Bradley, S Von Hunerbein, S Emeis, and G Warmbier (2003). *On the theory of SODAR measurement techniques (final reporting on WP1, EU WISE project NNE5-2001-297)*. Project Report. Roskilde, Denmark: Riso.

Aster, Richard C, Brian Borchers, and Clifford H Thurber (2013). *Parameter estimation and inverse problems*. Academic Press.

Barthelmie, Rebecca Jane et al. (2010). "Quantifying the impact of wind turbine wakes on power output at offshore wind farms". In: *Journal of Atmospheric and Oceanic Technology* 27.8, pp. 1302–1317.

Barthelmie, Rebecca et al. (2001). "ENDOW: Efficient Development of Offshore Windfarms". In: *Wind Engineering* 25.5, pp. 263–270. DOI: 10.1260/030952401760177837. eprint: http://dx.doi.org/10.1260/030952401760177837.

Basu, Sukanta, Albert AM Holtslag, Bas JH Van De Wiel, Arnold F Moene, and Gert-Jan Steeneveld (2008). "An inconvenient "truth" about using sensible heat flux as a surface boundary condition in models under stably stratified regimes". In: *Acta Geophysica* 56.1, pp. 88–99.

Bougeault, P. and P. Lacarrere (1989). "Parameterization of Orography-Induced Turbulence in a Mesobeta–Scale Model". In: *Monthly Weather Review* 117.8, pp. 1872–1890. ISSN: 0027-0644. DOI: `10.1175/1520-0493(1989)117<1872:POOITI>2.0.CO;2`.

Brasseur, James G and Tie Wei (2010). "Designing large-eddy simulation of the turbulent boundary layer to capture law-of-the-wall scaling)". In: *Physics of Fluids* 22.2, p. 021303.

Calaf, M, C Meneveau, and J Meyers (2010). "Large eddy simulation study of fully developed wind-turbine array boundary layers". In: *Physics of Fluids* 22.1. ISSN: 1070-6631. DOI: `10.1063/1.3291077`.

Calaf, Marc, Marc B Parlange, and Charles Meneveau (2011). "Large eddy simulation study of scalar transport in fully developed wind-turbine array boundary layers". In: *Physics of Fluids (1994-present)* 23.12, p. 126603.

Carvalho, D, A Rocha, M Gomez-Gesteira, and C Santos (2012). "A sensitivity study of the WRF model in wind simulation for an area of high wind energy". In: *Environmental Modelling amp; Software* 33, pp. 23–34. ISSN: 1364-8152. DOI: `10.1016/j.envsoft.2012.01.019`.

Chen, Y, FL Ludwig, and RL Street (2004). "Stably stratified flows near a notched transverse ridge across the Salt Lake valley". In: *Journal of Applied Meteorology* 43.9, pp. 1308–1328. ISSN: 0894-8763. DOI: `10.1175/1520-0450(2004)043<1308:SSFNAN>2.0.CO;2`.

Chow, FK, AP Weigel, RL Street, MW Rotach, and M Xue (2006). "High-resolution large-eddy simulations of flow in a steep Alpine valley. Part I: Methodology, verification, and sensitivity experiments". In: *Journal of Applied Meteorology and Climatology* 45.1, pp. 63–86. ISSN: 1558-8424. DOI: `10.1175/JAM2322.1`.

Churchfield, Matthew J, Sang Lee, John Michalakes, and Patrick J Moriarty (2012). "A numerical study of the effects of atmospheric and wake turbulence on wind turbine dynamics". In: *Journal of turbulence* 13.

Churchfield, Matthew J, J Michalakes, B Vanderwende, S Lee, MA Sprague, JK Lundquist, and PJ Moriarty (2013). *Using Mesoscale Weather Model Output as Boundary Conditions for Atmospheric Large-Eddy Simulations and Wind-Plant Aerodynamic Simulations (Presentation)*. Tech. rep. National Renewable Energy Laboratory (NREL), Golden, CO.

Deppe, Adam J., William A. Gallus, and Eugene S. Takle (2012). "A WRF Ensemble for Improved Wind Speed Forecasts at Turbine Height". In: *Wea. Forecasting* 28.1, pp. 212–228. ISSN: 0882-8156. DOI: `10.1175/WAF-D-11-00112.1`.

Dudhia, J. (1995). "Reply". In: *Mon. Wea. Rev.* 123.8, pp. 2573–2575. ISSN: 0027-0644. DOI: `10.1175/1520-0493(1995)123<2573:R>2.0.CO;2`.

Duque, Earl PN, Michael D Burklund, and Wayne Johnson (2003). "Navier-Stokes and comprehensive analysis performance predictions of the NREL phase VI experiment". In: *Journal of Solar Energy Engineering* 125.4, pp. 457–467.

Durran, Dale R. and Joseph B. Klemp (1983). "A Compressible Model for the Simulation of Moist Mountain Waves". In: *Mon. Wea. Rev.* 111.12, pp. 2341–2361. ISSN: 0027-0644. DOI: `10.1175/1520-0493(1983)111<2341:ACMFTS>2.0.CO;2`.

Elliott, DL and JC Barnard (1990). "Observations of wind turbine wakes and surface roughness effects on wind flow variability". In: *Solar Energy* 45.5, pp. 265–283.

Fitch, A. C., J. B. Olson, J. K. Lundquist, J. Dudhia, A. K. Gupta, J. Michalakes, and I. Barstad (2012). "Local and Mesoscale Impacts of Wind Farms as Parameterized in a Mesoscale NWP Model". In: *Monthly Weather Review*, p. 120307071704005. ISSN: 0027-0644, 1520-0493. DOI: `10.1175/MWR-D-11-00352.1`.

Floors, R., C.L. Vincent, S.-E. Gryning, A. Peña, and E. Batchvarova (2013). "The Wind Profile in the Coastal Boundary Layer: Wind Lidar Measurements and Numerical Modelling". English. In: *Boundary-Layer Meteorology* 147.3, pp. 469–491. ISSN: 0006-8314. DOI: `10.1007/s10546-012-9791-9`.

Freedman, J, M Markus, and R Penc (2008). "Analysis of West Texas wind plant ramp-up and ramp-down events". In: *AWSTruewind report*.

Glauert, H (1963). *Aerodynamic Theory: A General Review of Progress, volume IV, chapter Division L, Airplane Propellers*.

Gomez-Elvira, Rafael, Antonio Crespo, Emilio Migoya, Fernando Manuel, and Julio Hernandez (2005). "Anisotropy of turbulence in wind turbine wakes". In: *Journal of Wind Engineering and Industrial Aerodynamics* 93.10, pp. 797–814. ISSN: 0167-6105. DOI: `http://dx.doi.org/10.1016/j.jweia.2005.08.001`.

Gopalan, Harish et al. (2014). "Evaluation of the effect of Realistic and Synthetic Inflow on the Power and Loading Pattern of Wind Turbine". In: *AIAA SciTech*. American Institute of Aeronautics and Astronautics. DOI: `10.2514/6.2014-0707`.

Grell, GA, S Emeis, WR Stockwell, T Schoenemeyer, R Forkel, J Michalakes, R Knoche, and W Seidl (2000). "Application of a multiscale, coupled MM5/chemistry model to the complex terrain of the VOTALP valley campaign". In: *Atmospheric Environment* 34.9, 1435–1453. ISSN: 1352-2310.

Grenier, Herve and Christopher S. Bretherton (2001). "A Moist PBL Parameterization for Large-Scale Models and Its Application to Subtropical Cloud-Topped Marine Boundary Layers". In: *Monthly Weather Review* 129.3, pp. 357–377. ISSN: 0027-0644. DOI: `10.1175/1520-0493(2001)129<0357:AMPPFL>2.0.CO;2`.

Gronas, S and AD Sandvik (1999). "Numerical simulations of local winds over steep orography in the storm over north Norway on October 12, 1996". In: *Journal of Geophysical Research-Atmospheres* 104.D8, 9107–9120. ISSN: 0747-7309.

Hanna, SR and R Yang (2001). "Evaluations of Mesoscale Models' Simulations of Near-Surface Winds, Temperature Gradients, and Mixing Depths". In: *Journal of Applied Meteorology* 40.6, pp. 1095–1104. ISSN: 0894-8763, 1520-0450. DOI: `10.1175/1520-0450(2001)040<1095:EOMMSO>2.0.CO;2`.

Harris, Lucas M. and Dale R. Durran (2010). "An Idealized Comparison of One-Way and Two-Way Grid Nesting". In: *Mon. Wea. Rev.* 138.6, pp. 2174–2187. ISSN: 0027-0644. DOI: `10.1175/2010MWR3080.1`.

Hirth, Brian D, John L Schroeder, W Scott Gunter, and Jerry G Guynes (2012). "Measuring a utility-scale turbine wake using the TTUKa mobile research radars". In: *Journal of Atmospheric and Oceanic Technology* 29.6, pp. 765–771.

Hirth, Brian D, John L Schroeder, Zack Irons, and Kevin Walter (2015). "Dual-Doppler measurements of a wind ramp event at an Oklahoma wind plant". In: *Wind Energy*.

Högström, U, DN Asimakopoulos, H Kambezidis, CG Helmis, and A Smedman (1988). "A field study of the wake behind a 2 MW wind turbine". In: *Atmospheric Environment (1967)* 22.4, pp. 803–820.

Hong, Song-You, Yign Noh, and Jimy Dudhia (2006). "A New Vertical Diffusion Package with an Explicit Treatment of Entrainment Processes". In: *Monthly Weather Review* 134.9, pp. 2318–2341. ISSN: 0027-0644. DOI: 10.1175/MWR3199.1.

Hong, Song-You and Hua-Lu Pan (1996). "Nonlocal Boundary Layer Vertical Diffusion in a Medium-Range Forecast Model". In: *Monthly Weather Review* 124.10, pp. 2322–2339. ISSN: 0027-0644. DOI: 10.1175/1520-0493(1996)124<2322:NBLVDI>2.0.CO;2.

Ivanell, Stefan, Jens N Sørensen, Robert Mikkelsen, and Dan Henningson (2009). "Analysis of numerically generated wake structures". In: *Wind Energy* 12.1, pp. 63–80.

Janjic, Zavisa I. (1994). "The Step-Mountain Eta Coordinate Model: Further Developments of the Convection, Viscous Sublayer, and Turbulence Closure Schemes". In: *Monthly Weather Review* 122.5, pp. 927–945. ISSN: 0027-0644. DOI: 10.1175/1520-0493(1994) 122<0927:TSMECM>2.0.CO;2.

Kang, Seokkoo, Xiaolei Yang, and Fotis Sotiropoulos (2014). "On the onset of wake meandering for an axial flow turbine in a turbulent open channel flow". In: *Journal of Fluid Mechanics* 744, pp. 376–403.

Kelley, ND, BJ Jonkman, GN Scott, JT Bialasiewicz, and LS Redmond (2005). "The impact of coherent turbulence on wind turbine aeroelastic response and its simulation". In: *Windpower 2005 Conference Proceedings*.

Kosovic, Branko (1997). "Subgrid-scale modelling for the large-eddy simulation of high-Reynolds-number boundary layers". In: *Journal of Fluid Mechanics* 336, pp. 151–182. ISSN: 1469-7645. DOI: 10.1017/S0022112096004697.

Kosovic, Branko and Judith A Curry (2000). "A large eddy simulation study of a quasi-steady, stably stratified atmospheric boundary layer". In: *Journal of the Atmospheric Sciences* 57.8, pp. 1052–1068.

Landahl, MT and E Mollo-Christensen (1986). "Turbulence and Random Processes in Fluid MechanicsCambridge University Press". In: *Cambridge, UK*.

Lilly, DK (1967). "The representation of small-scale turbulence in numerical simulation experiments". In: *Proceedings of the IBM Scientific Computing Symposium on Environmental Sciences* IBM Form No. 320-1951. ISSN: 0022-4928.

Liu, Y, T Warner, Y Liu, C Vincent, W Wu, B Mahoney, S Swerdlin, K Parks, and J Boehnert (2011). "Simultaneous nested modeling from the synoptic scale to the LES scale for wind energy applications". In: *Journal of Wind Engineering and Industrial Aerodynamics* 99.4. ¡ce:title¿The Fifth International Symposium on Computational Wind Engineering¡/ce:title¿, pp. 308–319. ISSN: 0167-6105. DOI: 10.1016/j.jweia.2011.01. 013.

Lundquist, JK, MJ Churchfield, S Lee, and A Clifton (2015). "Quantifying error of lidar and sodar Doppler beam swinging measurements of wind turbine wakes using computational fluid dynamics". In: *Atmospheric Measurement Techniques* 8.2, pp. 907–920.

Madsen, Helge Aagaard (1996). "A CFD analysis of the actuator disc flow compared with momentum theory results". In: *Proceedings of the 10th IEA Symposium on the Aerodynamics of Wind Turbines, Department of Fluid Mechanics, Technical University of Denmark*, pp. 109–24.

Magnusson, M and A-S Smedman (1999). "Air flow behind wind turbines". In: *Journal of Wind Engineering and Industrial Aerodynamics* 80.1, pp. 169–189.

Mahoney, W.P. et al. (2012). "A Wind Power Forecasting System to Optimize Grid Integration". In: *Sustainable Energy, IEEE Transactions on* 3.4, pp. 670–682. ISSN: 1949-3029. DOI: `10.1109/TSTE.2012.2201758`.

Marjanovic, Nikola, Sonia Wharton, and Fotini K Chow (2014). "Investigation of model parameters for high-resolution wind energy forecasting: Case studies over simple and complex terrain". In: *Journal of Wind Engineering and Industrial Aerodynamics* 134, pp. 10–24.

Marquis, M, J Wilczak, M Ahlstrom, J Sharp, A Stern, JC Smith, and S Calvert (2011). "Forecasting the Wind to Reach Significant Penetration Levels of Wind Energy". In: *Bulletin of the American Meteorological Society* 92.9, pp. 1159–1171. ISSN: 0003-0007. DOI: `10.1175/2011BAMS3033.1`.

Martınez, Luis A, Stefano Leonardi, Matthew J Churchfield, and Patrick J Moriarty (2012). "A comparison of actuator disk and actuator line wind turbine models and best practices for their use". In: *AIAA Paper* 2012-0900.

Mass, CF et al. (2003). "Regional environmental prediction over the Pacific Northwest". In: *Bulletin of the American Meteorological Society* 84.10, pp. 1353–+. ISSN: 0003-0007. DOI: `10.1175/BAMS-84-10-1353`.

Mehta, D., A.H. van Zuijlen, B. Koren, J.G. Holierhoek, and H. Bijl (2014). "Large Eddy Simulation of wind farm aerodynamics: A review". In: *Journal of Wind Engineering and Industrial Aerodynamics* 133, pp. 1–17. ISSN: 0167-6105. DOI: `http://dx.doi.org/10.1016/j.jweia.2014.07.002`.

Meyers, Johan and Charles Meneveau (2010). "Large eddy simulations of large wind-turbine arrays in the atmospheric boundary layer". In: *AIAA Paper* 827, p. 2010.

— (2012). "Optimal turbine spacing in fully developed wind farm boundary layers". In: *Wind Energy* 15.2, pp. 305–317.

Mikkelsen, Robert (2003). "Actuator disc methods applied to wind turbines". PhD thesis. Technical University of Denmark.

Mikkelsen, Robert, Jens N Sørensen, Stig Øye, and Niels Troldborg (2007). "Analysis of power enhancement for a row of wind turbines using the actuator line technique". In: *Journal of Physics: Conference Series*. Vol. 75. 1. IOP Publishing, p. 012044.

Mirocha, J. D., B. Kosovic, M. L. Aitken, and J. K. Lundquist (2014). "Implementation of a generalized actuator disk wind turbine model into the weather research and forecasting model for large-eddy simulation applications". en. In: *Journal of Renewable and Sustainable Energy* 6.1, p. 013104. ISSN: 1941-7012. DOI: `10.1063/1.4861061`.

Mirocha, Jeffrey D, Daniel A Rajewski, Nikola Marjanovic, Julie K Lundquist, Branko Kosović, Caroline Draxl, and Matthew J Churchfield (2015). "Investigating wind turbine

impacts on near-wake flow using profiling lidar data and large-eddy simulations with an actuator disk model". In: *Journal of Renewable and Sustainable Energy* 7.4, p. 043143.

Monin, AS and AMf Obukhov (1954). "Basic laws of turbulent mixing in the surface layer of the atmosphere". In: *Contrib. Geophys. Inst. Acad. Sci. USSR* 151, pp. 163–187.

Nakanishi, Mikio and Hiroshi Niino (2006). "An Improved Mellor Yamada Level-3 Model: Its Numerical Stability and Application to a Regional Prediction of Advection Fog". English. In: *Boundary-Layer Meteorology* 119.2, pp. 397–407. ISSN: 0006-8314. DOI: `10.1007/s10546-005-9030-8`.

Park, Sungsu and Christopher S. Bretherton (2009). "The University of Washington Shallow Convection and Moist Turbulence Schemes and Their Impact on Climate Simulations with the Community Atmosphere Model". In: *Journal of Climate* 22.12, pp. 3449–3469. ISSN: 0894-8755. DOI: `10.1175/2008JCLI2557.1`.

Pijl, S.P. van der (2007). *Numerical Modelling of Wind Farm Aerodynamics*. Tech. rep. Technical Report ECN Internal, Energy Research Centre of the Netherlands.

Pleim, Jonathan E. (2007). "A Combined Local and Nonlocal Closure Model for the Atmospheric Boundary Layer. Part I: Model Description and Testing". In: *Journal of Applied Meteorology and Climatology* 46.9, pp. 1383–1395. ISSN: 1558-8424. DOI: `10.1175/JAM2539.1`.

Porte-Agel, F, YT Wu, H Lu, and RJ Conzemius (2011). "Large-eddy simulation of atmospheric boundary layer flow through wind turbines and wind farms". In: *Journal of Wind Engineering and Industrial Aerodynamics* 99.4, pp. 154–168. ISSN: 0167-6105. DOI: `10.1016/j.jweia.2011.01.011`.

Rajewski, Daniel A, Eugene S Takle, Julie K Lundquist, John H Prueger, Richard L Pfeiffer, Jerry L Hatfield, Kristopher K Spoth, and Russell K Doorenbos (2014). "Changes in fluxes of heat, H 2 O, and CO 2 caused by a large wind farm". In: *Agricultural and Forest Meteorology* 194, pp. 175–187.

Rajewski, Daniel A et al. (2013). "Crop wind energy experiment (CWEX): observations of surface-layer, boundary layer, and mesoscale interactions with a wind farm". In: *Bulletin of the American Meteorological Society* 94.5, pp. 655–672.

Rhodes, Michael E and Julie K Lundquist (2013). "The effect of wind-turbine wakes on summertime US Midwest atmospheric wind profiles as observed with ground-based Doppler lidar". In: *Boundary-Layer Meteorology* 149.1, pp. 85–103.

Rye, Barry J and RMichael Hardesty (1993). "Discrete spectral peak estimation in incoherent backscatter heterodyne lidar. I. Spectral accumulation and the Cramer-Rao lower bound". In: *Geoscience and Remote Sensing, IEEE Transactions on* 31.1, pp. 16–27.

Sanderse, B, SP Pijl, and B Koren (2011). "Review of computational fluid dynamics for wind turbine wake aerodynamics". In: *Wind Energy* 14.7, pp. 799–819.

Shaw, W. J., J. K. Lundquist, and S. J. Schreck (2009). *Workshop on research needs for wind resource characterization*. Bull. Am. Meteor. Soc. 90, pp. 535–538.

Skamarock, W., J. B. Klemp, J. Dudhia, D. O. Gill, D. Barker, M. G. Duda, X. Y. Huang, and W. Wang (2008). *A Description of the Advanced Research WRF Version 3*. NCAR Technical Note NCAR/TN-475+STR.

Skamarock, WC and JB Klemp (2008). "A time-split nonhydrostatic atmospheric model for weather research and forecasting applications". In: *Journal of Computational Physics* 227.7, 3465–3485. ISSN: 0021-9991. DOI: {10.1016/j.jcp.2007.01.037}.

Smagorinsky, J (1963). "GENERAL CIRCULATION EXPERIMENTS WITH THE PRIMITIVE EQUATIONS". In: *Monthly Weather Review* 91.3, pp. 99–164. ISSN: 0027-0644, 1520-0493. DOI: 10.1175/1520-0493(1963)091<0099:GCEWTP>2.3.CO;2.

Smalikho, IN, VA Banakh, YL Pichugina, WA Brewer, RM Banta, JK Lundquist, and ND Kelley (2013). "Lidar investigation of atmosphere effect on a wind turbine wake". In: *Journal of Atmospheric and Oceanic Technology* 30.11, pp. 2554–2570.

Sørensen, Jens Nørkær (2011). "Instability of helical tip vortices in rotor wakes". In: *Journal of Fluid Mechanics* 682, pp. 1–4.

Sorensen, JN and WZ Shen (2002). "Numerical Modelling of Wind Turbine Wakes". In: *Journal of Fluids Engineering* 124.2, pp. 393–399. ISSN: 0098-2202.

Sørensen, JN, WZ Shen, and X Munduate (1998). "Analysis of wake states by a full-field actuator disc model". In: *Wind Energy* 1.2, pp. 73–88.

Sørensen, Niels N and Martin OL Hansen (1998). "Rotor performance predictions using a Navier-Stokes method". In: *AIAA paper* 98, p. 0025.

Storm, B, J Dudhia, S Basu, A Swift, and I. Giammanco (2009). "Evaluation of the Weather Research and Forecasting Model on Forecasting Low-level Jets: Implications for Wind Energy". In: *Wind Energy* 12.1, 81–90. ISSN: 1095-4244. DOI: {10.1002/we.288}.

Sukoriansky, Semion, Boris Galperin, and Veniamin Perov (2005). "Application of a New Spectral Theory of Stably Stratified Turbulence to the Atmospheric Boundary Layer over Sea Ice". English. In: *Boundary-Layer Meteorology* 117.2, pp. 231–257. ISSN: 0006-8314. DOI: 10.1007/s10546-004-6848-4.

Talbot, C, E Bou-Zeid, and J Smith (2012). "Nested Mesoscale Large-Eddy Simulations with WRF: Performance in Real Test Cases". In: *Journal of Hydrometeorology* 13.5, pp. 1421–1441.

Thomsen, Kenneth and Poul Sorensen (1999). "Fatigue loads for wind turbines operating in wakes". In: *Journal of Wind Engineering and Industrial Aerodynamics* 80.12, pp. 121–136. ISSN: 0167-6105. DOI: http://dx.doi.org/10.1016/S0167-6105(98)00194-9.

Troldborg, Niels, Jens N Sorensen, and Robert Mikkelsen (2010). "Numerical simulations of wake characteristics of a wind turbine in uniform inflow". In: *Wind Energy* 13.1, pp. 86–99.

Troldborg, Niels, Jens N Sørensen, and Robert Mikkelsen (2007). "Actuator line simulation of wake of wind turbine operating in turbulent inflow". In: *Journal of physics: conference series*. Vol. 75. 1. IOP Publishing, p. 012063.

Vanderwende, BJ and Julie K Lundquist (2012). "The modification of wind turbine performance by statistically distinct atmospheric regimes". In: *Environmental Research Letters* 7.3, p. 034035.

Vermeer, LJ, Jens Nørkær Sørensen, and A Crespo (2003). "Wind turbine wake aerodynamics". In: *Progress in aerospace sciences* 39.6, pp. 467–510.

Wharton, S and JK Lundquist (2012a). "Assessing atmospheric stability and its impacts on rotor-disk wind characteristics at an onshore wind farm". en. In: *Wind Energy* 15.4, pp. 525–546. ISSN: 1099-1824. DOI: `10.1002/we.483`.

Wharton, Sonia and Julie K Lundquist (2012b). "Atmospheric stability affects wind turbine power collection". In: *Environmental Research Letters* 7.1, p. 014005.

Williams, JL, RM Maxwell, JK Lundquist, and S Wharton (2009). "On the use of a coupled variably-saturated groundwater flow - land surface model to initialize a fully coupled subsurface - land surface - atmospheric model for wind energy forecasting". In: *Eos Trans. AGU Fall Meeting Supplement* 90.52, A31F-0183.

Woodward, CS, RM Maxwell, JK Lundquist, J Mirocha, S Smith, and AF Tompson (2009). "Wind Energy Resource Assessment using Coupled Groundwater-Land-Surface Atmospheric Models". In: *Eos Trans. AGU Fall Meeting Supplement* 90.52, A31F-0189.

Wu, Yu-Ting and Fernando Porté-Agel (2011). "Large-eddy simulation of wind-turbine wakes: evaluation of turbine parametrisations". In: *Boundary-layer meteorology* 138.3, pp. 345–366.

— (2012). "Atmospheric turbulence effects on wind-turbine wakes: An LES study". In: *energies* 5.12, pp. 5340–5362.

Wyngaard, JC (2004). "Toward numerical modeling in the "terra incognita"". In: *Journal of the Atmospheric Sciences* 61.14, 1816–1826. ISSN: 0022-4928.

Xie, Bo, Jimmy C. H. Fung, Allen Chan, and Alexis Lau (2012). "Evaluation of nonlocal and local planetary boundary layer schemes in the WRF model". In: *Journal of Geophysical Research: Atmospheres* 117.D12, n/a–n/a. ISSN: 2156-2202. DOI: `10.1029/2011JD017080`.

Xie, Bo, J. C. R. Hunt, D. J. Carruthers, J. C. H. Fung, and J. F. Barlow (2013). "Structure of the planetary boundary layer over Southeast England: Modeling and measurements". In: *Journal of Geophysical Research: Atmospheres* 118.14, pp. 7799–7818. ISSN: 2169-8996. DOI: `10.1002/jgrd.50621`.

Yver, C. E., H. D. Graven, D. D. Lucas, P. J. Cameron-Smith, R. F. Keeling, and R. F. Weiss (2013). "Evaluating transport in the WRF model along the California coast". In: *Atmospheric Chemistry and Physics* 13.4, pp. 1837–1852. DOI: `10.5194/acp-13-1837-2013`.

Zahle, Frederik, Niels N Sørensen, and Jeppe Johansen (2009). "Wind turbine rotor-tower interaction using an incompressible overset grid method". In: *Wind Energy* 12.6, pp. 594–619.

Zajaczkowski, Frank J, Sue Ellen Haupt, and Kerrie J Schmehl (2011). "A preliminary study of assimilating numerical weather prediction data into computational fluid dynamics models for wind prediction". In: *Journal of Wind Engineering and Industrial Aerodynamics* 99.4, pp. 320–329.

Zhang, Hailing, Zhaoxia Pu, and Xuebo Zhang (2013a). "Examination of Errors in Near-Surface Temperature and Wind from WRF Numerical Simulations in Regions of Complex Terrain". In: *Wea. Forecasting* 28.3, pp. 893–914. ISSN: 0882-8156. DOI: `10.1175/WAF-D-12-00109.1`.

Zhang, Wei, Corey D Markfort, and Fernando Porté-Agel (2013b). "Wind-turbine wakes in a convective boundary layer: A wind-tunnel study". In: *Boundary-layer meteorology* 146.2, pp. 161–179.